THEORETICAL ELECTRONIC STRUCTURE OF STRUCTURALLY MODIFIED GRAPHENE

by

Marc David Dvorak

A thesis submitted to the Faculty and the Board of Trustees of the Colorado School of Mines in partial fulfillment of the requirements for the degree of Doctor of Philosophy (Applied Physics).

Golden, Colorado

Date ________________________

Signed: ________________________
Marc David Dvorak

Signed: ________________________
Dr. Zhigang Wu
Thesis Advisor

Golden, Colorado

Date ________________________

Signed: ________________________
Dr. Jeff Squier
Professor and Head
Department of Physics

ABSTRACT

Graphene has emerged as a promising replacement for silicon in next-generation electronics and optoelectronic devices. If graphene is to be used in semiconductor devices, however, it must acquire an electronic band gap. Numerous approaches have been proposed to control the band gap of graphene, including the periodic patterning of defects. However, the mechanism for band gap opening and the associated physics in graphene patterned with defects remain unclear. Using both analytic theory and first-principles calculations, we show that periodic patterning of defects on graphene can open a large and tunable band gap, induce strong absorption peaks at optical wavelengths, and host a giant band gap quantum spin Hall phase. First, a geometric rule is analytically derived for the arrangements of defects that open a band gap in graphene, with one ninth of all possible patterns opening a band gap. Next, we perform *ab-initio* density functional calculations to compare the effects of structural vacancies, hexagonal BN dopants, and passivants on the electronc structure of graphene. Qualitatively, these three types of structural defects behave the same, with only slight differences in their resulting band structures. By adjusting the shape of structural defects, we show how to move the Dirac cones in reciprocal space in accordance with the tight-binding model for the anisotropic honeycomb lattice, while the fundamental mechanism for band gap opening remains the same. To quantitatively predict the band gap and optical properties of these materials, we employ many-body perturbation theory with Green's functions (GW/Bethe-Salpeter equation) to directly include electron-electron and electron-hole interactions. Structurally modified graphene shows a strong renormalization of the fundamental band gap over single particle descriptions, and a strong electron-hole interaction as indicated by strong exciton binding energies ($>$ 0.5 eV). Finally, we show that structurally modified graphene can host a topologically insulating phase if spin-orbit interactions are included. Tight-binding calculations show that an insulating graphene nanomesh is also a

quantum spin Hall insulator with a giant bulk band gap, an extremely valuable material for next-generation spintronics.

TABLE OF CONTENTS

LIST OF FIGURES

LIST OF TABLES

LIST OF SYMBOLS

Bloch wavevector . . . . $\mathbf{k}$

Hamiltonian . . . . H

Bloch wave . . . . ψ_{k}

Number of electrons . . . . N

Electronic creation operator . . . . $a_i^\dagger$

Electronic destruction operator . . . . a_i

Tight-binding hopping parameter . . . . t

Tight-binding on-site energy . . . . E_0

Exchange-correlation energy functional . . . . E_{XC}

Exchange-correlation potential . . . . V_{XC}

Charge density . . . . $\rho(\mathbf{r})$

Electronic self-energy . . . . Σ

Velocity operator . . . . $\mathbf{v}$

Polarization vector . . . . $\mathbf{e}$

Exciton eigenstate . . . . $|S\rangle$

Imaginary dielectric function . . . . $\epsilon_2(\omega)$

Set of parameters defining Hamiltonian . . . . $\mathbf{R}$

Closed contour in space defining Hamiltonian . . . . $\mathcal{C}$

Surface bounded by a closed countour in space defining Hamiltonian . . . . $\mathcal{S}$

Corners of hexagonal BZ of graphene . . . . $\mathbf{K}$

Location of Dirac points in BZ . . . . $\mathbf{D}$

Electronic band gap . . . . E_{g}

Periodic potential on graphene . . . . $U(\mathbf{r})$

Translation vectors of graphene supercell . . . . $\mathbf{R}_1$, $\mathbf{R}_2$

Translation vectors of graphene . . . . $\mathbf{a}_1$, $\mathbf{a}_2$

Chiral vector of carbon nanotube . . . . $\mathbf{C}_{\mathrm{h}}$

Transverse vector of carbon nanotube . . . . $\mathbf{T}$

LIST OF ABBREVIATIONS

Photovoltaic . . . . PV

Carbon nanotube . . . . CNT

Graphene nanoribbon . . . . GNR

Tight-binding . . . . TB

Density functional theory . . . . DFT

Self-energy as a product of Green's function (G) and screened interaction (W) . . . . GW

Bethe-Salpeter equation . . . . BSE

Quasiparticle . . . . QP

Topological insulator . . . . TI

Graphene nanomesh . . . . GNM

Many-body perturbation theory . . . . MBPT

Random phase approximation . . . . RPA

Quantum spin Hall . . . . QSH

ACKNOWLEDGMENTS

I would first like to thank my advisor, Zhigang Wu, for guiding me through five years of graduate school. His initial intuition that there was still much to be discovered in a field that had already attracted significant research interest provided me with a productive and valuable dissertation. His instruction has been excellent, and his openness to my ideas has made our research very collaborative.. I would also like to thank Mark Lusk and David Wood for regularly providing comments and suggestions at our electronic structure group meetings. I am also grateful to the remaining members of my committee, Cristian Ciobanu (committee chair), James Bernard, and Su-Huai Wei for reviewing my research proposal and dissertation and providing valuable feedback.

I would like to acknowledge my funding from the US Department of Energy grant DE-SC0006433, which allowed me to attend graduate school in the first place and made my research possible. The Golden Energy Computing Organization (GECO) and the National Energy Research Scientific Computing Center (NERSC) have provided extremely valuabe computational resources that made my research possible.

Most importantly, I want to thank my parents (Tom and Karen) and sisters (Sophie and Tessa) for their endless love, support, and encouragement. Their support and confidence in me to finish graduate school has made all the difference. I am also grateful to my Great-Aunt Rose and Great-Uncle Dale for helping me navigate the in's and out's of graduate school, a particularly nebulous institution to those who have never navigated it themselves.

CHAPTER 1

INTRODUCTION

1.1 Project Objectives

Graphene, a monolayer of carbon atoms arranged in a honeycomb lattice (Figure 1.1), is the miracle material of the 21st century. It is incredibly strong, atomically thin, and its charge carriers behave like ultra-relativistic massless Dirac particles. Graphene has remarkable electron mobility and can conduct heat and electric current efficiently. Optically, it absorbs red light unusually well, with absorption much higher than expected for an atomically thin material. In addition, graphene exhibits the quantum spin Hall effect, an insulating phase with topologically protected, spin-filtered edge states. Beyond the fundamental science, graphene has attracted great research interest for technological applications, including electronics, optoelectronics, and spintronics.

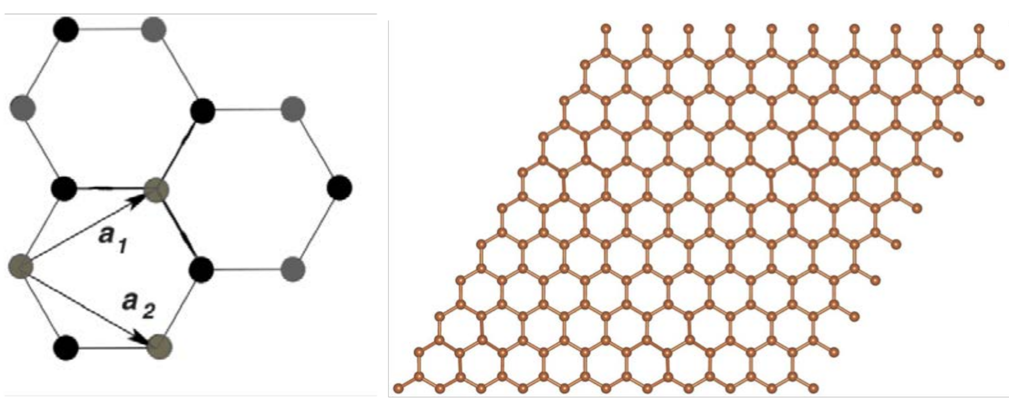

Figure 1.1: Primitive cell (left) and a sheet of graphene (right). A- and B-sublattices are indicated by light and dark circles in the primitive cell.

As the performance of conventional semiconductor technologies nears its peak, graphene-based devices have emerged as a viable candidate to replace bulk semiconductors in next-generation photovoltaic (PV) cells and microprocessors [1–9]. The major obstacle to creating such devices is reliably creating useful semiconducting materials from graphene, which is intrisically gapless. One approach is modifying the boundary conditions, using carbon nanotubes (CNTs) or graphene nanoribbons (GNRs), to open a band gap, e.g. adjusting their chirality relative to the graphene lattice to remove semimetallic points in the band structure. It is also possible to open a band gap in graphene by applying periodic structural defects. While band gap opening in CNTs and GNRs is well understood, the mechanism for band gap opening in periodically defected graphene [10–15] remains unclear. Studies have shown, however, that it is sometimes possible to open a sizable band gap in graphene by applying periodic structural defects. Although numerous *ab-initio* calculations have been carried out to compute the electronic structure of these materials [10–19], there is still no consensus about the origin of their band gap.

The primary objective of this research is to provide an analytic understanding of electronic structure in structurally modified graphene that can be used to design graphene-based materials for electronics and optoelectronics. We investigate their electronic structures with both analytic modeling based on tight-binding (TB), and numerical calculations based on density functional theory (DFT) and many-body perturbation theory. Specifically, a perturbative tight-binding model is presented to qualitatively predict the appearance of band gaps, and DFT calculations are performed to confirm the TB model. Next, we perform highly accurate quasiparticle calculations in the GW approximation to quantitatively predict band gaps in semiconducting defected graphene structures. Their optical absorption spectra and electron-hole binding energies are evaluated by solving the Bethe-Salpeter equation. These results highlight the controllable nature of many-body interactions in graphene by adjusting structural defects. Finally, we explore the topology of the band structure in defected graphene and show that structurally modified graphene can also be a quantum spin Hall insulator with a large bulk band gap.

Because there are so many possible types of structural defects on graphene, we must clarify exactly what types of defects we consider in this research. Prior research has shown defects that break graphene's A- B-sublattice symmetry open a band gap. This mechanism is well understood; when imbalance is introduced between sublattices, their on-site energies are different and the resulting spectrum is gapped. Within the category of sublattice symmetry breaking defects are those that preserve the honeycomb lattice and those that break it [20–24]. Lattice preserving defects are substitional dopants that do not affect the crystal structure [25, 26], while the introduction of pentagonal, heptagonal, etc. rings on graphene breaks the honeycomb lattice. In either case, sublattice imbalance is responsible for band gap opening. In this dissertation, we focus on defects that *preserve* both sublattice symmetry and the honeycomb lattice. There is no consensus on the mechanism for band gap opening in these materials. Proposed mechanisms include quantum confinement or a chemical effect, but there has yet to be a first-principles explanation for either, and there is empirical evidence that neither one is correct.

An analytic model of band gap opening in periodically modified graphene can reveal the fundamental mechanism responsible for such a semimetal to semiconductor transition. Numerical first-principles calculations have been carried out to compute electronic structures of various defected graphene sheets. However, only empirical band gap opening rules were found which cannot reveal the basic physics involved or predict if structurally modified graphene with arbitrary defect distribution is semiconducting or semimetallic.

On the other hand, analytic models cannot offer *ab-initio* quantitative predictions for the magnitude of the band gap, which can be predicted with mean-field methods or many-body theory. Mean-field methods, such as density functional theory, are advantageous over many-body techniques because of their affordable computational cost. DFT is useful for qualitatively describing electronic structure and guiding experimentalists in choosing materials among numerous choices. In this research, we use DFT to confirm and parameterize analytic models. However, DFT systematically and severely underestimates the single-particle band gaps (E_{g}) of semiconductors and insulators. For this reason, quantitative predictions of E_{g} are obtained using the GW approximation. The GW approximation uses the DFT eigenstates to estimate the electronic self-energy, the results of which are directly comparable to experimental photoemission/inverse photoemission data. *GW* is extremely computationally expensive, so we perform *GW* calculations only for a few representative materials.

In contrast to single-QP energy levels, the electron-hole interaction and the optical absorption are intrinsically two-particle quantities, requiring a solution of the Bethe-Salpeter equation (BSE). Much theoretical work has shown that the independent quasiparticle absorption cannot reliably reproduce experimental optical spectra [27–33]. Low dimensional systems, in particular, require the explicit treatment of the e-h interaction due to reduced electronic screening and the close proximity of electron and hole, leading to their strengthened coupling. Additionally, optical properties are of direct interest for photovoltaic applications.

Pristine graphene was the first predicted quantum spin Hall (QSH) insulator [34, 35], a material that is insulating in the bulk but possesses spin-filtered metallic states on its edges. In graphene, its bulk band gap due to spin-orbit coupling is less than $k_{\mathrm{B}}\mathrm{T}$ at room temperature [36] - too small to be practical for devices. In order to make spintronic devices with the QSH state's spin-filtered edge states, the bulk band gap must be increased. Recently, research on the QSH effect in graphene has focused on increasing the bulk band gap by enhancing spin-orbit coupling with heavy metal-atom dopants. However, periodic defects on graphene can also open a sizable band gap. We perform TB calculations based on the original Kane-Mele model for the QSH insulator modified to include structural defects [34, 35]. Our goal is to determine whether structural defects still allow a QSH phase to exist, or if defects break the symmetries necessary for a QSH phase to form. If both the large bulk band gap and QSH phase exist, structurally modified graphene would be a promising QSH insulator for spintronic devices.

This dissertation addresses a very difficult yet practical problem in nanoscale physics: how to make use of structural modifications to tune the electronic properties and optical absorption of graphene. Our results substantially advance the understanding of electronic structure and optical properties of defected graphene and advance the field one step closer to geometrically engineering semiconducting graphene for realistic optoelectronic devices.

1.2 Introduction and Motivation

Technologies based on conventional semiconductors have progressed at an impressive pace over the past 50 years. Microprocessors and integrated circuits, in particular, have developed nearly in agreement with Moore's Law, which predicts that the number of transistors per unit area approximately doubles every two years. However, performance of these devices is starting to level off as device size and efficiency quickly approach physical limits [37–39]. As individual processor speed flattens, manufacturers have started to introduce multiple core CPUs and novel processor architectures to compensate. Additionally, theoretical efficiency limits and high manufacturing costs of crystalline-silicon-based photovoltaic cells have prompted investigations into novel materials and devices for next-generation PV cells. Existing solar energy conversion technologies are not cost effective at their current efficiencies and manufacturing costs [40, 41].

Overcoming these performance limits requires a paradigm shift from the conventional materials and methods used in the past. Among the more promising developments is the use of nanostructures that can be optimized for a particular application, for example, multiple-exciton generation in quantum dots for possible PV applications [42] or graphene-based materials with high carrier mobility. Nanostructures are attractive because their properties can be tuned by quantum confinement and are sensitive to structure and surface chemistry [43, 44]. In addition, these nanomaterials could reduce manufacturing cost dramatically.

Graphene-based nanostructures, in particular, continue to attract considerable research interest in electronics[1, 45]. Due to its massless-Dirac-fermion charge carriers [46], graphene has anomalously high electrical conductivity. This makes graphene appealing for electronics, but it lacks a sizable electronic band gap necessary for semiconductor devices. The pursuit of semiconducting, graphene-based nanostructures that maintain its electrical conductivity has been an active area of research for many years. Among these carbon allotropes are the carbon nanotube, the graphene nanoribbon, and the graphene nanomesh (GNM) - a periodic array of holes on pristine graphene which have already been used to build functional field-effect transistors (Figure 1.2) [6]. GNRs and CNTs have been studied extensively, while

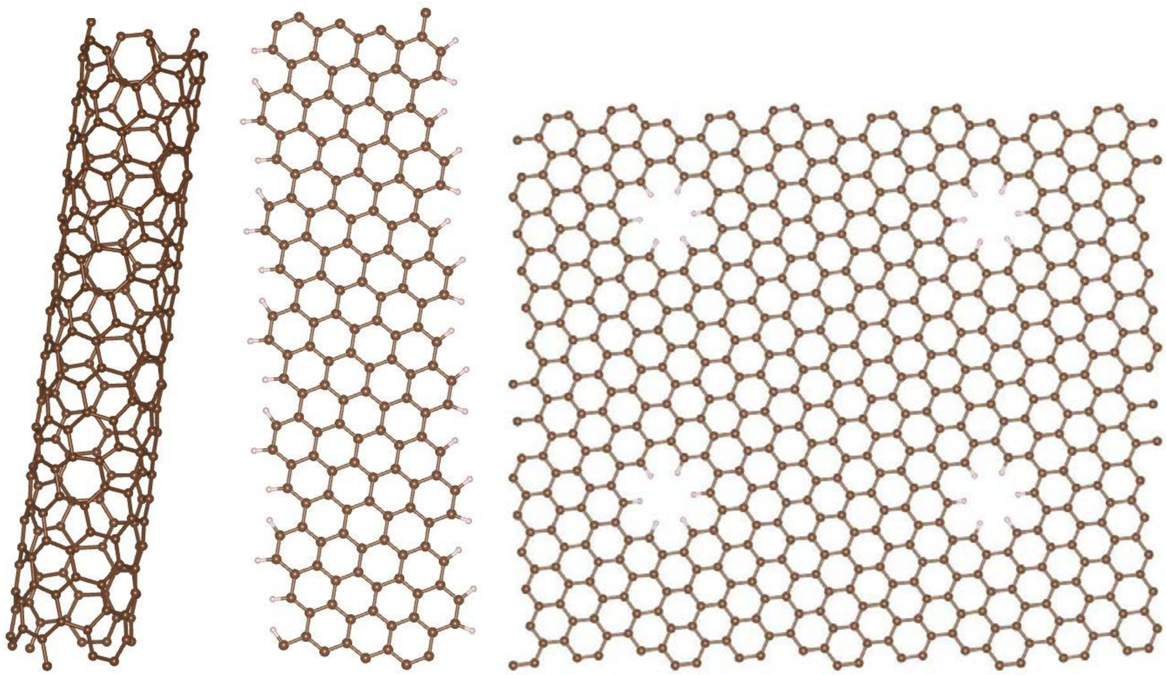

Figure 1.2: A carbon nanotube (left), graphene nanoribbon (center), and graphene nanomesh (right). Brown dots are C atoms and white dots are H passivants.

understanding of GNMs is currently limited to TB models and DFT calculations. Extensive computational studies of CNTs at the many-body perturbation theory (MBPT) level have revealed insightful physics [47, 48] and successfully explained experimental data. Similar theoretical descriptions of GNMs have not been completed and are necessary to guide experimentalists. A rigorous study of many-body effects in GNMs advances the understanding of fundamental physics in valuable graphene-based nanostructures.

So far, the discussion has been limited to GNMs, but graphene can actually be patterned with many different defects. This freedom in choosing defects when creating periodically modified graphene gives these structures a distinct advantage over CNTs or GNRs. CNTs and GNRs are inherently pure graphene subject to one dimensional quantum confinement and different chiralities. They possess only this single degree of freedom − periodicity and orientation of the structure. By introducing structural modifications to pristine graphene, one can tune both defect size and distribution to control the material's properties − many additional degrees of freedom. Boundary conditions and periodicity still play a crucial role, but altering defect type and size generates a seemingly endless number of possible structures. The greater flexibility in the modified graphene landscape allows for additional customization of periodically defected structures, making them more attractive than CNTs or GNRs.

The focus on GNMs over alternatively defected sheets is justified by recent research showing great viability in GNMs through the demonstration of functional GNM devices. Bai *et al.* demonstrated GNM based field-effect transistors (FET) capable of supporting currents 100 times that of GNR based devices [6]. Zeng *et al.* used an anodic aluminum oxide membrane to create an FET of their own [49], and Sinitskii *et al.* demonstrated self-assembled GNM devices [50]. Akhavan fabricated GNMs by local photodegradation of graphene using ZnO nanorods [51]. The experimental promise of GNMs calls for a more complete theoretical description of their electronic and optical properties, but also highlights the relatively narrow scope of the previous theoretical and computational work. Publications prior to our research are largely limited to numerical trends without a precise understanding of the physics involved. There is also a complete lack of understanding of many-body effects in defected graphene.

1.3 Theory and Methods

A hierarchy of electronic structure methods of successively improved accuracy and more rigorous theory is used in this research. First, an analytic perturbative model for periodic potentials in graphene is presented. Next, calculations based on density functional theory relax the atomic structure of the system of interest and compute electronic band structures. DFT also provides Kohn-Sham states and energies as a basis for the subsequent steps. Quasiparticle corrections are applied to the DFT band structure in the GW approximation. Finally, we include the electron-hole interaction and compute the optical absorption and exciton binding energies by approximately solving the equation of motion for the two-particle Green's function, the Bethe-Salpeter equation. A brief discussion of topological insulators is also presented to provide the reader with enough background for Chapter 6 of this dissertation.

1.3.1 Tight-binding

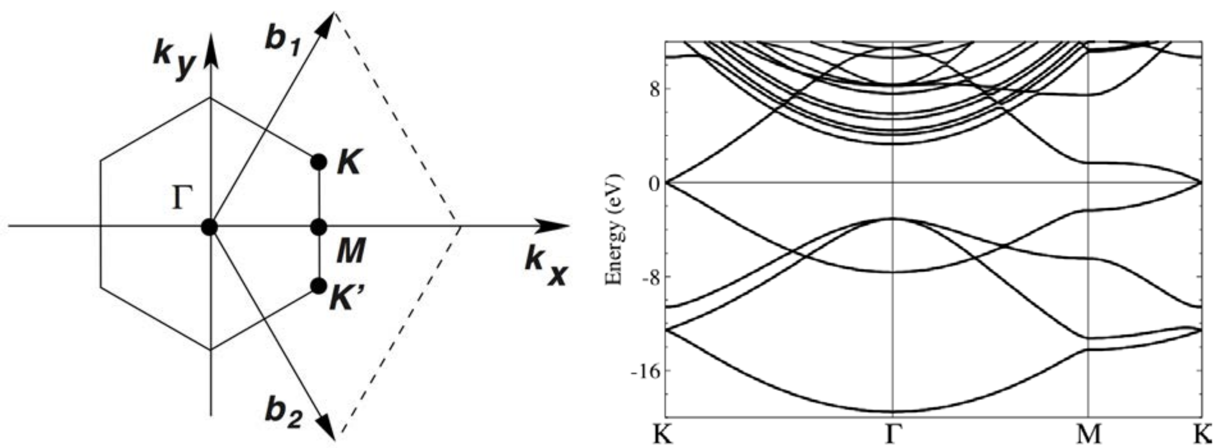

Figure 1.3: Brillouin zone (left) and TB dispersion of graphene (right).

The simplest approach to describe the electronic structure of graphene is the tight-binding method [52]. In tight-binding, one assumes that Bloch states in a crystal can be written as a superposition of atomic orbitals. In one dimension, for Bloch wave $\psi_k(x)$, this means that

$$\psi_k(x) = \frac{1}{\sqrt{N}} \sum_{j=1}^{N} e^{ikX_j} \phi(x - X_j). \tag{1.1}$$

Here, $\phi(x - X_j)$ is an atomic orbital centered at position X_j in the one dimensional chain. With the full Hamiltonian of the crystal H, the energy of this state gives rise to on-site and hopping terms that are typical of TB Hamiltonians.

$$E(k) = \langle \phi(x) | \, H \, | \phi(x) \rangle + \sum_j e^{ikX_j} \langle \phi(x) | \, H \, | \phi(x - X_j) \rangle \tag{1.2}$$

Here, the first term is the on-site energy of an electron at the origin, and the second term represents hopping from the origin to all other lattice sites. In second quantized notation, and if hopping is truncated to only nearest-neighbor lattice sites, the Hamiltonian takes the form

$$H = \sum_i \epsilon_i a_i^\dagger a_i + \sum_{\langle i,j \rangle} t_{ij} a_i^\dagger a_j. \tag{1.3}$$

Because graphene has a two atom basis, the matrix representation of Equation 1.3 is a 2×2 matrix. With only nearest neighbor hopping (t) and on-site energy (E_0), the TB Hamiltonian in graphene is

$$H_{\mathbf{k}} = \begin{pmatrix} E_0 & tf(\mathbf{k}) \\ tf^*(\mathbf{k}) & E_0 \end{pmatrix}. \tag{1.4}$$

The energy eigenvalues are

$$\begin{aligned} E_{\pm}(\mathbf{k}) &= E_0 \pm t|f(\mathbf{k})| \\ |f(\mathbf{k})| &= \sqrt{3 + 2\cos(\sqrt{3}k_y a) + 4\cos\left(\frac{\sqrt{3}}{2}k_y a\right)\cos\left(\frac{3}{2}k_x a\right)} \end{aligned}$$

Valence and conduction bands just touch at two symmetry-inequivalent Dirac points in the Brillouin zone at $\mathbf{K} = \left(\frac{2\pi}{3a}, \pm\frac{2\pi}{3\sqrt{3}a}\right)$, making it a semimetal. The TB dispersion of graphene is shown in Figure 1.3.

1.3.2 Density functional theory

Improving upon the TB description of electronic structure, DFT is, in principle, an exact theory for the ground state of a many-body system [53]. The total energy of the system is determined uniquely by the ground state charge density $\rho(\mathbf{r})$.

$$E[\rho(\mathbf{r})] = \frac{1}{2}\sum_{i=1}^{N}\int \psi_i^*(\mathbf{r})\nabla^2\psi_i(\mathbf{r})d\mathbf{r} + \int \rho(\mathbf{r})V_{\text{ext}}(\mathbf{r})d\mathbf{r} + \frac{1}{2}\iint \frac{\rho(\mathbf{r})\rho(\mathbf{r}')}{|\mathbf{r}-\mathbf{r}'|}d\mathbf{r}d\mathbf{r}' + E_{\text{XC}}[\rho(\mathbf{r})]$$

The terms on the right-hand side are the kinetic energy, external potential (including the ionic potential) energy, Hartree energy, and the exchange-correlation (XC) energy, respectively. Applying a varational principle to minimize the total energy, one can derive the well-known Kohn-Sham (KS) equations [54]:

$$\left[-\frac{1}{2}\nabla^2 + V_{\text{ext}}(\mathbf{r}) + V_{\text{H}}(\mathbf{r}) + V_{\text{XC}}(\mathbf{r})\right]\psi_i(\mathbf{r}) = \epsilon_i\psi_i(\mathbf{r}) \tag{1.5}$$

where the Hartree potential $V_{\text{H}}(\mathbf{r})$ and the XC potential $V_{\text{XC}}(\mathbf{r})$ are defined as $V_{\text{H}}(\mathbf{r}) = \int \frac{\rho(\mathbf{r}')}{|\mathbf{r}-\mathbf{r}'|}d\mathbf{r}'$ and $V_{\text{XC}}(\mathbf{r}) = \delta E_{\text{XC}}[\rho(\mathbf{r})]/\delta\rho(\mathbf{r})$. Once the nonlinear Kohn-Sham equations for each i^{th} electronic wave function are solved self-consistently, the ground state charge density, electronic structure, and atomic forces can be computed.

Unfortunately, the exact XC energy functional is not known. In practice, then, DFT cannot give the *exact* ground state energy of a system. Luckily, simple approximations to the XC functional, including the local density approximation [54] (LDA) based on quantum monte carlo calculations of the electron gas and gradient corrected functionals [55, 56], give surprisingly accurate results in comparison with experiment.

1.3.3 GW approximation

Formally, the wave functions and energy eigenvalues obtained from DFT are physically meaningless - they are ancillary quantities en route to obtaining the total charge density and ground state energy. It is somewhat fortunate, then, that the electronic structure obtained by DFT actually matches experiment reasonably well. Because the DFT electronic structure is close to experiment, it is common to interpret DFT energies and eigenfunctions as quasiparticle states of the many-body system. Strictly speaking, however, quasi-electrons and quasi-holes are solutions to the following equation [57, 58],

$$\left[-\frac{1}{2}\nabla^2 + V_{ext}(\mathbf{r}) + V_H(\mathbf{r})\right]\psi_i(\mathbf{r}) + \int \Sigma(\mathbf{r}, \mathbf{r}', \epsilon_i)\psi_i(\mathbf{r}')d\mathbf{r}' = \epsilon_i\psi_i(\mathbf{r}), \tag{1.6}$$

where Σ is the electronic self-energy. For most realistic systems, it is numerically intractable to solve this equation directly. Instead, it is common to compute self-energy corrections to the DFT eigenvalues in the *GW* approximation. *GW* can be formally derived from Hedin's equations [59] by setting the vertex function to a Dirac δ-function. In general, this methodology improves the underestimation of band gaps by DFT.

To actually compute the self-energy corrections, the common implementation takes advantage of the fact that DFT wave functions are very similar to actual quasiparticle states [60–62]. Using these DFT orbitals and energies, one spectrally constructs the mean-field Green's function (G^0) according to

$$G^0(\mathbf{r},\mathbf{r}';E) = \sum_i \frac{\psi_i(\mathbf{r})\psi_i^*(\mathbf{r}')}{E-\epsilon_i} \tag{1.7}$$

with DFT orbitals $\psi_i(\mathbf{r})$ and energies ϵ_i. In a non-self-consistent calculation, the dressed Green's function $G(\mathbf{r},\mathbf{r}';E)$ is approximated as this bare Green's function $G^0(\mathbf{r},\mathbf{r}';E)$, and the self-energy is computed in frequency space as

$$\Sigma(\mathbf{r},\mathbf{r}';E) = \frac{i}{2\pi}\int dE' G^0(\mathbf{r},\mathbf{r}';E+E')W(\mathbf{r},\mathbf{r}';E') \tag{1.8}$$

W contains the screened Coulomb and exchange interactions using the independent-particle polarizability P^0 (RPA). By including the self-energy corrections and/or replacing DFT orbitals with quasiparticle wave functions, one can construct a higher-order Green's function, recalculate Σ, and iterate until numerical convergence is reached. While a self-consistent solution is always necessary in principle, often times only a single iteration gives quasiparticle energies that compare well with experiment.

1.3.4 Bethe-Salpeter equation

The GW approximation accurately describes quasi-electron addition or removal processes. Optical absorption or emission processes result in the creation/annihilation of neutral excitations – excitons – that are superpositions of quasi-electron/quasi-hole pairs. Therefore, to accurately describe optical processes, the GW approximation is not adequate and the electron-hole interaction must be included. Based on the equation of motion for the two-particle Green's function [27, 28, 62–64], the Bethe-Salpeter equation (BSE) takes the form

$$(E^{QP}_{c\mathbf{k}} - E^{QP}_{v\mathbf{k}})A^S_{vc\mathbf{k}} + \sum_{v'c'\mathbf{k}'}\langle vc\mathbf{k}|K^{\mathrm{eh}}|v'c'\mathbf{k}'\rangle A^S_{v'c'\mathbf{k}'} = \Omega^S A^S_{vc\mathbf{k}} \tag{1.9}$$

where $A^S_{vc\mathbf{k}}$ is the s^{th} exciton eigenstate in the quasiparticle basis, K^{eh} is the electron-hole interaction kernel, and Ω^S is the excitation energy. K^{eh} is analogous to the self-energy in the single particle case. The exciton created upon the absorption of a photon is expressed in real space as

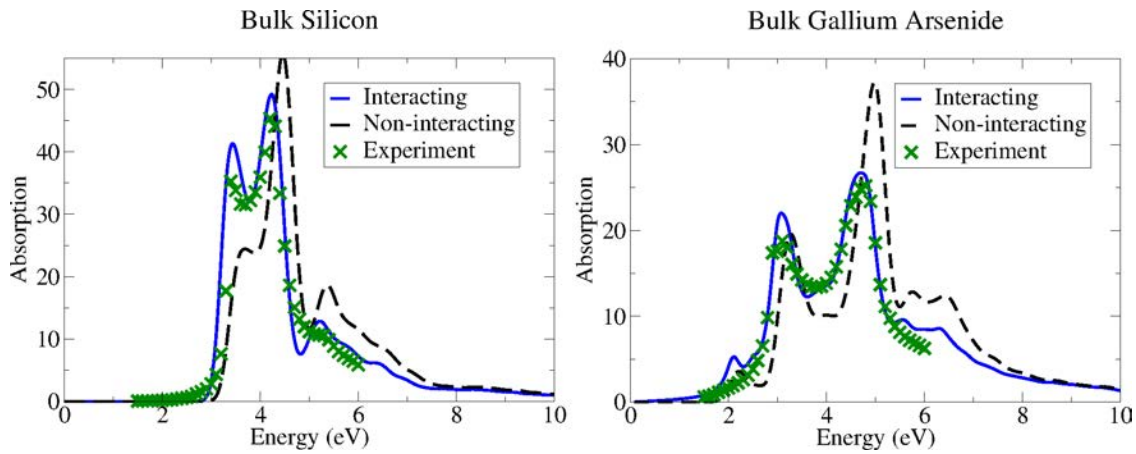

Figure 1.4: Optical absorption of Si and GaAs computed at the Bethe-Salpeter level.

$$\Psi(\mathbf{r}_e, \mathbf{r}_h) = \sum_{\mathbf{k},c,v} A^S_{vc\mathbf{k}} \psi_{\mathbf{k},c}(\mathbf{r}_e)\psi^*_{\mathbf{k},v}(\mathbf{r}_h). \tag{1.10}$$

The imaginary part of the dielectric function, which is directly comparable with experiment, is computed as transitions from the ground state to exciton states,

$$\epsilon_2(\omega) = \frac{16\pi^2 e^2}{\omega^2} \sum_S |\mathbf{e} \cdot \langle 0|\mathbf{v}|S\rangle|^2 \delta(\omega - \Omega^S), \tag{1.11}$$

where $\mathbf{v}$ is the single particle velocity operator, $\mathbf{e}$ is the incident field polarization, and $|S\rangle$ is an exciton state. To better match experiment, artificial thermal broadening modifies this absorption spectrum from a discrete set of Dirac-delta functions to a continuous spectrum of Lorentzian peaks. Figure 1.4 shows the computed absorption spectra of two common semiconductors, Si and GaAs.

Diagonalizing the two-particle Hamiltonian also yields the exciton binding energy (E_b), the difference between the quasiparticle band gap and the lowest excitation energy, Ω^S. This energy must be provided to separate the electron and hole and release free charge carriers in a material. Hence, it is an important design parameter in optoelectronic devices. Recent work has shown that simple descriptions of excitons based on effective mass models cannot adequately predict trends in E_b [65]. Solving the Bethe-Salpeter equation, however, can accurately match experimental values of E_b and is necessary for accurate predictions of untested materials. The complete DFT-GW-BSE methodology is summarized in Figure 1.5.

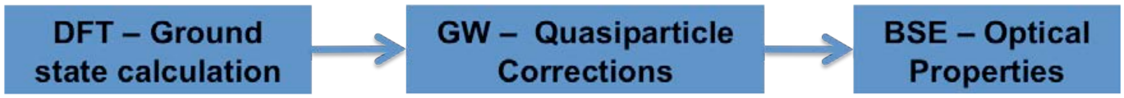

Figure 1.5: The computational methodology for describing quasiparticle addition/removal processes and optical absorption/emission processes.

1.3.5 Topological insulators

Because topological insulators (TI) are such a new field, a brief discussion of their properties will benefit the reader's understanding of Chapter 6. Topological insulators are a newly discovered electronic phase of matter that are distinguished from their ordinary counterparts, non-topological (or trivial) insulators, by the idea of adiabatic continuity. By deforming the Hamiltonian, insulators belonging to the same topological class may be connected to each other without undergoing band gap closure at any point in between. Geometrically, this is analogous to deforming a torus into a coffee mug – both possess one opening, and hence are topologically equivalent. In contrast, insulators belonging to different topological classes can only be connected along an adiabatic path which causes band gap closure at some point between the two phases. Returning to the geometric analogy, adiabatically connecting one insulator to a topologically distinct insulator is analogous to deforming a torus into a sphere. Because the opening in the torus must be closed in this deformation, the torus and sphere are topologically distinct. For a topological insulator, the point of band gap closure that separates two insulating phases that belong to different topological classes is analogous to removing the opening in the torus.

Similar to the genus in geometric topology, the topological class of an insulator can be characterized by a single integer. In the case of the Chern insulator, this integer is the Chern number, which is related to the Berry phase or Berry curvature. Suppose that some Hamiltonian H is characterized by a set of parameters $\mathbf{R}(t)$ that depend on time. The Berry phase of the eigenstate $|\psi(t)\rangle = e^{-i\theta(t)}|n(\mathbf{R})\rangle$ is the phase change of $|\psi(t)\rangle$ upon completing a closed path $\mathcal{C}$ in the parameter space defined by $\mathbf{R}$. The Berry phase is *distinct* from the ordinary phase associated with the time evolution of a quantum system; together, they give the *total* phase change of the wave function. For $\mathcal{C}$ to be closed, the configuration $\mathbf{R}(t)$ at the initial (t_0) and final (t_f) times must be the same. The change in phase acquired along such a path not due to normal time evolution, γ_n, can be expressed in terms of the Berry vector potential, $\mathbf{A}_n(\mathbf{R})$. In three dimensions,

$$\mathbf{A}_n(\mathbf{R}) = i\langle n(\mathbf{R})|\frac{\partial}{\partial \mathbf{R}}|n(\mathbf{R})\rangle \quad ; \quad \gamma_n = \int_{\mathcal{C}} d\mathbf{R}\cdot \mathbf{A}_n(\mathbf{R}) \tag{1.12}$$

Because the wave function must be single valued at the beginning and end of any closed contour, the Berry phase can only equal $2\pi m$, where m is an integer called the Chern number, but m is *not* necessarily 0. In analogy with electromagnetics, the Berry curvature $\Omega_n(\mathbf{R})$ is the curl of the Berry vector potential. By application of Stokes' theorem, the Berry phase also equals the integral of $\Omega_n(\mathbf{R})$ over the surface $\mathcal{S}$ bounded by the curve $\mathcal{C}$.

$$\Omega_n(\mathbf{R}) = \nabla_{\mathbf{R}} \times \mathbf{A}_n(\mathbf{R}) \quad ; \quad \gamma_n = \int_{\mathcal{S}} d\mathbf{S}\cdot \Omega_n(\mathbf{R}) \tag{1.13}$$

In cases when $m \neq 0$ (a non-trivial insulator), singularities in the Berry curvature represent obstructions to gauge smoothing the wave functions. In other words, it is not possible to choose a gauge that is continuous and single valued over the entire space $\mathbf{R}$ that would give $m = 0$.

In a crystal, the wave vector $\mathbf{k}$ of a given Bloch state can be interpreted as the parameters $\mathbf{R}$; generally, Hamiltonians for periodic systems are $\mathbf{k}$-dependent. If we allow $\mathbf{k}$ to vary over all possible values in the Brillouin zone, integrating $\Omega_n(\mathbf{k})$ over the BZ gives the Chern number for the band that $|\psi\rangle$ belongs to. Summing the Chern numbers over all occupied states gives the total Chern number of the material. At the point of band gap closure along the adiabatic deformation of the Hamiltonian, Chern numbers can effectively be 'passed' between occupied and unoccupied bands, separating the two insulating phases on either side of the band gap closure into topologically distinct phases.

As a consequence of their Chern number, Chern insulators possess very unusual edge states. Consider two insulators, with different Chern numbers equal to 0 and +1, and place them next to each other. Far from the interface between these two materials and into each bulk, we know each material is an insulator with its respective Chern number. Each band carries its own Chern number, with the total Chern number equal to the sum over all occupied bands. At the interface, the composite material must transition from a trivial insulator to a topological one. Therefore, at the interface, the occupied band carrying Chern value +1 in the topological insulator must cross the Fermi energy and become an unoccupied band in the trivial insulator. This leaves the sum of Chern values over occupied bands in the trivial insulator at zero, and the topological order far into the bulk of each material is preserved. For this reason, Chern insulators have metallic edge states that cross the Fermi energy. By placing edges on a material and creating a ribbon geometry, one can verify if a material is a non-trivial insulator by looking for the appearance of edge states that traverse the band gap.

In this research, our interest is in the quantum spin Hall insulator. The QSH insulator can be thought of as two Chern insulators with opposite Chern numbers for different spins. For spin up, the Chern number in the QSH phase is +1, while for spin down, the Chern number is -1. Because their Chern numbers are of opposite sign, the edge bands corresponding to different spins cross the band gap in opposite directions. Therefore, in the QSH phase, edge bands not only cross the band gap but are also spin-filtered, since each band with a given spin only crosses the band gap in a single direction. For both spins, the total Chern number of the QSH insulator is zero. The QSH is therefore classified by a different topological invariant, the Z_2 index, which only takes two values, even (trivial) or odd (non-trivial). The appearance of spin-filtered edge states that cross the band gap indicate the existence of a Z_2 odd, topologically non-trivial phase.

CHAPTER 2

BAND GAP OPENING BY PATTERNING GRAPHENE

Adapted from an article published as

Scientific Reports **3**, 2289 (2013).

Marc Dvorak [1,2,3], William Oswald[1,2], and Zhigang Wu[1,2,3]

Owing to its remarkable electronic and transport properties, graphene has great potential of replacing silicon for next-generation electronics and optoelectronics; but its zero band gap associated with Dirac fermions prevents such applications. Among numerous attempts to create semiconducting graphene, periodic patterning using defects, passivation, doping, nanoscale perforation, etc., is particularly promising and has been realized experimentally. However, despite extensive theoretical investigations, the precise role of periodic modulations on the electronic structure of graphene remains elusive. Here, we employ both tight-binding modeling and first-principles electronic structure calculations to show that the appearance of a band gap in patterned graphene has a geometric origin. Thus, the analytic rule for gap opening by patterning graphene is derived, which indicates that if a modified graphene is a semiconductor, its two corresponding carbon nanotubes, whose chiral vectors equal graphene's supercell lattice vectors, are both semimetals.

2.1 Introduction

Graphene has risen as a fascinating system in condensed matter physics for not only fundamental science but also technological applications [1, 45, 66] because of its many unique and amazing properties originating from its massless fermions [45, 67] due to the linear dispersion of energy bands near the Dirac points (**K**). For example, under gate voltage, charge

[1]Department of Physics, Colorado School of Mines
[2]Researcher
[3]Author

carriers in graphene can be tuned continuously between electrons and holes [1], and their mobilities exceed 2.5×10^5 cm^{2}V^{-1}s^{-1} under ambient conditions [68]. This certainly makes graphene extremely attractive for electronic and optoelectronic applications [66]; however, graphene is a semimetal with band gap (E_{g}) closing at $\mathbf{K}$, which prohibits switching of the graphene channels in field-effect transistors and building functional junctions in graphene optoelectronics.

Extraordinary efforts [6, 20, 26, 69–75] have been spent to create semiconducting graphene materials that maintain its exceptional transport property. One scheme is to create a band gap through quantum confinement in graphene nanoribbons [69] (GNRs). But it is difficult to control the magnitude of the band gap in GNRs, since E_{g} is very sensitive to the ribbon edge and width. Moreover, a narrow GNR, which is necessary for a sizable gap, cannot carry sufficiently large currents, making it unattractive for devices. Other methods include substrate-induced [70, 71] and strain-induced [72] band gaps, but the former is essentially not tunable, while the latter is practically limited by the ability to tune E_{g} to the desired value. An alternative approach is to periodically modify graphene [76], which is crucial to preserve its anomalously high charge carrier mobilities, by normal or inverse Stone-Thrower-Wales types of defects [20, 21, 23, 73], hydrogen passivation [74], boron and nitrogen doping [26], or nanoscale holes creating graphene nanomeshes [6, 75, 76] (GNMs). In particular, Balog *et al.* [74] demonstrated the existence of a band gap in graphene with patterned hydrogen adsorption, and Bai *et al.* [6] made functional GNM field-effect transistors capable of supporting currents 100 times of those in GNR-based devices.

However, it is still a mystery why periodically modified graphene can either open a substantial gap or remain gapless (or a tiny gap) if its supercell lattice changes only slightly [10–19, 77], which complicates the creation of a band gap by patterning defects. The observed behavior so far is also apparently at odds with the proposal that the band gap in these graphene structures is due to quantum confinement between neighboring modulated sites [6]. A general description of quantum confinement that results in an energy gap in patterned graphene is missing; instead, previous theoretical investigations [10–19, 77] mainly focused on some special patterns whose supercell lattices form rectangular or hexagonal structures. A number of interesting empirical rules have been discovered, but a fundamental and precise understanding of how electronic structure is affected by regularly patterning graphene has not yet been achieved.

2.2 Results

2.2.1 Analytic theory

In this work we adopt and extend the tight-binding model [45], which describes the sp^2 bonding in graphene extremely well, to include periodic structural alterations modeled by an external potential $U(\mathbf{r})$ applied to graphene [78]. We denote the primitive lattice vectors of pristine graphene by $\mathbf{a}_1$ and $\mathbf{a}_2$, and the supercell lattice vectors of the patterned graphene can be written as

$$\begin{aligned} \mathbf{R}_1 &= n_1\mathbf{a}_1 + m_1\mathbf{a}_2 \\ \mathbf{R}_2 &= n_2\mathbf{a}_1 + m_2\mathbf{a}_2 \end{aligned} \tag{2.1}$$

with (n_1, m_1, n_2, m_2) four integers. If the defect sites form two-dimensional Bravais lattices, then the external potential $U(\mathbf{r})$ has the same translational symmetry

$$U(\mathbf{r}) = U(\mathbf{r} + l_1\mathbf{R}_1 + l_2\mathbf{R}_2) \tag{2.2}$$

where l_1 and l_2 are integers. The Fourier components of $U(\mathbf{r})$, $U(\mathbf{k})$, determine the non-zero scattering matrix elements between Bloch states.

At Dirac points $\mathbf{K}$ and $\mathbf{K}'$, the intrinsic tight-binding off-diagonal matrix elements $tf(\mathbf{k})$ of graphene vanish, giving rise to a zero band gap. A non-vanishing $U(\mathbf{K})$, the Fourier transform of $U(\mathbf{r})$ evaluated at the Dirac points, satisfies conservation of crystal momentum for scattering between Dirac points and results in an energy gap. A detailed discussion of this condition and the previous model are presented in Supplementary Information. This leads to the following band gap opening rule:

$$
\begin{aligned}
n_1 - m_1 = 3p \quad \text{and} \quad n_2 - m_2 = 3q, \qquad & \text{(Gap opening)} \\
\text{Otherwise,} \qquad & \text{(Gap closure)}
\end{aligned}
\tag{2.3}
$$

where p and q are integers. A derivation of this band gap opening condition is presented in Supplementary Information.

Equation 2.3 indicates that only one ninth of arbitrarily patterned graphenes are semiconducting while the rest remain semimetallic; thus the patterning periodicity must be carefully chosen to create a gap. Furthermore, Equation 2.1 suggests that a patterned graphene can be mapped to a pair of carbon nanotubes [79] (CNTs) with chiral vectors $\mathbf{C}_h$ equal to $\mathbf{R}_1$ and $\mathbf{R}_2$ respectively; then band gap opening in a patterned graphene has an exactly opposite correlation to that in CNTs: it possesses a sizable band gap only if *both of its corresponding CNTs are gapless* at the tight-binding level.

We illustrate our analytic theory by discussing a crucial and representative class of patterned graphene, namely GNMs. Figure 2.1 plots various primitive cells of GNMs, which are parallelograms with different angles, side lengths, and orientations with respect to the underlying graphene lattice. Because of the honeycomb structure of graphene, 60° and 90° (rectangular) parallelograms are especially important because of their high symmetry which makes them easier to realize experimentally [6, 75]. Like other patterned graphenes, a GNM can be mapped to two CNTs. Since unfolding a CNT generates a GNR, a GNM can also be mapped to a pair of GNRs, as illustrated in Figure 2.1g and h. Experimentally, GNRs have been created by unzipping CNTs longitudinally [80], whereas CNTs could also be produced by wrapping GNRs around [81]. A GNR and its corresponding CNT have similar dependence of electronic band structure on their transverse vectors, and their well-known three-fold alternation in electronic structure is not surprising, given the hexagonal symmetry of graphene [45].

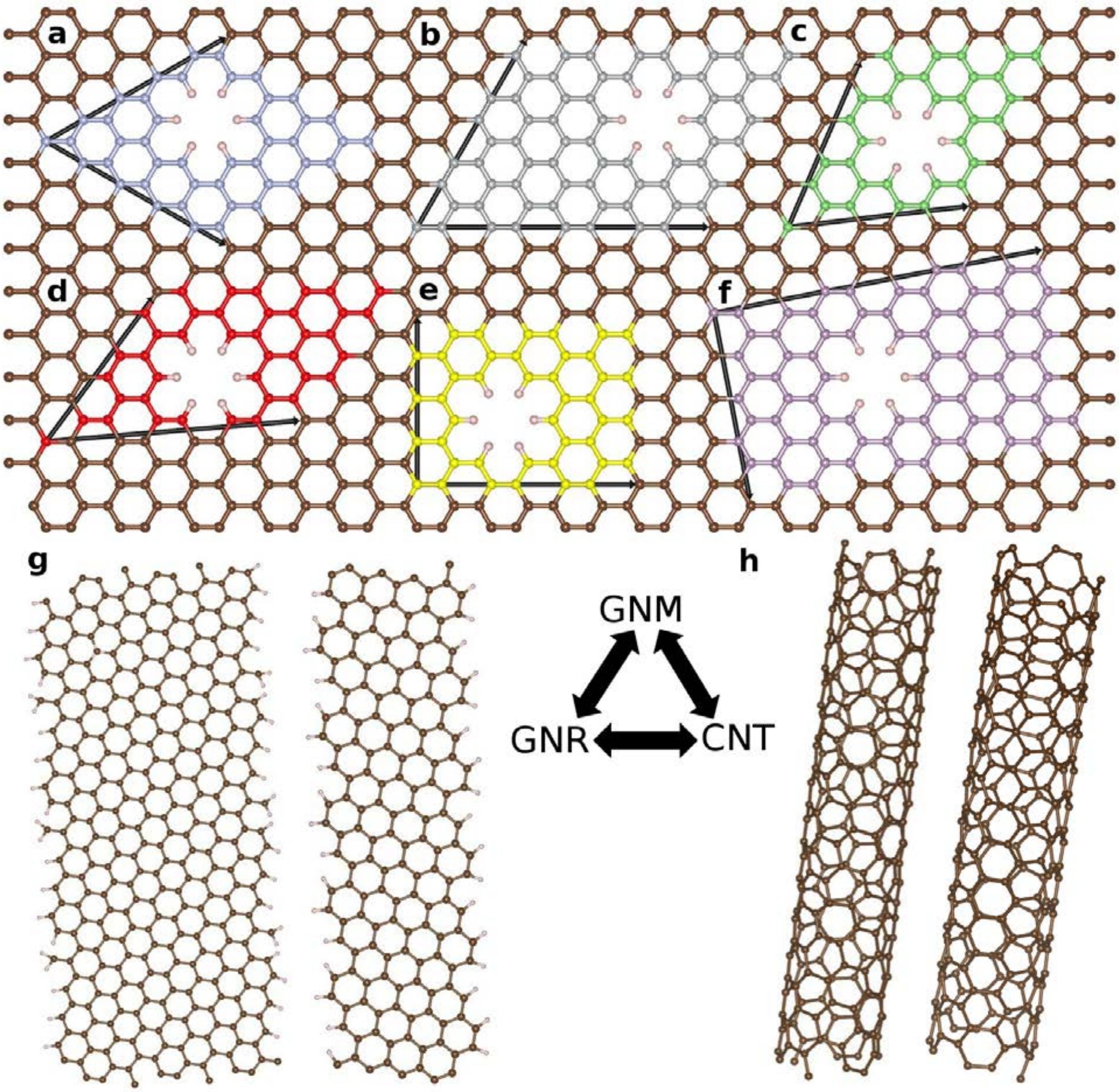

Figure 2.1: Primitive cells of GNMs. (a,b,c) 60° parallelograms, with two lattice vectors along the zigzag (blue), armchair (gray), and chiral (green) directions, respectively. (d) Oblique parallelogram (red). (e,f) Rectangles whose lattice vectors are along the zigzag and armchair directions, respectively (yellow), or along two chiral directions (purple). Dangling bonds in GNMs and GNRs are passivated by hydrogen atoms (small gray dots), while carbon atoms are denoted by brown dots. (g,h) The relationship among GNMs, GNRs, and CNTs, as explained in the text.

However, a GNM's (or other type of patterned graphene) dependence of band gap opening on supercell lattice vectors is opposite to that of its corresponding CNTs (or GNRs). Along each lattice vector of a GNM the matching condition on Dirac points is exactly the same as the circular confinement condition of a CNT. A CNT is characterized by its chiral vector defined by a pair of integers (n, m): $\mathbf{C}_h = n\mathbf{a}_1 + m\mathbf{a}_2$. The tight-binding model asserts that a CNT is semimetallic if $n - m \equiv 0 \bmod 3$, or semiconducting otherwise [79], since its allowed $\mathbf{k}$ points must satisfy $\mathbf{k} \cdot \mathbf{C}_h = 2\pi l$ with l integers. Figure 2.2 d-f illustrates that only when these lines of $\mathbf{k}$ points pass through graphene's Dirac points $\mathbf{K}$, a CNT remains semimetallic. On the other hand, as shown in Figure 2.2 g-i, the reciprocal lattice vectors of a GNM are the intersection of two sets of parallel lines representing the allowed $\mathbf{k}$ points of its two matching CNTs. To create a band gap, the reciprocal lattice vectors of a GNM must overlap the Dirac points, requiring both sets of parallel lines to pass through $\mathbf{K}$ and $\mathbf{K}'$; consequently, a semiconducting GNM corresponds to two semimetallic CNTs.

2.2.2 First-principles calculations

In the following, we demonstrate that the above conclusion drawn from analytic modeling is in qualitative agreement with first-principles results. We present electronic structures obtained using density functional theory (DFT [53, 54]) for GNMs; in addition, our DFT calculations on periodically H-passivated and boron nitrogen doped graphene show similar results, which will be presented in Chapter 3. Although it is well known that DFT can severely underestimate band gaps in semiconductors and insulators, DFT makes good predictions on the trends of electronic band structures and band gap [58]. In particular, DFT correctly predicts a zero band gap (closing at the Dirac points) for pristine graphene [45], and the predicted trends for band gaps and band structures in graphene-based nanostructures, such as CNTs and GNRs, are mostly correct, compared with many-body perturbation theory within the GW approximation and experimental data [69, 79, 82]. If these materials are semimetallic (or nearly semimetallic), DFT predicts them to have zero (or nearly zero) band gap; on the other hand, if they are semiconductors, DFT predicts sizable E_g which tends to be underestimated. A list of DFT band gaps for several different GNMs is presented in Table 2.1.

Figure 2.2 j-l compares DFT electronic band structures of three oblique GNMs with $(n_1, m_1, n_2, m_2) = (9, -3, -4, 9), (7, 4, -4, 8), (9, -2, -4, 9)$, whose crystal structures are shown in Figure 2.2 g-i, respectively. Although these three GNMs have the same holes and similar primitive cells, only the middle one has a substantial gap because its two matching CNTs are semimetallic. The left GNM corresponds to one metallic and one semiconducting CNT and has a tiny gap at M_2 and is nearly semimetallic; the GNM on the right remains gapless, with both of its matching CNTs semiconducting. These first-principles results qualitatively agree with our analytic theory, clearly demonstrating the sensitivity of band structure to patterning periodicity. They also suggest that, in a GNM, the top valence bands and bottom conduction bands derived from the π orbitals are nearly symmetric with respect to the Fermi energy (or the middle of energy gap), consistent with the tight-binding model for graphene in which only the nearest-neighbor interactions are taken into account.

Next we discuss rectangular and hexagonal GNMs, which have a one-to-one correspondence to CNTs, because their lattice vectors $\mathbf{R}_1$ and $\mathbf{R}_2$ are not independent. $\mathbf{R}_1$ and $\mathbf{R}_2$ for a rectangular GNM form the chiral and translational ($\mathbf{T}$) vectors of a CNT subject to an integer multiplier j: $\mathbf{R}_1 = \mathbf{C}_h$ and $\mathbf{R}_2 = j\mathbf{T}$, or $\mathbf{R}_1 = j\mathbf{T}$ and f$\mathbf{R}_2 = \mathbf{C}_h$. Here $\mathbf{T} = t_1\mathbf{a}_1 + t_2\mathbf{a}_2$, with $t_1 = (2m+n)/t$, $t_2 = -(2n+m)/t$, and t is the greatest common divisor of $2m+n$ and $2n+m$. If $n-m$ is not a multiple of 3, then $t_1 - t_2 \equiv 0 \bmod 3$, so that the existence of a band gap in a rectangular GNM depends only on $\mathbf{R}_1$ by the difference between n_1 and m_1: it is semiconducting if $n_1 - m_1 \equiv 0 \bmod 3$ or semimetallic otherwise, exactly in contrast to a CNT with $\mathbf{C}_h = \mathbf{R}_1$, as summarized in Figure 2.3i. The DFT band structures of two rectangular GNMs (Figure 2.3a and b) with $(n_1, m_1 n_2, m_2) = (6, 3, -4, 5)$ and $(6, 4, -7, 8)$ are plotted in Figure 2.3e and f. In both cases, $n_2 - m_2$ is divisible by 3; the former is a semiconductor with a direct gap at the Γ point, while the latter is semimetallic with the Dirac point folding along the $\Gamma - M_2$ segment. In fact, all semiconducting GNMs open direct band gaps at the Γ point.

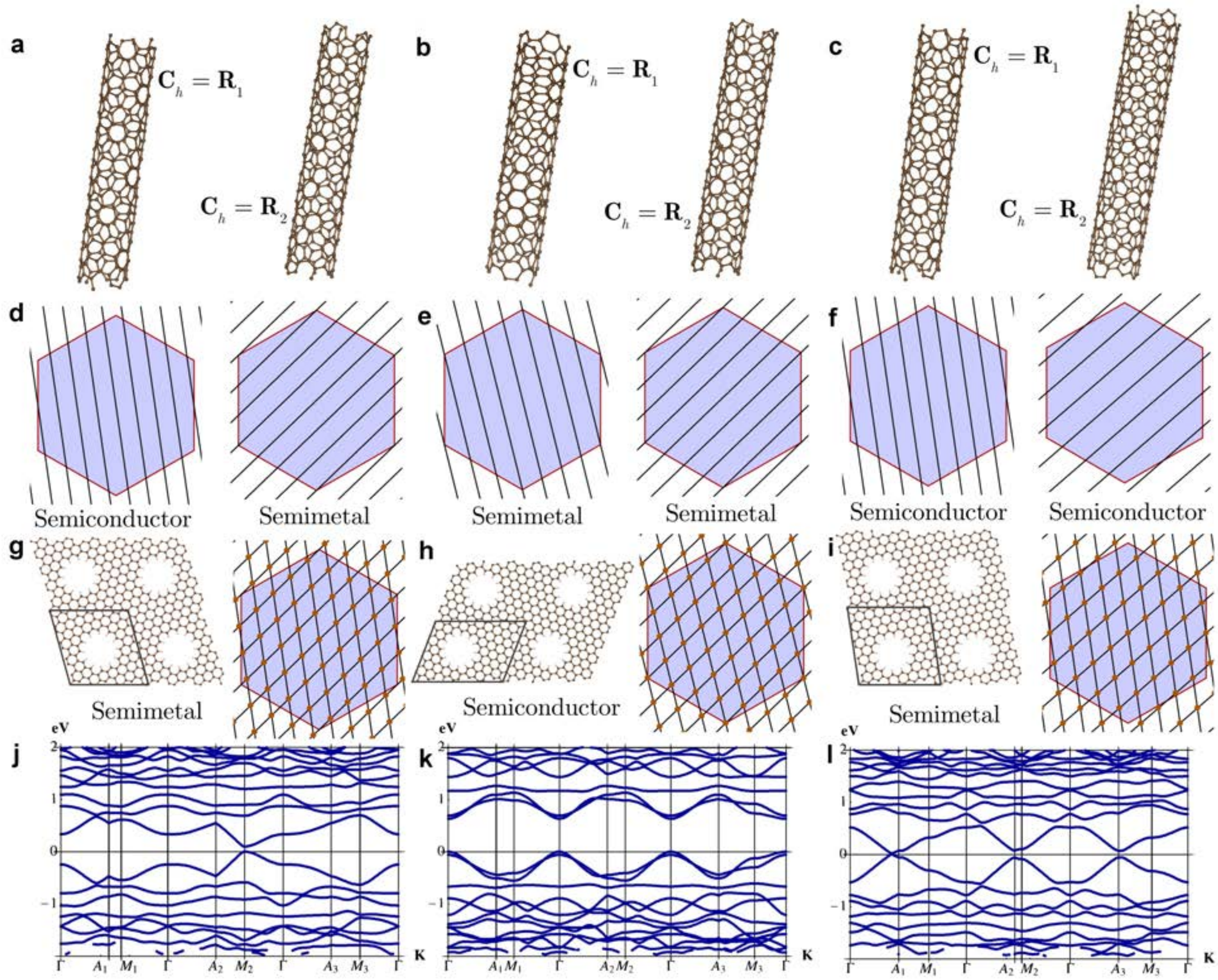

Figure 2.2: Band gap opening/closure in GNMs and their corresponding CNTs. (a-c) Crystal structures of a pair of CNTs in each panel, whose chiral vectors are equal to the lattice vectors of GNMs plotted on the left side of (g-i), and whose allowed **k**-points (parallel lines) are plotted in (d-f), respectively. The right side of (g-i) show the reciprocal lattices of GNMs plotted in (a-c), respectively. In (d-i), the hexagons indicate the Brillouin zone of pristine graphene, with its 6 corners the Dirac points. (j-l) Electronic band structures of GNMs plotted in (g-i), respectively. Brillouin zones of all GNMs in the text are plotted in Figure 2.5

In a rectangular GNM, $\mathbf{R}_1$ and $\mathbf{R}_2$ are perpendicular to each other with *conjugate* chiralities so that at least one of its two matching CNTs is metallic, and then one third of rectangular GNMs are semiconducting. On the other hand, a 60° parallelogram GNM's lattice vectors $\mathbf{R}_1$ and $\mathbf{R}_2$ have the same chirality subject to integer multipliers. In general, we cannot assign a pair of integers to characterize a 60° parallelogram GNM because $\mathbf{R}_1$ and

$\mathbf{R}_2$ might be different in length. For $\mathbf{R}_1$ and $\mathbf{R}_2$ with the same length, a 60° parallelogram becomes a 60° rhombus and such GNMs have hexagonal symmetry, in which $n_1 - m_1$ and $n_2 - m_2$ are either both divisible or neither divisible by 3. Therefore the existence of a band gap in a hexagonal GNM with equal side lengths also depends only on $\mathbf{R}_1$ via $n_1 - m_1$, and one third of them possess band gaps, compared with only one ninth of all possible 60° parallelogram GNMs. Figure 2.3g and h plot DFT band structures of two hexagonal GNMs (Figure 2.3c and d) with $(n_1, m_1, n_2, m_2) = (5, 4, 9, -5)$ and $(7, 1, 8, -7)$, respectively. As predicted by Equation 2.3, the former is semimetallic, while the latter is a semiconductor.

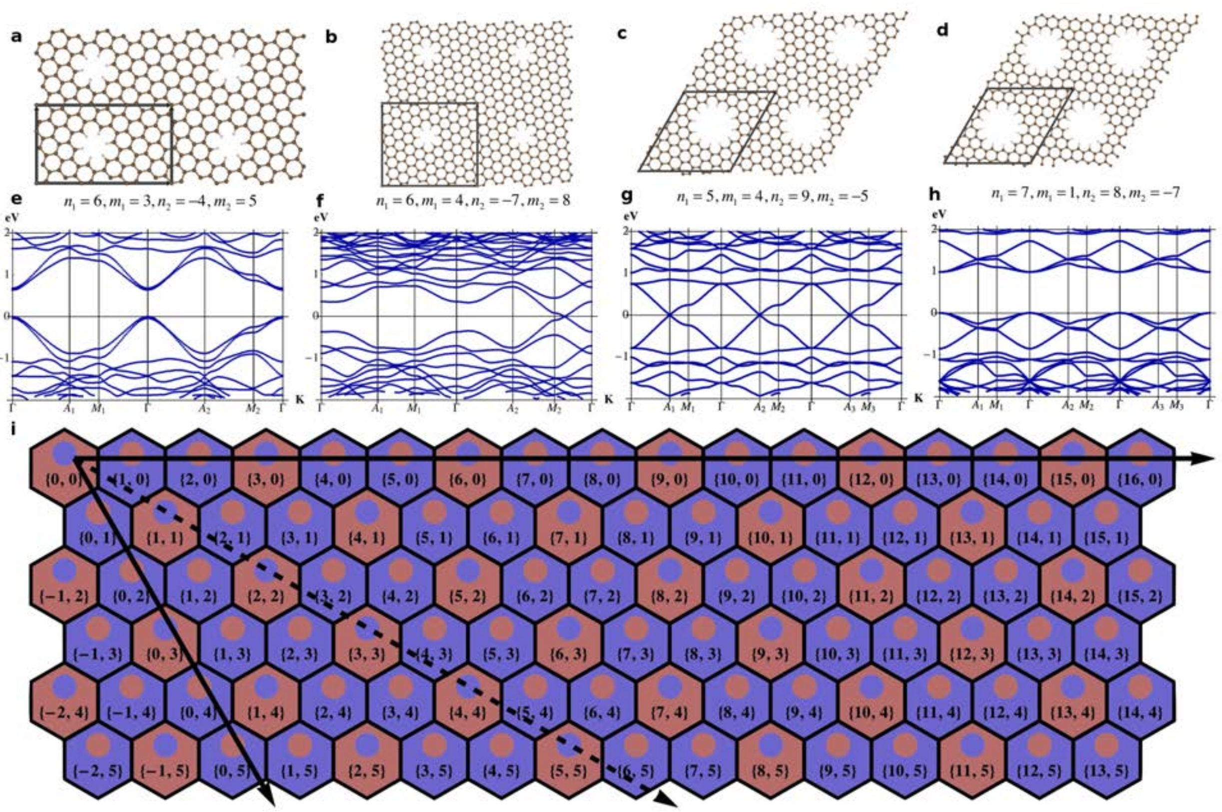

Figure 2.3: Rectangular and hexagonal GNMs. (a,b) Crystal structures of two rectangular GNMs; (e,f) are the corresponding electronic band structures. (c,d) Crystal structures of two hexagonal GNMs; (g,h) are the corresponding electronic band structures. (i) Band gap opening (red) and closure (blue) for rectangular and hexagonal GNMs (hexagons) and CNTs (circles) chracterized by (n_1, m_1) for vector $\mathbf{R}_1$ of GNMs and $\mathbf{C}_h$ of CNTs, respectively, i.e. $\mathbf{C}_h = \mathbf{R}_1 = n_1\mathbf{a}_1 + m_1\mathbf{a}_2$. Here the solid arrows in (i) denote the zigzag direction, while the dashed arrow indicates the armchair vector.

Previous theory and simulations [10–19, 77] studied many special GNMs, namely the zigzag (Figure 2.1a), armchair (Figure 2.1b), and zigzag-armchair (Figure 2.1e) GNMs, in which $\mathbf{R}_1$ and $\mathbf{R}_1$ are both along the zigzag or armchair directions, or along zigzag and armchair directions respectively. A zigzag GNM is characterized by a pair of integers (Z_1, Z_2) with $(n_1, m_1, n_2, m_2) = (Z_1, 0, 0, Z_2)$, an armchair by (A_1, A_2) with $(n_1, m_1, n_2, m_2) = (2A_1, -A_1, A_2, A_2)$ and a zigzag-armchair by (Z, A) with $(n_1, m_1, n_2, m_2) = (Z, -Z, A, A)$. The band gap opening rules for these special cases as functions of structural parameters A and Z are presented in Figure 2.4e, f, and j, respectively. One third of zigzag-armchair GNMs are semiconducting, a result that is independent of the value of A and depends only on whether $Z \equiv 0 \bmod 3$. A zigzag GNM acquires a band gap if both $Z_1 \equiv 0 \bmod 3$ and $Z_2 \equiv 0 \bmod 3$, so only one ninth of them are semiconducting, whereas *all* armchair GNMs are semiconductors regardless of the values of A_1 and A_2. These predictions have been verified by previous and present DFT calculations whose results are plotted in Figure 2.4a-d, g, and h. Comparing band structures plotted in Figures 2-4, one finds that for the same patterning geometry, semiconducting graphene alternates with semimetallic ones, except for the armchair case where all of them are semiconductors. Apparently, the armchair structure is the preferred choice to open a band gap by patterning graphene.

We have carried out additional DFT calculations for electronic structures of other patterned graphenes with a variety of primitive cells and defect sizes other than what is reported in Figures 2.2-2.4. All these results (in Supplementary Information) agree with Equation 2.3 on band gap existence. Furthermore, the magnitude of the band gap of a semiconducting patterned graphene depends on the on-site perturbation strength and inter-site distances; in particular, E_g of GNMs as functions of hole size and primitive cell area can be well fitted to a simple scaling rule proposed by Pedersen *et al.* [12], as demonstrated in Figure 2.4i. Hence, once a semiconducting patterning is chosen, E_g can be tuned to the ideal value for target applications by adjusting the type, size of, and distance between structural modulations.

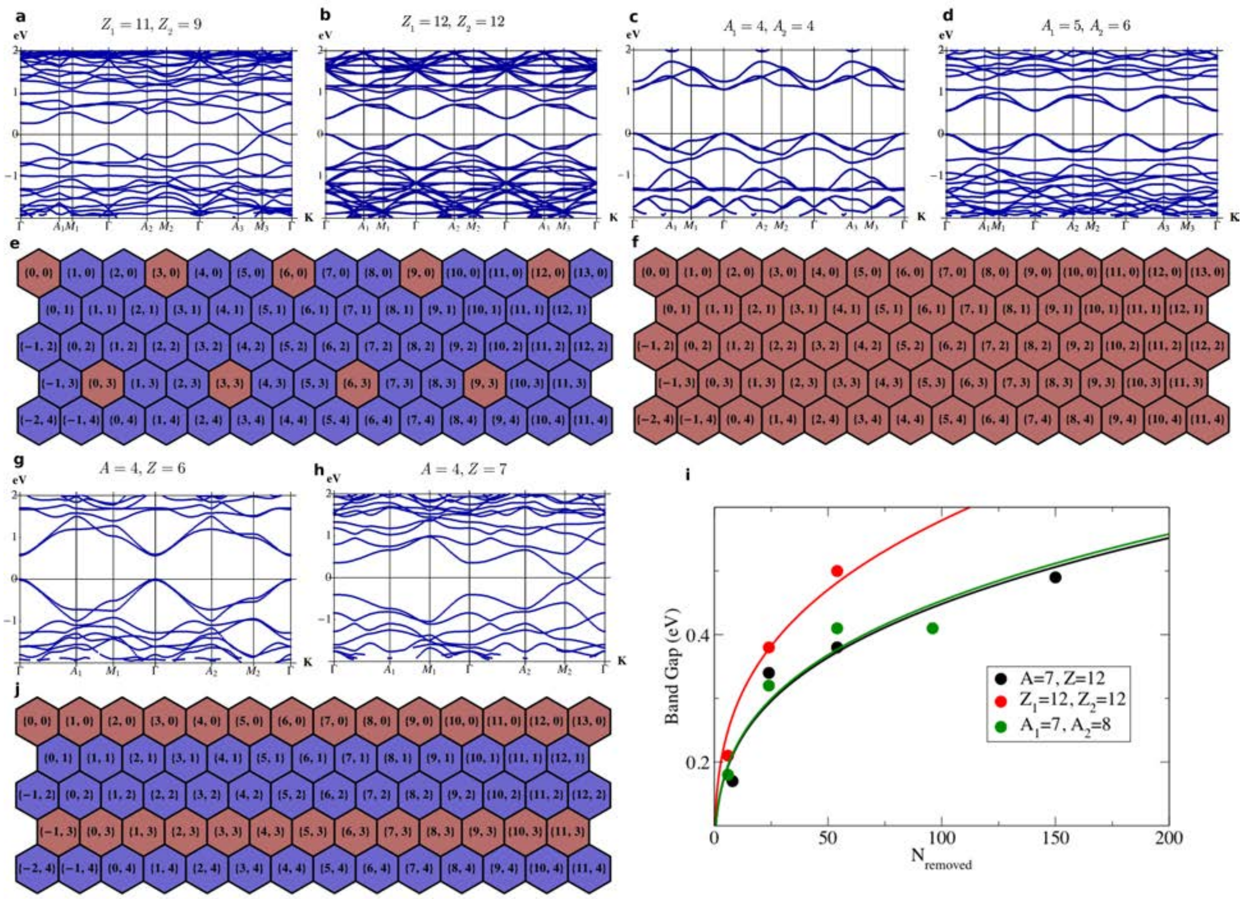

Figure 2.4: Zigzag, armchair, and zigzag-armchair GNMs. Electronic band structures of two zigzag (**a,b**), armchair (**c,d**), and zigzag-armchair (**g,h**) GNMs. Their crystal structures are plotted in Figure 2.6. **e,f,j** Band gap opening (red) and closure (blue) for zigzag (**e**), armchair (**f**), and zigzag-armchair (**j**) GNMs characterized by (Z_1, Z_2), (A_1, A_2), and (A, Z), respectively. **i** Band gap (eV) as a function of hole size indicated by the number of removed carbon atoms (N_{removed}) per primitive cell for a zigzag (red), an armchair (green), and a zigzag-armchair (black) GNM. Computed data (circles) are fitted to smooth curves, as described in Supplementary Information.

2.3 Discussion

Using a perturbatve tight-binding model we have derived a universal band gap opening rule for graphene with arbitrary Bravais lattice patterning. A simple reverse relation on existence of band gap between a modified graphene and its two analogous CNTs is found, which is confirmed by first-principles electronic structure calculations. Current modeling can be easily generalized from Bravais to non-Bravais supercells, such as the honeycomb structure, and thus the DFT results for the honeycomb GNMs [15] can also be well explained. We conclude that band gap opening in patterned graphene is not caused by quantum confinement as in CNTs or GNRs, though confinement may still play a role in determing the magnitude of E_{g} once a gap is present; instead, it originates from intervalley scattering between the Dirac points, leading to the exactly opposite band gap opening conditions between modified graphene and CNTs.

Our present work has solved an outstanding problem on how to properly pattern graphene to induce band gaps, pointing to practical routes of geometrically designing graphene with controllable and desirable electronic behavior. Previous experiments [6, 26, 74–76] have demonstrated that patterning graphene could open a substantial band gap suitable for transistors, but none of them have yet reported the predicted sensitivity of electronic behavior to patterning periodicity. Their patterned graphene structures are rather rough, which might greatly hamper transport of charge carriers, while a high-quality, accurate periodic patterning is expected to largely maintain the ultrahigh electron mobility. This requires the ability of tailoring graphene structrures precisely at the atomic scale [83] − an exciting and rapidly advancing frontier in nanoscience and nanotechnology for pushing electronics and optoelectronics towards ever smaller scales.

Finally, the restriction of our modeling, as well as the key to its success, is that the valence and conduction bands in graphene touch only at the Dirac points. In other materials with vanishingly small density of states near the Fermi energy or, equivalently, band gap closing only at a small discrete set of **k**-points, it should be possible to perturb all these touching **k**-points by application of defects. Moreover, it is appealing to investigate the effects of periodic perturbation and structural symmetry breaking on strongly-correlated materials showing intriguing quantum/topological orders, such as topological insulators, whose gapless surface states are protected by time-reversal symmetry and the topology of the material.

2.4 Methods

2.4.1 First-principles calculations

Our first-principles electronic structure calculations based on DFT were performed employing the SIESTA package [84] using a triple-ζ polarized atomic basis set for carbon atoms, whose numerical accuracy has been rigorously examined against the planewave-based VASP program [85]. The two-dimensional Brillouin zones of GNMs are sampled on a 2×2 Monkhorst-Pack **k**-grid with good convergence due to very large primitive cells. The generalized gradient approximation [86] is used for the exchange-correlation functional. All calculations are spin-polarized. GNM structures are optimized until the maximum atomic force is less than 0.02 eV/Å. Dangling bonds in GNMs are passivated by hydrogen atoms.

2.4.2 Tight-binding model

Graphene has two sublattices (A and B) whose Hamiltonian is written as

$$H_{\mathbf{k}} = \begin{pmatrix} E_0 & tf(\mathbf{k}) \\ tf^*(\mathbf{k}) & E_0 \end{pmatrix} \tag{2.4}$$

where E_0 and t are two parameters. The eigenvalues are

$$E_{\pm}(\mathbf{k}) = E_0 \pm t|f(\mathbf{k})| \tag{2.5}$$

$$|f(\mathbf{k})| = \sqrt{3 + 2\cos(\sqrt{3}k_y a) + 4\cos\left(\frac{\sqrt{3}}{2}k_y a\right)\cos\left(\frac{3}{2}k_x a\right)} \tag{2.6}$$

with $a \sim 1.42$ Å, the neighboring carbon-carbon distance. The structural modifications are modeled by an external periodic potential $U(\mathbf{r})$. If the scattering matrix element between two degenerate states at Dirac points $\mathbf{K}$ and $\mathbf{K}'$ [87, 88],

$$|\langle \mathbf{K}| U(\mathbf{r}) |\mathbf{K}'\rangle|^2 = |U(\mathbf{K}' - \mathbf{K})|^2 \cos^2(\theta_{\mathbf{K},\mathbf{K}'}/2), \tag{2.7}$$

is non-zero, where $\Theta_{\mathbf{K},\mathbf{K}'}$ is the angle between $\mathbf{K}$ and $\mathbf{K}'$, then there is a sizable band gap in defected graphene. Equation 2.7 leads to the same band gap opening criterion of $U(\mathbf{K}) \neq 0$.

2.5 Acknowledgments

The authors gratefully acknowledge financial support from USA Department of Energy (DOE) Early Career Award (No. DE-SC0006433). Computations were carried out at the Golden Energy Computing Organization (GECO) at Colorado School of Mines and at the National Energy Research Scientific Computing Center (NERSC).

2.6 Supplementary Information

2.6.1 Tight-binding model for pristine graphene

Graphene has two sublattices (A and B) with the tight-binding model Hamiltonian [1] written as

$$H^0_{\mathbf{k}} = \begin{pmatrix} E_0 & tf(\mathbf{k}) \\ tf^*(\mathbf{k}) & E_0 \end{pmatrix} \tag{2.8}$$

where E_0 and t are two parameters, defined by

$$E_0 \equiv \langle\phi_A| H^{(0)} |\phi_A\rangle = \langle\phi_B| H^{(0)} |\phi_B\rangle\,, \tag{2.9}$$

where ϕ_A and ϕ_B are orbitals on the A-site and B-site, and

$$t \equiv \langle\phi_A| H^{(0)} |\phi_B\rangle\,, \tag{2.10}$$

with ϕ_A and ϕ_B a pair of nearest-neighbor orbitals. The eigenvalues are

$$E^{(0)}_{\pm} = E_0 \pm t|f(\mathbf{k})| \tag{2.11}$$

where

$$|f(\mathbf{k})| = \sqrt{3 + 2\cos\left(\sqrt{3}k_y a\right) + 4\cos\left(\frac{\sqrt{3}}{2}k_y a\right)\cos\left(\frac{3}{2}k_x a\right)}, \tag{2.12}$$

with $a \sim 1.42$ Å, the neighboring carbon-carbon distance. At the Dirac points $\mathbf{K}$ and $\mathbf{K}'$, $f(\mathbf{K}) = f(\mathbf{K}') = 0$, leading to band gap closure. Pristine, undoped graphene has a single filled band corresponding to the $-$ sign in Equation 2.11, placing the Fermi energy at the Dirac points.

2.6.2 Perturbative model for graphene under periodic potential

We model the effects of periodic structural modifications on graphene by a periodic potential $U(\mathbf{r})$:

$$U(\mathbf{r}) = U(\mathbf{r} + l_1\mathbf{R}_1 + l_2\mathbf{R}_2), \tag{2.13}$$

where l_1 and l_2 are two integers, while $\mathbf{R}_1$ and $\mathbf{R}_2$ are lattice vectors defining the periodicity of the applied periodic potential (structural modifications):

$$\mathbf{R}_1 = n_1\mathbf{a}_1 + m_1\mathbf{a}_2 \quad ; \quad \mathbf{R}_2 = n_2\mathbf{a}_1 + m_2\mathbf{a}_2. \tag{2.14}$$

Here, (n_1, m_1, n_2, m_2) are integers, and $\mathbf{a}_1$ and $\mathbf{a}_2$ are the primitive translation vectors of pristine graphene.

$$\mathbf{a}_1 = \sqrt{3}a\left(\frac{\sqrt{3}}{2}, \frac{1}{2}\right) \quad ; \quad \mathbf{a}_2 = \sqrt{3}a\left(\frac{\sqrt{3}}{2}, -\frac{1}{2}\right) \tag{2.15}$$

We denote the periodic potential in reciprocal space by $U(\mathbf{k})$:

$$U(\mathbf{k}) = \frac{1}{2\pi}\int_{-\infty}^{\infty}\int_{-\infty}^{\infty} U(\mathbf{r})e^{-i\mathbf{k}\cdot\mathbf{r}}dxdy. \tag{2.16}$$

Treating the periodic potential as a perturbation to pristine graphene, the changes in the diagonal matrix elements are approximated as

$$E_1 \equiv \langle\phi_A| U(\mathbf{r}) |\phi_A\rangle = \langle\phi_B| U(\mathbf{r}) |\phi_B\rangle \tag{2.17}$$

where the last equality holds only if the perturbation affects both A and B sublattices equally. This is the case for all GNMs considered here. The on-site energy described by E_1 may be renormalized compared to that of pristine graphene, however. The perturbed Hamiltonian is

$$H^1_{\mathbf{k}} = \begin{pmatrix} E_0 + E_1 & \lambda_0 f(\mathbf{k}) + U(\mathbf{k}) \\ \lambda_0 f^*(\mathbf{k}) + U^*(\mathbf{k}) & E_0 + E_1 \end{pmatrix} \tag{2.18}$$

$U(\mathbf{k})$ is meant to conveniently and concisely represent the scattering matrix element between different Dirac points. Instead of constructing a large Hamiltonian explicitly coupling Bloch states with different momenta, inserting $U(\mathbf{k})$ on the off-diagonal correctly opens a band gap in the dispersion if scattering between Dirac points is allowed. A band gap opens only if $U(\mathbf{K}) \neq 0$, even though $f(\mathbf{K}) = 0$. If we are concerned *only* with scattering between Dirac points ($\mathbf{K}$ and $\mathbf{K}'$) or forward scattering at a Dirac point, the translational symmetry of $U(\mathbf{k})$ – not necessarily $U(\mathbf{k} - \mathbf{k}')$ – correctly describes the conditions for scattering.

Ordinarily, to conserve crystal momentum, two Bloch states with momenta $\mathbf{k}$ and $\mathbf{k}'$ have a non-zero scattering matrix element only if they can be connected by a reciprocal lattice vector, $\mathbf{k} - \mathbf{k}' = \mathbf{G}$. Here, we assume scattering off an external potential described by supercell vectors $\mathbf{R}_1$ and $\mathbf{R}_2$ with reciprocal lattice vectors $\mathbf{G}$. In graphene, however, $\mathbf{K}' = -\mathbf{K}$, so the condition $\mathbf{k} - \mathbf{k}' = \mathbf{G}$ becomes $\mathbf{K} - \mathbf{K}' = \mathbf{K} + \mathbf{K} = 2\mathbf{K} = \mathbf{G}$. Therefore, the condition for intervalley ($\mathbf{K} \leftrightarrow \mathbf{K}'$) scattering is that $\mathbf{K}$ and $\mathbf{K}'$ be included in the reciprocal lattice of the supercell described by $\mathbf{R}_1$ and $\mathbf{R}_2$. This is obviously the same as the condition for forward scattering at a single Dirac point when there is no momentum transfer between the initial and scattered states. Therefore, *both* scattering conditions are met if $U(\mathbf{k})$ is non-zero at the Dirac points. We now know that scattering is possible if $\mathbf{K}$ and $\mathbf{K}'$ are included in the supercell reciprocal lattice. We phenomenologically insert $U(\mathbf{k})$ into the tight-binding Hamiltonian to explicitly incorporate the translational symmetry of the supercell into the problem. In the following section, we derive the geometric conditions for which scattering between $\mathbf{K}$ and $\mathbf{K}'$ is allowed.

2.6.3 Band gap opening rule

We now find the geometric conditions for which $U(\mathbf{K}) \neq 0$, which is equivalent to including $\mathbf{K}$ in the reciprocal lattice of the supercell described by $\mathbf{R}_1$ and $\mathbf{R}_2$. Since we are concerned only with the conditions under which scattering is possible, we use a model potential based on a Dirac δ-function.

$$U(\mathbf{r}) = \sum_{\alpha,\beta=-\infty}^{\infty} = g\delta(\mathbf{r} - \alpha\mathbf{R}_1 - \beta\mathbf{R}_2) \tag{2.19}$$

Here, g indicates the strength of the perturbation. This model serves only to enforce the translational symmetry of the problem with no description of the shape of the potential.

Next, we evaluate $U(\mathbf{k})$.

$$U(\mathbf{k}) = \frac{1}{2\pi}\int_{-\infty}^{\infty}\int_{-\infty}^{\infty} U(\mathbf{r})e^{-i\mathbf{k}\cdot\mathbf{r}}dxdy = \frac{g}{2\pi}\sum_{\alpha,\beta=\infty}^{\infty}\int_{-\infty}^{\infty}\int_{-\infty}^{\infty}\delta(\mathbf{r}-\alpha\mathbf{R}_1-\beta\mathbf{R}_2)e^{-i\mathbf{k}\cdot\mathbf{r}}dxdy$$

Here, we can express $\mathbf{R}_1$ and $\mathbf{R}_2$ in terms of the lattice constant a.

$$\begin{aligned}
\mathbf{r}-\alpha\mathbf{R}_1-\beta\mathbf{R}_2 &= \left(x-\alpha\frac{3}{2}(n_1+m_1)a-\beta\frac{3}{2}(n_2+m_2)a\right)\hat{x} \\
&+ \left(y-\alpha\frac{\sqrt{3}}{2}(n_1-m_1)a-\beta\frac{\sqrt{3}}{2}(n_2-m_2)a\right)\hat{y} \\
&= (x-\alpha x_1-\beta x_2)\,\hat{x}+(y-\alpha y_1-\beta y_2)\,\hat{y} \qquad (2.20)
\end{aligned}$$

where $x_1 \equiv \frac{3}{2}(n_1+m_1)a$, $x_2 \equiv \frac{3}{2}(n_2+m_2)a$, $y_1 \equiv \frac{\sqrt{3}}{2}(n_1-m_1)a$, and $y_2 \equiv \frac{\sqrt{3}}{2}(n_2-m_2)a$. Therefore,

$$\delta(\mathbf{r}-\alpha\mathbf{R}_1-\beta\mathbf{R}_2) = \delta(x-\alpha x_1-\beta x_2)\delta(y-\alpha y_1-\beta y_2) \qquad (2.21)$$

Then,

$$\begin{aligned}
U(\mathbf{k}) &= \frac{g}{2\pi}\sum_{\alpha,\beta=-\infty}^{\infty}\left(\int_{-\infty}^{\infty}\delta(x-\alpha x_1-\beta x_2)e^{-ik_x x}dx\right)\left(\int_{-\infty}^{\infty}\delta(y-\alpha y_1-\beta y_2)e^{ik_y y}dy\right) \\
&= \frac{g}{2\pi}\sum_{\alpha,\beta=-\infty}^{\infty} e^{-ik_x(\alpha x_1+\beta x_2)}e^{-ik_y(\alpha y_1+\beta y_2)} \\
&= \frac{g}{2\pi}\left(\sum_{\alpha=-\infty}^{\infty} e^{i\alpha(k_x x_1+k_y y_1)}\right)\left(\sum_{\beta=-\infty}^{\infty} e^{i\beta(k_x x_2+k_y y_2)}\right) \\
&= \frac{g}{2\pi}\left(2\pi\sum_{\alpha=-\infty}^{\infty}\delta(k_x x_1+k_y y_1-2\pi\alpha)\right)\left(2\pi\sum_{\beta=-\infty}^{\infty}\delta(k_x x_2+k_y y_2-2\pi\beta)\right) \\
&= 2\pi g\sum_{\alpha,\beta=-\infty}^{\infty}\delta(k_x x_1+k_y y_1-2\pi\alpha)\delta(k_x x_2+k_y y_2-2\pi\beta) \qquad (2.22)
\end{aligned}$$

In order for $U(\mathbf{k}) \neq 0$, $\mathbf{k}$-points must satisfy the following equations:

$$\begin{aligned}
k_x x_1+k_y y_1 &= 2\pi\alpha \\
k_x x_2+k_y y_2 &= 2\pi\beta \qquad (2.23)
\end{aligned}$$

Equation 2.23 defines a grid of perturbed $\mathbf{k}$-points at which $U(\mathbf{k}) \neq 0$, as plotted in Figure 2.2 in the dissertation. When these points include the Dirac points $\mathbf{K}$ and $\mathbf{K}'$, we expect band gap opening. The Dirac points in the Brillouin zone are

$$\mathbf{K} = \left(\frac{2\pi}{3a}, \pm \frac{2\pi}{3\sqrt{3}a} \right). \tag{2.24}$$

We insert these into Equation 2.23.

$$\frac{2\pi}{3a}x_1 \pm \frac{2\pi}{3\sqrt{3}a}y_1 = 2\pi\alpha \quad ; \quad \frac{2\pi}{3a}x_2 \pm \frac{2\pi}{3\sqrt{3}a}y_2 = 2\pi\beta \tag{2.25}$$

Plugging in the expressions for x_1, y_1, x_2, and y_2,

$$\begin{aligned} \frac{2\pi}{3a}\left(\frac{3}{2}(n_1+m_1)a\right) \pm \frac{2\pi}{3\sqrt{3}a}\left(\frac{\sqrt{3}}{2}(n_1-m_1)a\right) &= 2\pi\alpha \\ \frac{2\pi}{3a}\left(\frac{3}{2}(n_2+m_2)a\right) \pm \frac{2\pi}{3\sqrt{3}a}\left(\frac{\sqrt{3}}{2}(n_2-m_2)a\right) &= 2\pi\beta, \end{aligned} \tag{2.26}$$

which reduce to

$$\begin{aligned} (n_1+m_1) \pm \frac{1}{3}(n_1-m_1) &= 2\alpha \\ (n_2+m_2) \pm \frac{1}{3}(n_2-m_2) &= 2\beta \end{aligned} \tag{2.27}$$

Equation 2.27 is satisfied for some integers α and β only if

$$n_1 - m_1 = 3p \quad \text{and} \quad n_2 - m_2 = 3q, \tag{2.28}$$

where p and q are integers. If $n_1 - m_1 = 3p$,

$$\begin{aligned} n_1 + m_1 &= 3p + 2m_1 \\ \Rightarrow 3p + 2m_1 \pm \frac{1}{3}3p &= 2\alpha \\ 3p + 2m_1 \pm p &= 2\alpha \\ 4p + 2m_1 = 2\alpha \quad &\text{or} \quad 2p + 2m_1 = 2\alpha \end{aligned} \tag{2.29}$$

Since both the LHS and RHS of Equation 2.29 are always even numbers and we are free to choose α, the condition in Equation 2.27 is indeed satistfied if $n_1 - m_1 = 3p$ and $n_2 - m_2 = 3q$.

This is the crucial band gap opening rule in the paper.

2.6.4 Brillouin zones

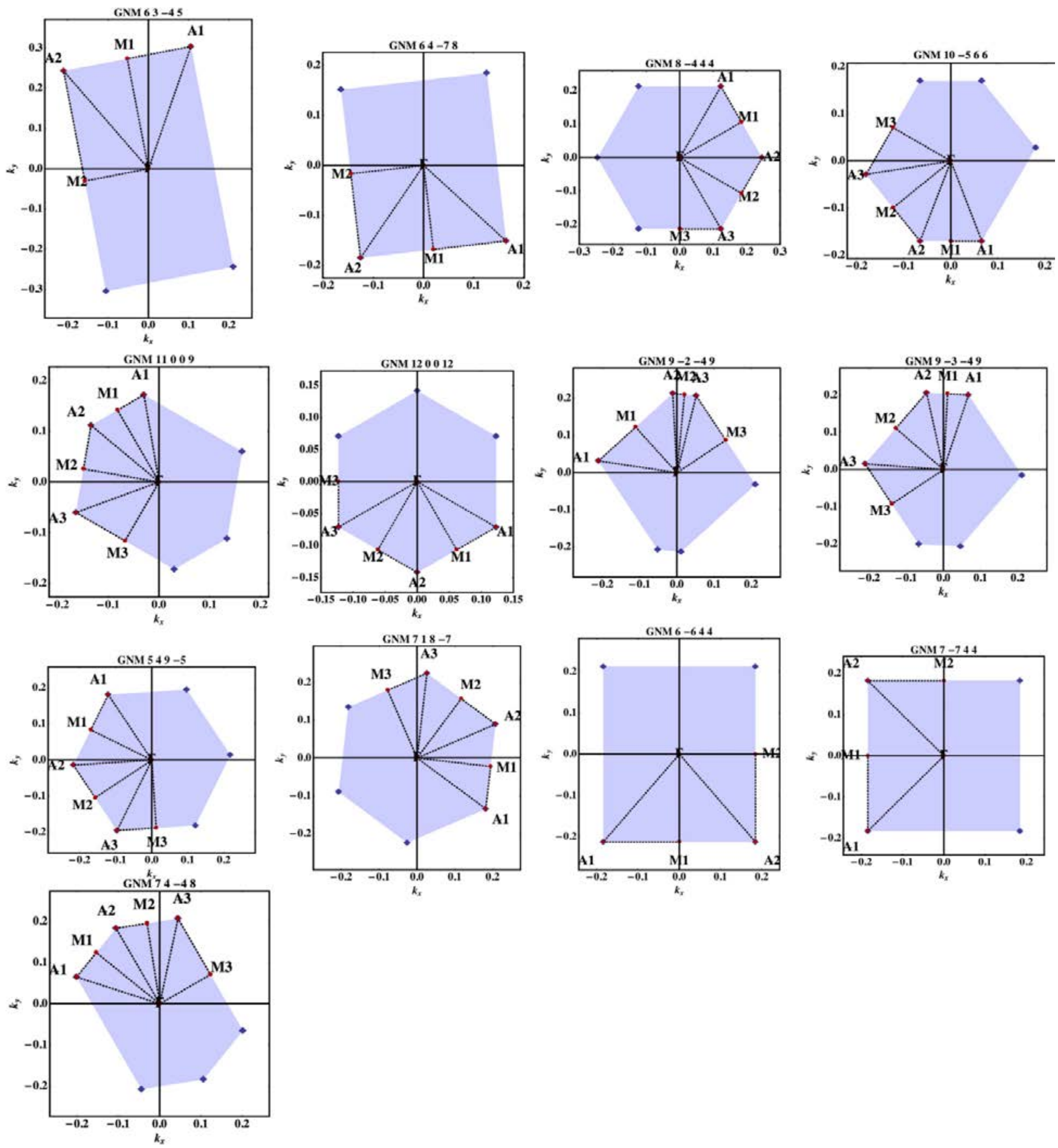

Figure 2.5: Brillouin zones for GNMs. Left to right, top to to bottom, the (n_1, m_1, n_2, m_2) coordinates for the GNM structures presented in the paper are $(6, 3, -4, 5)$, $(6, 4, -7, 8)$, $(8, -4, 4, 4)$, $(10, -5, 6, 6)$, $(5, 4, 9, -5)$, $(11, 0, 0, 9)$, $(12, 0, 0, 12)$, $9, -2, -4, 9)$, $(9, -3, -4, 9)$, $(7, 1, 8, -7)$, $(6, -6, 4, 4)$, $(7, -7, 4, 4)$, and $(7, 4, -4, 8)$.

2.6.5 Zigzag, armchair, and zigzag-armchair GNMs

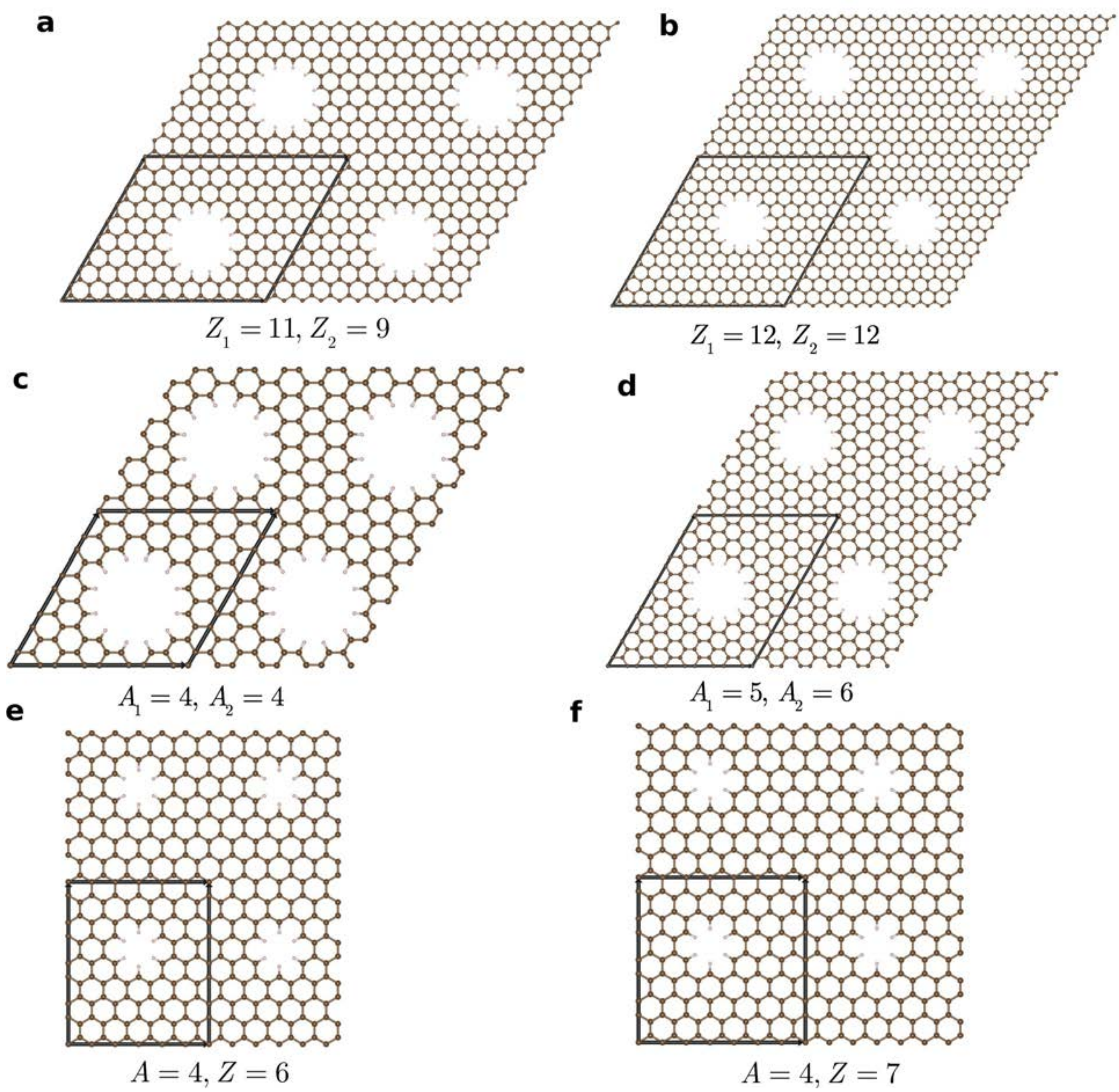

Figure 2.6: Crystal structures of two zigzag (**a**, **b**), armchair (**c**, **d**), and zigzag-armchair (**e**, **f**) GNMs, whose electronic band structures are plotted in Figure 4 in the paper.

2.6.6 Summary of band gap results

Table 2.1: Summary of band gap results. Hole size refers to the number of C atoms removed from graphene. Y or N indicates whether the structure satisfies the geometric condition for band gap opening.

	n_1	m_1	n_2	m_2	Hole Size	TB Gap?	DFT Gap (eV)
AZ Rectangular	10	-10	4	4	24	N	0
	9	-9	7	7	24	N	0.41
	10	-10	7	7	24	N	0
	6	-6	6	6	24	Y	0.70
	11	-11	8	8	24	N	0
	12	-12	8	8	24	Y	0.27
Chiral Rectangular	3	2	-7	8	6	N	0
	4	1	-6	9	6	Y	0.62
	4	3	-10	11	6	N	0
	5	1	-7	11	6	N	0
	6	3	-4	5	6	Y	0.61
	6	4	-7	8	6	N	0
	7	2	-11	16	6	N	0
	8	2	-6	9	6	Y	0.35
	9	6	-7	8	6	Y	0.26
Zigzag	10	0	0	10	24	N	0
	11	0	0	12	24	N	0
	12	0	0	12	6	Y	0.21
	12	0	0	12	24	Y	0.38
	12	0	0	12	54	Y	0.50
Armchair	8	-4	6	6	24	Y	1.05
	8	-4	5	5	24	Y	0.78
	10	-5	5	5	24	Y	0.68
	10	-5	6	6	24	Y	0.55
	14	-7	8	8	6	Y	0.18
	14	-7	8	8	24	Y	0.32
	14	-7	8	8	54	Y	0.41
	14	-7	8	8	96	Y	0.41
60° Parallelogram	3	5	8	-3	24	N	0
	5	4	9	-5	24	N	0
	7	1	8	-7	24	Y	0.98
Oblique Parallelogram	9	-1	-4	9	6	N	0
	9	-2	-4	9	6	N	0
	9	-3	-4	9	6	N	< 0.05

	n_1	m_1	n_2	m_2	Hole Size	TB Gap?	DFT Gap (eV)
	9	-1	-4	9	24	N	0
	9	-2	-4	9	24	N	0
	9	-3	-4	9	24	N	< 0.1
	10	1	2	9	24	N	9
	10	2	2	9	24	N	0
	7	4	-4	8	24	Y	0.62

2.6.7 Dependence of band gap in GNMs on hole size

Our derivation is general enough that it likely holds for several different perturbative potentials that are reasonably localized. We have studied a series of holes in graphene nanomeshes (GNMs), and our results suggest that as hole size is increased, the band gap in semiconducting GNMs increases. If a band gap exists, the magnitude of E_g is primarily determined by the hole size and the supercell area. We used the following scaling rules proposed by Pedersen *et al.*[12],

$$E_\mathrm{g} = g\frac{N^{\alpha}_{\mathrm{removed}}}{N_{\mathrm{total}}}, \tag{2.30}$$

to fit our band gap data. Originally the parameter α is set to 0.5, but we found that $\alpha \sim 0.3$ gave the best fit to our GNM data, as plotted in Figure 2.4i in this dissertation and Figure 4b in Oswald *et al.*'s work [10], respectively.

CHAPTER 3

GEOMETRICALLY INDUCED TRANSITIONS BETWEEN SEMIMETAL AND SEMICONDUCTOR IN GRAPHENE

Adapted from an article published as

Physical Review B **90**, 115415 (2014).

Marc Dvorak [4,5], and Zhigang Wu[4,5]

How the long-range order and local defect configurations modify the electronic structure of graphene remains an outstanding problem in nanoscience, which precludes the practical method of patterning graphene from being widely adopted for making graphene-based electronic and optoelectronic devices. A small variation in supercell geometry can change the patterned graphene from a semimetal to a semiconductor, or vice versa. Based on the effective-Hamiltonian formalism, here we reveal that a semimetal-to-semiconductor transition can be induced geometrically without breaking sublattice symmetry. For the same patterning periodicity, however, breaking sublattice symmetry increases the gap, while phase cancellation can lead to a semiconductor-to-semimetal transition in non-Bravais lattices. Our theory predicts the analytic relationship between long-range defect order and band gap opening/closure in graphene, which is in excellent agreement with our numerical *ab-initio* calculations of graphene nanomeshes, partially hydrogen passivated graphene, and boron nitride doped graphene.

3.1 Introduction

While graphene [45, 89] possesses exceptional charge carrier mobilities [68], it lacks a sizable band gap necessary for meaningful on-off ratios in field-effect transistors or for practical

[4]Department of Physics, Colorado School of Mines
[5]Researcher and Author

optoelectronics. The pursuit of semiconducting graphene-based materials remains a high priority in current research. Recently, field-effect transistors based on graphene nanomeshes (GNMs), in which periodic holes are punctuated, have been fabricated [6]. Similarly, band gap opening in graphene has also been induced by patterned hydrogen (H) adsorption [74] or boron nitride (BN) doping [25, 26, 90]. An alternative scheme is 'self-doping', where extended defects, such as pentagons and heptagons, are introduced to alter the properties of graphene [20].

An outstanding problem is how such periodic patternings modify the electronic structure of graphene. In particular, what are the exact effects of the long-range order and local defects on the Dirac points ($\mathbf{K}$ and $\mathbf{K}'$) where π and π^* bands touch? Previous experimental [6, 26, 74, 91, 92] and theoretical [10, 15, 16, 18, 82, 93–100] studies have revealed that the electronic band structure of graphene is sensitive to patterning: a small variation in the supercell periodicity could change the patterned graphene from a semimetal to a semiconductor, or vice versa. However, the underlying mechanisms and basic rules remain unclear, since most of these theoretical efforts relied heavily on first-principles computations of special cases, lacking analytic understanding from fundamental considerations.

Here, we propose a theory based on the effective Hamiltonian for the tight-binding model of graphene to reveal the analytic relation between defect geometry and band gap opening/closure. We show that without breaking sublattice symmetry, the semimetal-to-semiconductor transition can occur if the periodic defects induce scattering between two Dirac points, while such scattering can be annihilated by phase cancellation if defects form non-Bravais lattices in certain arrangements. In addition, breaking sublattice symmetry always increases band gaps, and such symmetry breaking and restoring can also be induced geometrically. We carry out first-principles electronic structure calculations for three different types of patterned graphene, including GNMs, partially H-passivated graphene, and hexagonal BN-doped graphene. The numerical results confirm our analytic theory and also find the band gap scaling rules in these defected graphene structures.

3.2 Theoretical Results

Two carbon (C) atoms in the unit cell of graphene form two sublattices, and the famous electronic band structure of graphene is well described by the two-dimensional tight-binding model Hamiltonian [45, 101] including only nearest-neighbor hopping:

$$H_0(\mathbf{k}) = \begin{pmatrix} E_0 & tf(\mathbf{k}) \\ tf^*(\mathbf{k}) & E_0 \end{pmatrix}. \tag{3.1}$$

Here E_0 and t are the on-site energy and hopping parameter, respectively, and

$$f(\mathbf{k}) = e^{ik_x a} + 2e^{-ik_x a/2} \cos\left(\frac{\sqrt{3}}{2} k_y a\right), \tag{3.2}$$

with a the C-C distance. The eigenvalues for this effective Hamiltonian are $E = E_0 + st|f(\mathbf{k})|$, where $s = \pm 1$, and the eigenstates are

$$\langle \mathbf{r}|s, \mathbf{k}\rangle = \frac{1}{\sqrt{2}} e^{i\mathbf{k}\cdot\mathbf{r}} \begin{pmatrix} 1 \\ se^{i\theta(\mathbf{k})} \end{pmatrix}, \tag{3.3}$$

where $e^{i\theta(\mathbf{k})} = f(\mathbf{k})/|f(\mathbf{k})|$.

All types of periodic patterning mentioned above can be universally modeled by applying a periodic external potential $U(\mathbf{r}) = U(\mathbf{r}+\mathbf{R}_i)$, with $\mathbf{R}_i$ ($i = 1, 2$) the supercell lattice vectors for the patterned graphene. The scattering amplitude between two states is [78, 87, 88, 102]

$$\langle s, \mathbf{k}|U(\mathbf{r})|s', \mathbf{k}'\rangle = \sum_{\mathbf{G}} \frac{1}{2}(1 + ss' e^{i[\theta(\mathbf{k}')-\theta(\mathbf{k})]}) U(\mathbf{G}) \delta_{\mathbf{k}',\mathbf{k}-\mathbf{G}}, \tag{3.4}$$

where $\mathbf{G}$ and $U(\mathbf{G})$ are the reciprocal lattice vector and the Fourier component of the external periodic potential, respectively.

Equation 3.4 suggests that a semimetal to semiconductor transition can occur if the scattering between two degenerate states at Dirac points $\mathbf{K}$ and $\mathbf{K}'$ is non-zero, i.e., when $U(\mathbf{G}) \neq 0$ at $\mathbf{G} = \mathbf{K} - \mathbf{K}'$. Because of the periodicity in reciprocal space of graphene, the above condition is equivalent to $U(\mathbf{K}) \neq 0$ (and $U(\mathbf{K}') \neq 0$), which induces band gap opening without breaking sublattice symmetry. Considering the usual case in which the defected sites are only a small portion of all C atoms, we propose a simple periodic model potential based on the Dirac δ-function,

$$U(\mathbf{r}) = \sum_{\alpha,\beta=-\infty}^{\alpha,\beta=+\infty} g\delta(\mathbf{r} - \alpha\mathbf{R}_1 - \beta\mathbf{R}_2), \tag{3.5}$$

with integers α and β. $U(\mathbf{K}) \neq 0$ only when the reciprocal lattice vectors $\mathbf{G}$ for the periodically modified graphene, with lattice vectors $\mathbf{R}_1 = n_1\mathbf{a}_1 + m_1\mathbf{a}_2$ and $\mathbf{R}_2 = n_2\mathbf{a}_1 + m_2\mathbf{a}_2$, contain the Dirac points of pristine graphene. Here, $\mathbf{a}_1$ and $\mathbf{a}_2$ are primitive lattice vectors of graphene, and (n_1, m_1, n_2, m_2) are four integers. It is straightforward to show [103] that $U(\mathbf{K}) \neq 0$ is satisfied only when

$$n_1 - m_1 = 3p, \text{ and } n_2 - m_2 = 3q, \tag{3.6}$$

for integers p and q, which is the same condition for a *semimetallic* carbon nanotube with chirality index $(n_1,\ m_1)$ or $(n_2,\ m_2)$ at the tight-binding level of theory.

Therefore there are two approaches to open up a band gap in graphene by applying periodic defects. The first one is sublattice symmetry breaking, e.g., BN doping, so that the two diagonal matrix elements in the effective Hamiltonian (Equation 3.1) are different and the degeneracy at the Dirac points is lifted. This has been extensively studied. The second is the intervalley scattering between two Dirac points $\mathbf{K}$ and $\mathbf{K}'$ induced geometrically without breaking sublattice symmetry, which can be realized with GNMs and partial H passivation. The second mechanism remains under exploration. Here, our theory has derived the analytic relationship between the translational symmetry of the material and the transition between semimetal and semiconductor.

Next, we extend our theory to graphene sheets whose defects form non-Bravais lattices, e.g., a honeycomb structure. If there are more than one ($M > 1$) defects in a supercell centered at $\boldsymbol{\tau}_1$, $\boldsymbol{\tau}_2$, ..., $\boldsymbol{\tau}_M$, it can be shown that

$$U^{\mathrm{non-Brav}}(\mathbf{k}) = S(\mathbf{k})U^{\mathrm{Brav}}(\mathbf{k}), \tag{3.7}$$

where $U^{\mathrm{non-Brav}}(\mathbf{k})$ is the external potential for the non-Bravais lattice, $U^{\mathrm{Brav}}(\mathbf{k})$ for the corresponding Bravais lattice, and the defect structure factor $S(\mathbf{k}) = \sum_{j=1}^{M} \exp(i\mathbf{k} \cdot \boldsymbol{\tau}_j)$. Even if the lattice vectors of a non-Bravais structure satisfy the band gap opening condition

(Equation 3.6), a zero structure factor at the Dirac point,

$$0 = S(\mathbf{K}) = \sum_{j=1}^{M} \exp(i\mathbf{K} \cdot \boldsymbol{\tau}_j), \tag{3.8}$$

leads to band gap closure due to phase cancellation.

3.3 *Ab-initio* Simulation Results

We employ first-principles electronic structure calculations based on density functional theory (DFT) to verify our analytic theory. Although DFT often severely underestimates band gaps, it accurately predicts a zero gap at the Dirac points for graphene and yields qualitatively correct electronic band structures for graphene [104] and graphene nanoribbons [105, 106]. Our spin-polarized calculations within the generalized gradient approximation [86] are carried out using the SIESTA code [84] based on atomic orbitals. Specifically, we use a triple-ζ polarized basis set for C and double-ζ polarized basis sets for B, N, and H, whose accuracy and convergence have been well examined by comparing against calculations using the planewave VASP code [85]. All graphene structures in this work are relaxed until all atomic forces are less than 0.02 eV/Å and the maximum stress is below 0.2 GPa.

3.3.1 Defects forming Bravais structures

Figure 3.1 shows the crystal and electronic band structures for two different supercells with partial H-passivation, holes (GNMs), and BN doping regions forming Bravais lattices. The effect of supercell lattice symmetry on electronic properties is compared across the three rows of panels, while the effect of different types of defects is compared among each column. The supercells on the left column have $(n_1, m_1, n_2, m_2) = (6, -6, 4, 4)$ so that $n_1 - m_1$ and $n_2 - m_2$ are both divisible by 3, satisfying the condition of Equation 3.6. The supercells on the right column have $(n_1, m_1, n_2, m_2) = (7, -7, 4, 4)$, therefore $n_1 - m_1 = 14$, not divisible by 3. Our theory predicts that the partially H-passivated graphene and GNM shown in the left column of Figure 3.1 are semiconductors, while those on the right (Figure 3.1b and d) are semimetals, consistent with first-principles results. Our theory also indicates that the

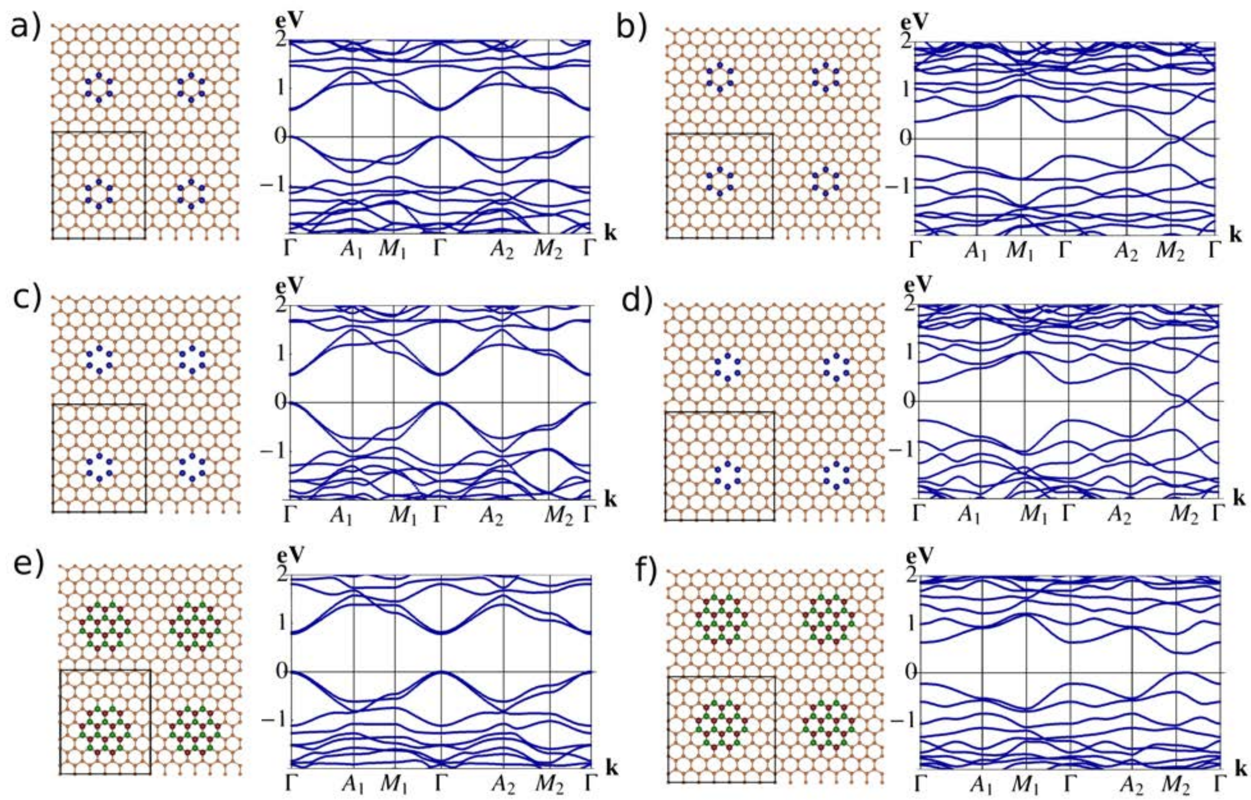

Figure 3.1: Crystal (left) and electronic band (right) structures for (a) H-passivated graphene, (c) GNM and (e) BN-doped graphene with supercell lattice parameters $(n_1, m_1, n_2, m_2) = (6, -6, 4, 4)$. Panels (b), (d) and (f) show those corresponding structures with $(n_1, m_1, n_2, m_2) = (7, -7, 4, 4)$. Here C, H, B and N atoms are denoted by golden, blue, green and red spheres, respectively. The black rectangle in each panel indicates the supercell of defected graphene.

BN-doped graphene is always semiconducting due to broken sublattice symmetry, but the long-range order could increase E_{g} if the lattice parameters (n_1, m_1, n_2, m_2) satisfy Equation 3.6. This prediction agrees well with the calculated electronic band structures shown in Figure 3.1e and f, with $E_{\mathrm{g}} = 0.78$ and 0.39 eV, respectively.

In addition, as expected, electronic band structures in the left three panels are very similar, differing mainly in values of their band gap, with 0.55, 0.56 and 0.78 eV for the partially-H passivated graphene, GNM, and BN-doped graphene materials shown in Figure 3.1a, c, and e, respectively. Electronic band structures across the right column are also very similar, except that in Figure 3.1f for the BN-doped graphene there is an energy gap at a point between Γ and M_2, at which the band gap closes in Figure 3.1b and d for H-passivated graphene and the GNM. These three types of defected graphene structures with other shapes of supercells, such as hexagonal or parallelogram, show the same trends for electronic band structures.

Table 3.1: Calculated band gaps (E_g in eV) of graphene sheets partially passivated by H. Here N_d and N_{tot} are the numbers of defected (passivated by H) and total carbon atoms in one supercell, respectively.

Cell type	n_1	m_1	n_2	m_2	E_g	N_d	N_{tot}	Defect %
Armchair	10	−5	5	5	0.48	12	150	8.0
	14	−7	8	8	0.14	6	336	1.8
	8	−4	5	5	0.59	12	120	10.0
Zigzag	6	0	0	6	0.71	6	72	8.3
	6	0	0	6	1.05	12	72	16.7
	6	0	0	7	0.00	12	84	14.3
	7	0	0	7	0.00	12	98	12.2
Chiral hexagonal	3	5	8	3	0.00	6	62	9.7
	5	4	9	−5	0.00	6	122	4.9
	7	1	8	−7	0.49	6	114	5.3
Chiral rectangular	6	2	−7	5	0.00	12	88	13.6
	6	3	−4	5	0.63	6	84	7.1
	6	4	−7	8	0.00	6	152	3.9
Rectangular	5	−5	5	5	0.00	6	100	6.0
	6	−6	4	4	0.55	6	96	6.3
	7	−7	4	4	0.00	6	112	5.4
Parallelogram	6	1	−3	9	0.00	6	114	5.3
	6	2	−3	9	0.00	6	120	5.0
	6	3	−2	7	0.54	6	96	6.3

Table 3.1 and Table 3.2 summarize the calculated E_g for H-passivated and BN-doped graphene sheets with various supercell symmetries, in addition to the rectangular unit cells shown in Figure 3.1. Results for GNM structures (not shown) are very similar to those for H-passivated graphene, as demonstrated in Figure 3.1a–d and in Figure 3.2a. Here, armchair indicates that both supercell vectors are along the armchair direction so that $(n_1, m_1, n_2, m_2) = (2n, -n, m, m)$ with n and m two integers, while zigzag indicates that both supercell vectors are along the zigzag direction so that $(n_1, m_1, n_2, m_2) = (n, 0, 0, m)$. Rectan-

Table 3.2: Calculated band gaps (E_g in eV) of graphene sheets doped by BN. Here N_d is the number of defected (replaced by B or N) carbon atoms while N_tot indicates the total number of atoms (including C, B and N) in one supercell.

Cell type	n_1	m_1	n_2	m_2	E_g	N_d	N_tot	Defect %
Armchair	10	−5	5	5	0.34	12	150	8.0
	14	−7	8	8	0.08	6	336	1.8
	8	−4	5	5	0.42	12	120	10.0
Zigzag	6	0	0	6	0.69	12	72	16.7
	6	0	0	7	0.41	12	84	14.3
	7	0	0	7	0.36	12	98	12.2
Chiral hexagonal	3	5	8	−3	0.16	6	98	6.1
	3	5	8	−3	0.48	12	98	12.2
	5	4	9	−5	0.13	6	122	4.9
	5	4	9	−5	0.38	12	122	9.8
	7	1	8	−7	0.25	6	114	5.3
	7	1	8	−7	0.68	12	114	10.5
Chiral rectangular	6	2	−7	5	0.42	12	104	11.5
	6	3	−4	5	0.33	6	84	7.1
	6	4	−7	8	0.31	12	152	7.9
Rectangular	5	−5	5	5	0.53	12	100	12.0
	6	−6	4	4	0.78	12	96	12.5
	7	−7	4	4	0.39	12	112	10.7
Parallelogram	6	1	−3	9	0.42	12	114	10.5
	6	2	−3	9	0.39	12	120	10.0
	6	3	−2	7	0.75	12	96	12.5

gular corresponds to rectangular supercells with one lattice vector along the zigzag direction while the other vector is along the armchair direction with $(n_1, m_1, n_2, m_2) = (n, -n, m, m)$, while chiral rectangular and chiral hexagonal correspond to rectangular and hexagonal supercells with lattice vectors along arbitrary directions. These numerical results in Table 3.1 and Table 3.2 verify our analytic model on the semimetal-to-semiconductor transition in periodically defected graphene.

Quantitatively, E_g in these semiconducting graphene structures is roughly proportional to the defect percentage (x, roughly when $x < 15\%$): $E_\mathrm{g} \approx Cx$ with C a constant, as demonstrated in Figure 3.2. Here Figure 3.2a shows that E_g in a semiconducting GNM is slightly larger than that in a corresponding H-passivated graphene with the same supercell and defected area. However, Figure 3.2b indicates that in BN-doped graphene, for the same level of doping, E_{g} is considerably enhanced if its lattice parameters (n_1, m_1, n_2, m_2) satisfy Equation 3.6. Linear fitting to Figure 3.2a obtains $C = 0.091\,\mathrm{eV}/\%$ and $0.087\,\mathrm{eV}/\%$ for GNM and H-passivated graphene, respectively, and $C = 0.057\,\mathrm{eV}/\%$ (the red line) and $0.036\,\mathrm{eV}/\%$ (the green line) in Figure 3.2b for BN-doped graphene. These values suggest that in BN-doped graphene, the imbalance between two sublattices contributes more to E_{g} than the supercell symmetry does, and the effect on E_{g} from the latter is much weaker than

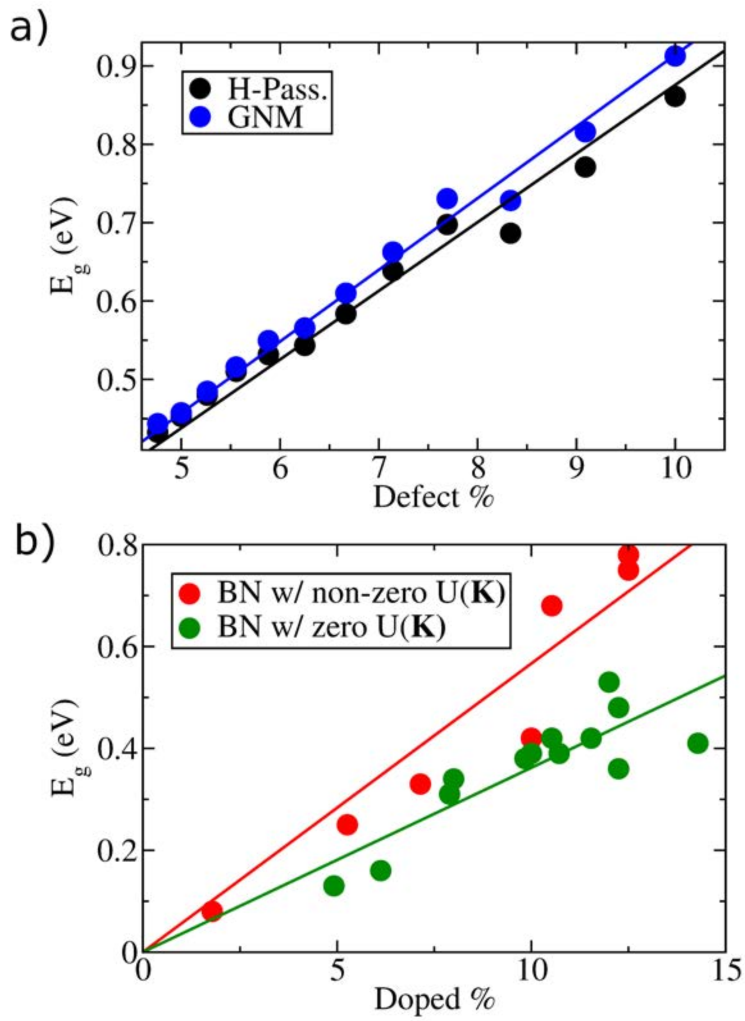

Figure 3.2: Band gap (E_{g}) as a function of defect percentage for (a) partially H-passivated graphene and GNMs and (b) BN-doped graphene.

that in GNMs or H-passivated graphene. Removing or passivating p_z orbitals of C atoms is apparently a stronger perturbation than BN substitution.

3.3.2 Defects forming non-Bravais structures

Next, we consider defects forming non-Bravais structures. As illustrated in Figure 3.3, the H-passivated graphene sheets in the upper two panels share the same chiral hexagonal lattice with parameters $(n_1, m_1, n_2, m_2) = (7, 1, 8, -7)$. Their electronic band structures are similar, except that E_g for the non-Bravais structure is larger. Since $n_1 - m_1$ and $n_2 - m_2$ are both divisible by 3, the Bravais structure (Figure 3.3a) is semiconducting with $E_\mathrm{g} = 0.50$ eV, while the non-Bravais structure (Figure 3.3b) with two passivated areas has a larger gap of 0.84 eV. This is because $\boldsymbol{\tau}_2 - \boldsymbol{\tau}_1 = 2\mathbf{a}_1 + 2\mathbf{a}_2$, and $S(\mathbf{K}) = e^{i\mathbf{K}\cdot\boldsymbol{\tau}_1}[1 + e^{i\mathbf{K}\cdot(\boldsymbol{\tau}_2-\boldsymbol{\tau}_1)}] = e^{i\mathbf{K}\cdot\boldsymbol{\tau}_1}(1 + e^{i4\pi})$, leading to $|S(\mathbf{K})| = 2 > 1$; consequently, constructive interference enlarges the band gap.

One cannot create a non-Bravais graphene lattice with two defects per unit cell whose structure factor vanishes at the Dirac point. This is because for an arbitrary relative displacement $\boldsymbol{\tau}_2 - \boldsymbol{\tau}_1 = p\mathbf{a}_1 + q\mathbf{a}_2$ with p and q two integers, $\mathbf{K}\cdot(\boldsymbol{\tau}_2 - \boldsymbol{\tau}_1) = 2q\pi + \frac{4}{3}(p-q)\pi \neq (2n+1)\pi$ with n an integer, thus $S(\boldsymbol{K}) = 1 + e^{i\mathbf{K}\cdot(\boldsymbol{\tau}_2-\boldsymbol{\tau}_1)} \neq 0$. However, it is possible when there are more than two identical defects per unit cell, e.g., the triangular arrangement shown in Figure 3.3d. In this H-passivated graphene material, defects are displaced along zigzag directions in a supercell by vectors of $\boldsymbol{\tau}_2 - \boldsymbol{\tau}_1 = 5\mathbf{a}_1$ and $\boldsymbol{\tau}_3 - \boldsymbol{\tau}_1 = 5\mathbf{a}_2$, so that $1 + e^{i\mathbf{K}\cdot(\boldsymbol{\tau}_2-\boldsymbol{\tau}_1)} + e^{i\mathbf{K}\cdot(\boldsymbol{\tau}_3-\boldsymbol{\tau}_1)} = 0$. Even though the corresponding Bravais structure (not shown) is semiconducting with $E_\mathrm{g} = 0.34$ eV, this non-Bravais structure is a semimetal. In contrast, the non-Bravais structure plotted in Figure 3.3c, in which three defects in a supercell are displaced along armchair directions, specifically, $\boldsymbol{\tau}_2 - \boldsymbol{\tau}_1 = 2\mathbf{a}_1 + 2\mathbf{a}_2$ and $\boldsymbol{\tau}_3 - \boldsymbol{\tau}_1 = 2\mathbf{a}_1 - 2\mathbf{a}_2$, leads to $|S(\mathbf{K})| = \sqrt{3}$ and an enlarged band gap of 0.83 eV.

Figure 3.3e suggests that constructive interference with $|S(\mathbf{K})| = \sqrt{3}$ in the GNM leads to an enhanced $E_\mathrm{g} = 0.91$ eV, compared with $E_\mathrm{g} = 0.36$ eV for the corresponding Bravais GNM, whereas a destructive interference with $S(\mathbf{K}) = 0$ in the non-Bravais GNM plotted in Figure 3.3f leads to zero gap. Our calculations have demonstrated a transition from semi-

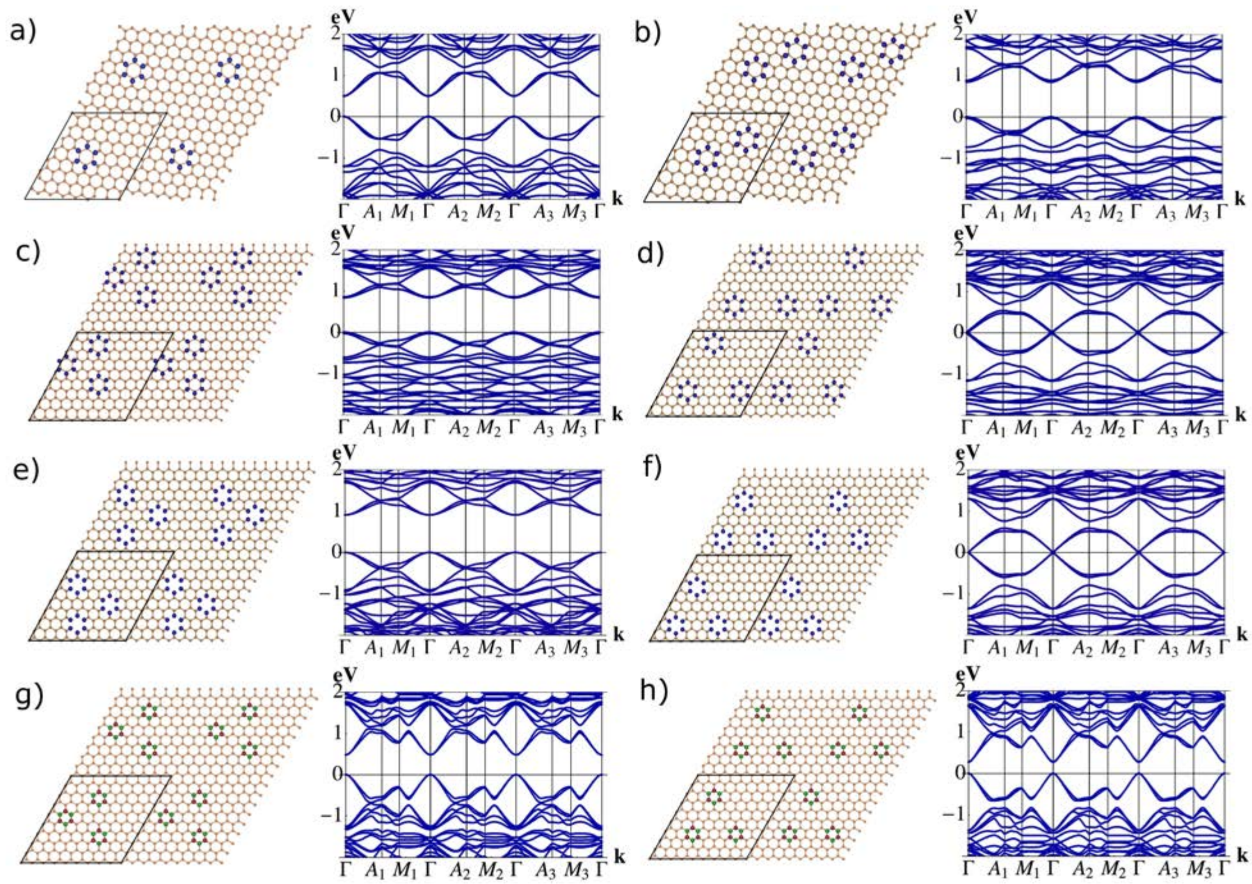

Figure 3.3: Crystal (left) and electronic band (right) structures of defected graphene sheets, which have $(7, 1, 8, -7)$ supercells in (a) and (b) and $(9, 0, 0, 9)$ supercells in (c–h). Except for panel (a), defects in these graphene structures form non-Bravais lattices. (a–d) H-passivated graphene. (e) and (f) GNMs. (g) and (h) BN-doped graphene. Supercells in these graphene structures are indicated by black parallelograms.

conductor to semimetal by rearranging the defects in H-passivated graphene and GNMs, as predicted in Equation 3.8. The cancellation of phase factors is compelling evidence that intervalley scattering is the mechanism responsible for band gap opening in defected graphene.

Finally, we discuss non-Bravais lattices with BN-doped areas. Figure 3.3g indicates that constructive interference with $|S(\mathbf{K})| = \sqrt{3}$ drastically increases the band gap ($E_\mathrm{g} = 0.48$ eV), compared with that of only 0.17 eV in the corresponding Bravais structure. However, destructive interference with zero $S(\mathbf{K})$ does not lead to no gap at the Γ-point (Figure 3.3h), although its band gap is reduced to 0.27 eV. This is due to the imbalance between A- and B-sublattices, so that $E_\mathrm{g} \neq 0$. Compared with the corresponding Bravais structure, the

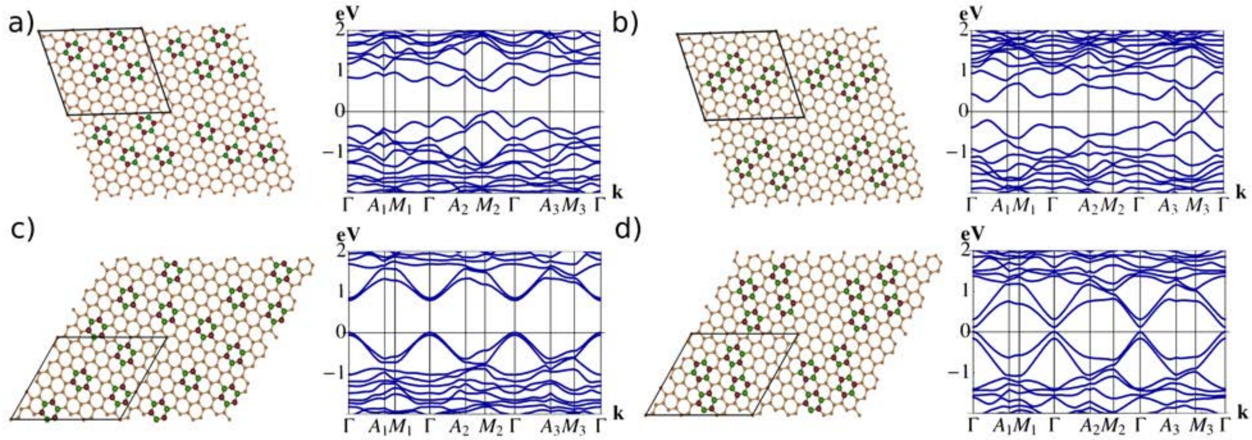

Figure 3.4: Crystal (left) and electronic band (right) structures of BN-doped graphene with supercell lattice parameters of $(6, 1, -3, 9)$ in (a) and (b) and $(6, 3, -2, 7)$ in (c) and (d). In the left column ((a) and (c)) four doped areas in a supercell are identical, while in the right column ((b) and (d)) in a supercell two BN-doped areas are different from the other two so that an overall balance between A and B-sublattices is reached. In each panel, the supercell is indicated by a black outline.

non-Bravais BN-doped graphene with $S(\mathbf{K}) = 0$ (Figure 3.3g) has a larger gap, because of the larger imbalance between A- and B-sublattices.

To induce a transition from semiconductor to semimetal for BN-doped graphene, one can geometrically restore the sublattice balance by switching B and N atoms between doped regions. The top row of Figure 3.4 does not satisfy the condition for intervalley scattering. Figure 3.4b shows a $(6, 1, -3, 9)$ lattice with zero gap, compared with the structure plotted in Figure 3.4a, which has the same $(6, 1, -3, 9)$ lattice but is a semiconductor with $E_{\mathrm{g}} = 0.50$ eV. Figure 3.4c and d show the $(6, 3, -2, 7)$ lattice, which satisfy the band gap opening rule of Equation 3.6. In Figure 3.4c, $S(\mathbf{K}) \neq 0$, leading to a relatively large band gap of 0.80 eV, whereas in Figure 3.4d switching B and N atoms between defects to restore A- and B-sublattice balance significantly reduces E_{g} to merely 0.12 eV. Figure 3.4d isolates the band gap opened by BN doping only due to intervalley scattering caused by long-range order, not due to sublattice imbalance. Further arranging identical doping sites to ensure $S(\mathbf{K}) = 0$ can eventually induce the semiconductor-to-semimetal transition geometrically.

3.4 Summary

In summary, we find that the degeneracy at the Dirac points is lifted and a sizable band gap appears when the reciprocal lattice vectors of defected graphene overlap with Dirac points of pristine graphene. Previous work has shown the absence of back scattering and band gaps in graphene and metallic carbon nanotubes under external potentials that vary slowly on the order of the C-C bond length [87, 88, 102]. However, for dopants, adsorbed atoms, and vacancies, the corresponding effective potentials vary considerably on this length scale, leading to the existence of intervalley scattering between $\mathbf{K}$ and $\mathbf{K}'$.[87, 88, 102] The symmetry breaking between two sublattices is also a contributing factor to band gap, which has been studied before. Here, our theory includes both sublattice asymmetry and intervalley scattering. For multiple defects in a supercell forming a non-Bravais structure, the magnitude of the structure factor at the Dirac point determines the size of the band gap at the Dirac point. Thus, arranging defects in non-Bravais structures can cause a transition from semiconductor to semimetal if destructive interference leads to complete phase cancellation and the sublattice symmetry is kept.

Our *ab-initio* electronic structure calculations on a variety of partially H-passivated graphene structures, graphene nanomeshes, and BN-doped graphene demonstrate the validity of our analytic analysis. The sublattice symmetry in H-passivated graphene and GNMs in our study is maintained, therefore the supercell symmetry and structure factor at the Dirac points can be controlled geometrically to induce transitions between semimetal and semiconductor. On the other hand, the balance between two sublattices in BN-doped graphene sheets must be restored to induce such transitions, in addition to lattice symmetry considerations. Our present model offers the fundamental understanding of how local defect configurations and long-range order modify the electronic properties of complex and realistic graphene structures so that precise tuning for various applications is possible.

3.5 Acknowledgments

This work was supported by U.S. DOE Early Career Award (Grant No. DE-SC0006433). Computations were carried out at the Golden Energy Computing Organization at CSM and the National Energy Research Scientific Computing Center (NERSC). The authors thank M. Lusk and D. Wood for insightful discussions.

CHAPTER 4

DIRAC POINT MOVEMENT AND TOPOLOGICAL PHASE TRANSITION IN PATTERNED GRAPHENE

Reproduced by permission of The Royal Society of Chemistry.

Nanoscale **7**, 3645 (2015).

Marc Dvorak [6,7], and Zhigang Wu[6.7]

The honeycomb lattice of graphene is characterized by linear dispersion and pseudospin chirality of fermions on the Dirac cones. If lattice anisotropy is introduced, the Dirac cones stay intact but move in reciprocal space. Dirac point movement can lead to a topological transition from semimetal to semiconductor when two inequivalent Dirac points merge, an idea that has attracted significant research interest. However, such movement normally requires unrealistically high lattice anisotropy. Here, we show that anisotropic defects can break the C_3 symmetry of graphene, leading to Dirac point drift in the Brillouin zone. Additionally, the long-range order in periodically patterned graphene can induce intervalley scattering between two inequivalent Dirac points, resulting in a semimetal-to-insulator topological phase transition. The magnitude and direction of Dirac point drift are predicted analytically, which are consistent with our first-principles electronic structure calculations. Thus, periodically patterned graphene can be used to study the fascinating physics associated with Dirac point movement and the corresponding phase transition.

4.1 Introduction

Since the isolation of graphene, a two-dimensional (2D) honeycomb lattice of carbon (C) atoms, tremendous research efforts have been spent on the physics of the honeycomb lattice and Dirac points [45, 107, 108]. Dirac points manifest themselves in many intriguing

[6]Department of Physics, Colorado School of Mines
[7]Researcher and Author

phenomena, including massless fermions in graphene [45] and conducting surface states in topological insulators [109]. Dirac points can appear in any 2D lattice if parameters are appropriately adjusted, but the honeycomb lattice is the simplest and most natural realization. Graphene is a tangible, solid-state example of such a lattice with C_3 symmetry, but Dirac points also exist on honeycomb lattices without C_3 symmetry. One possible realization is strained graphene [110–112], but most experiments focus on anisotropy in honeycomb optical lattices [113–117], which can be precisely tuned to study massless Dirac fermions and their correlated phases.

In pristine graphene, the Dirac points ($\mathbf{D}$ and $\mathbf{D}' = -\mathbf{D}$) are located at the corners of the hexagonal Brillouin zone ($\mathbf{K}$ and $\mathbf{K}' = -\mathbf{K}$). When lattice anisotropy is introduced, the Dirac points move away from these positions. If the anisotropy is large enough, the Dirac points will eventually merge and a topological transition occurs [118–120]. The significance of this transition in condensed-matter physics has lead to extensive theoretical and experimental efforts [113, 115, 117–119]. However, this phenomenon is extremely challenging to observe in graphene or any other solid-state materials because of the unrealistic lattice anisotropy required. Instead, researchers mainly focus on artificial honeycomb lattices, including trapping ultracold atoms in honeycomb optical lattices [113, 118] and nano-patterning 2D electron gases [121, 122] for better tunability.

In this article, we present a new mechanism to move Dirac points and facilitate a topological transition in graphene based on periodic patterning of defects. Specifically, anisotropic defects cause the Dirac points to move, whose shift can be evaluated according to the renormalization of graphene's three hopping parameters. Furthermore, the long-range order introduced by periodic defects can induce intervalley scattering between two Dirac points. The intervalley scattering condition leads to a transition from semimetal to semiconductor without requiring the Dirac points to merge and annihilate. Our theoretical analysis is consistent with *ab-initio* electronic structure calculations. Therefore, patterned graphene can serve as a tunable platform to adjust the effective mass of fermions and study electronically correlated

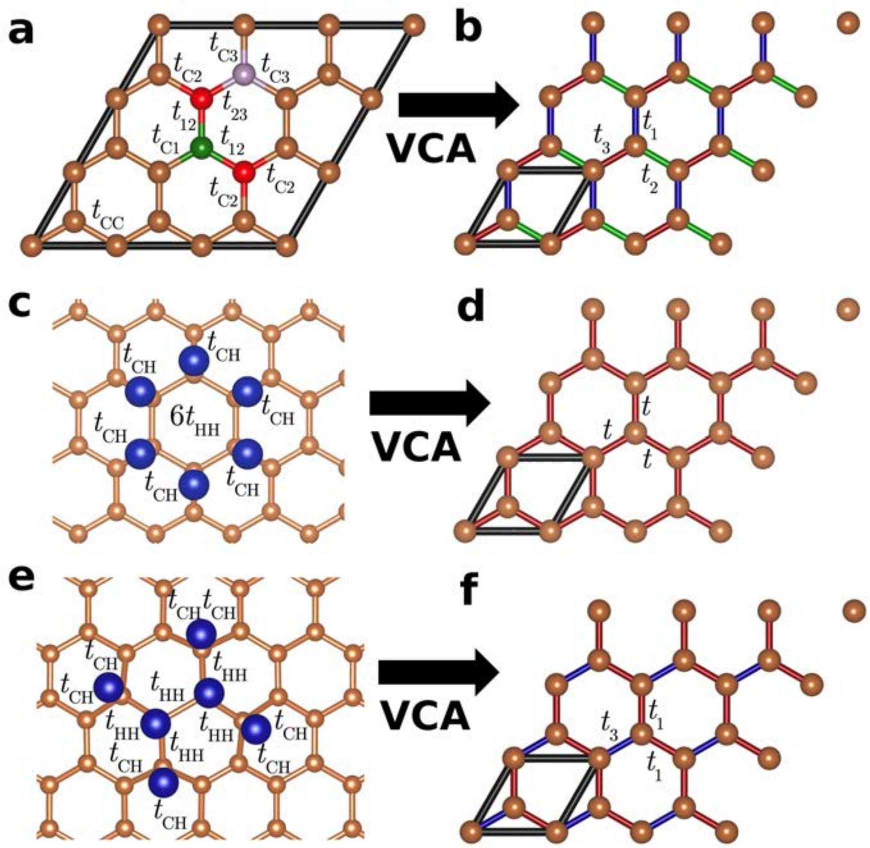

Figure 4.1: The virtual crystal approximation. (a,b) In the VCA, a defected graphene supercell is replaced by a 2-atom primitive cell with supercell averaged hopping parameters t_1, t_2 and t_3. (c,d) Isotropic defect of a 6C-ring passivated with hydrogen that preserves the local C_3 symmetry so that $t_1 = t_2 = t_3 = t$. (e,f) Anisotropic H-passivation defect formed from adjacent halves of two 6C-rings (split-6C) that breaks C_3 symmetry with $t_1 = t_2 \neq t_3$.

topological phase transitions.

4.2 Results

4.2.1 Quantifying anisotropy in patterned graphene

Various periodic defects have been realized on graphene, such as partially H-passivated graphene [74, 91], graphene nanomesh [6, 123] (GNM), and graphene doped with patches of hexagonal BN [26]. Recent works [6, 123] have demonstrated functional field-effect transistors based on patterned semiconducting graphene; however, the interplay between local defect configurations and long-range order in these materials is still unclear.

We have studied isotropic defects without breaking the local C_3 symmetry in the past [10, 103, 124], i.e., on average, the three hopping parameters (t) in the tight-binding (TB) graphene model [45, 101] remain identical. Here we focus on *anisotropic* defects that result in different renormalized hopping strengths. The anisotropy in defected graphene can be quantified by simply averaging the three nearest-neighbor hopping parameters in a supercell, i.e., the virtual crystal approximation (VCA) [125, 126] in solid-state physics. Based on the VCA, we model a large defected graphene supercell by a two-atom primitive cell with three distinct hopping parameters t_1, t_2, and t_3, as illustrated in Figure 4.1. The details of our VCA model are in Supplementary Information.

4.2.2 Dirac point drift

While the defected supercells shown on the left side of Figure 4.1 are difficult to deal with, their corresponding VCA model structures on the right side are well understood analytically at the TB level of theory [110, 118–120]. In a honeycomb lattice with three different hopping parameters and bond length a, Dirac points still satisfy $\mathbf{D'} = -\mathbf{D}$, but their locations [118] are:

$$\begin{aligned} D_{x,\pm} &= \pm\frac{2}{a}\arccos\left(-\sqrt{\frac{t_3^2-(t_2-t_1)^2}{4t_1t_2}}\right), \\ D_{y,\pm} &= \pm\frac{2}{\sqrt{3}a}\mathrm{sgn}(t_1-t_2) \\ &\quad \arccos\left(\frac{t_1+t_2}{t_3}\sqrt{\frac{t_3^2-(t_2-t_1)^2}{4t_1t_2}}\right). \end{aligned} \tag{4.1}$$

Previous work [110] has demonstrated that strain can move Dirac points according to Equation 4.1. Here, we show that we can modify the VCA hopping parameters and move the Dirac points along predictable paths in reciprocal space by adjusting the local defect structure, as demonstrated by Figure 4.2. Specifically, Figure 4.2b and Figure 4.2c indicate that Dirac points drift along the k_y axis for defects with $t_1 = t_2 \neq t_3$, corresponding to the case sketched in Figure 4.1f. Figure 4.2d and Figure 4.2e show the movement of Dirac

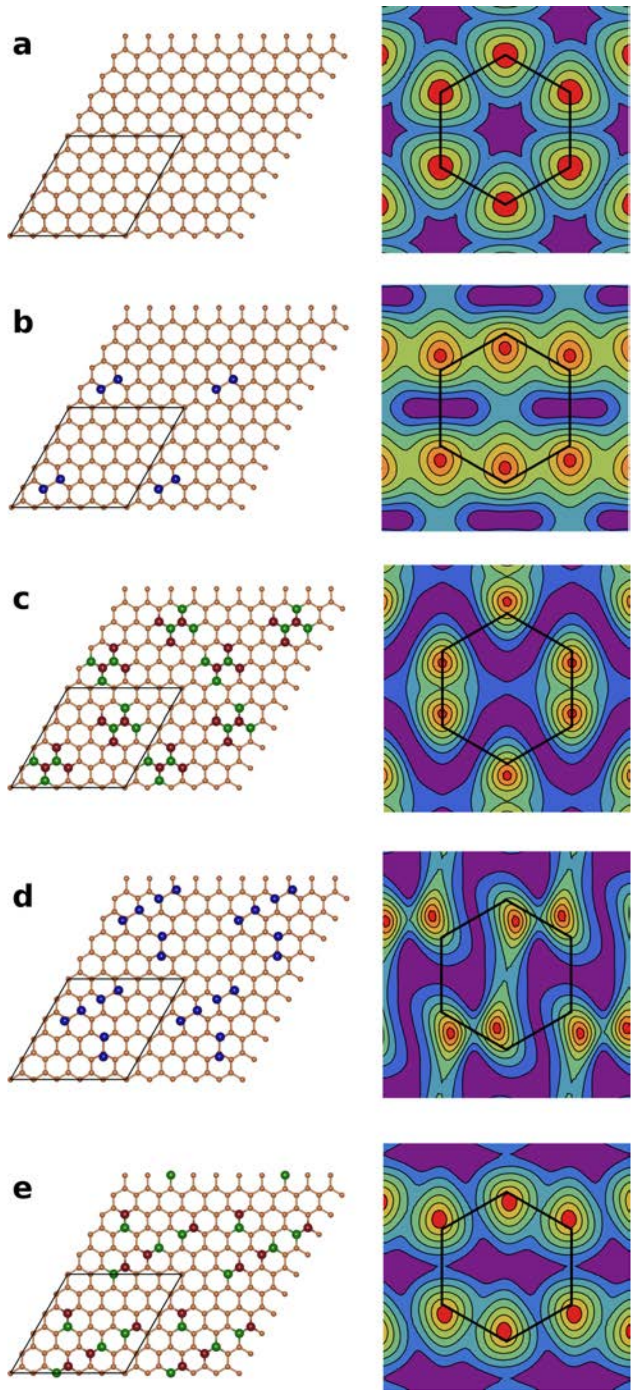

Figure 4.2: Dirac point drift. Crystal structures (left column) and contour plots of the energy for the highest valence band (right column) at each **k**-point in the Brillouin zone (black hexagon, for the 5×5 supercell) of defected graphene. The highest energy points (centers of the red areas) indicate the location of Dirac points. **a**, Pristine graphene. **b** and **d**, Partial hydrogen passivation. **c** and **e**, Boron nitride (BN) doping. Here, brown, blue, green, and dark red dots represent C, H, B and N atoms, respectively. All graphene structures have the same 5×5 hexagonal supercell indicated by solid black lines (left column).

points when all three VCA hopping parameters are unequal, $t_1 \neq t_2 \neq t_3$, corresponding to Figure 4.1b. Since boron nitride doping produces a much weaker perturbation than hydrogen passivation, the Dirac point shift in Figure 4.2c and Figure 4.2e is smaller than that in Figure 4.2b and Figure 4.2d, respectively.

Using Equation 4.1, one can determine the magnitude of Dirac point movement in patterned graphene in terms of the VCA hopping parameters. For instance, the anisotropic split-6C ring defect (Figure 4.1e) leads to:

$$\begin{aligned} t_1 &= t_2 = \left(1 - \frac{4}{3} f_d\right) t_{\mathrm{CC}} + \frac{2}{3} f_d (t_{\mathrm{HC}} + t_{\mathrm{HH}}), \\ t_3 &= \left(1 - \frac{5}{3} f_d\right) t_{\mathrm{CC}} + \frac{4}{3} f_d t_{\mathrm{HC}} + \frac{1}{3} f_d t_{\mathrm{HH}}, \end{aligned} \tag{4.2}$$

where the defected fraction $f_d \equiv N_{\mathrm{H}}/N_{\mathrm{C}}$, with N_{H} and N_{C} the numbers of H and C atoms in a supercell. t_{CC}, t_{HC}, and t_{HH} are hopping parameters between two C atoms without H passivation, one bare C atom and one passivated C atom, and two passivated C atoms, respectively. Inserting Equation 4.2 into Equation 4.1 and expanding the arccos function to linear order in the defect fraction f_d, we obtain the position of the shifted Dirac point $\mathbf{D}$ for graphene with 6C-split defects:

$$D_y^{\mathrm{split}} = \frac{4\pi}{3a} - \frac{2(t_{\mathrm{CC}} - 2t_{\mathrm{HC}} + t_{\mathrm{HH}}) f_d}{3\sqrt{3}\, a t_{\mathrm{CC}}} + \mathcal{O}[f_d]^2. \tag{4.3}$$

Here, a is the nearest-neighbor C-C bond length, and we orient our coordinate system so that the movement of Dirac points is along the k_y direction for the case of $t_1 = t_2 \neq t_3$ (Figure 4.2b and Figure 4.2c).

Another example is the ‘pair’ defect formed by two adsorbed H atoms on top of a pair of adjacent C atoms (Figure 4.2b). Depending on the defect fraction f_d, the Dirac point moves to

$$D_y^{\mathrm{pair}} = \frac{4\pi}{3a} + \frac{2(t_{\mathrm{CC}} - 2t_{\mathrm{HC}} + t_{\mathrm{HH}}) f_d}{\sqrt{3}\, a t_{\mathrm{CC}}} + \mathcal{O}[f_d]^2. \tag{4.4}$$

Comparing the slopes of the linear expansions in Equations 4.3 and 4.4, we draw two conclusions: (i) split and pair defects cause the Dirac point to drift in opposite directions and

(ii) for an identical defect fraction, the magnitude of the k_y drift for split defects is less than that of pair defects. Direct verification of Dirac point movement predicted by Equations 4.3 and 4.4 is difficult because the values of t_{HC} and t_{HH} are unknown. Instead, we perform first-principles electronic structure calculations to examine the above two conclusions.

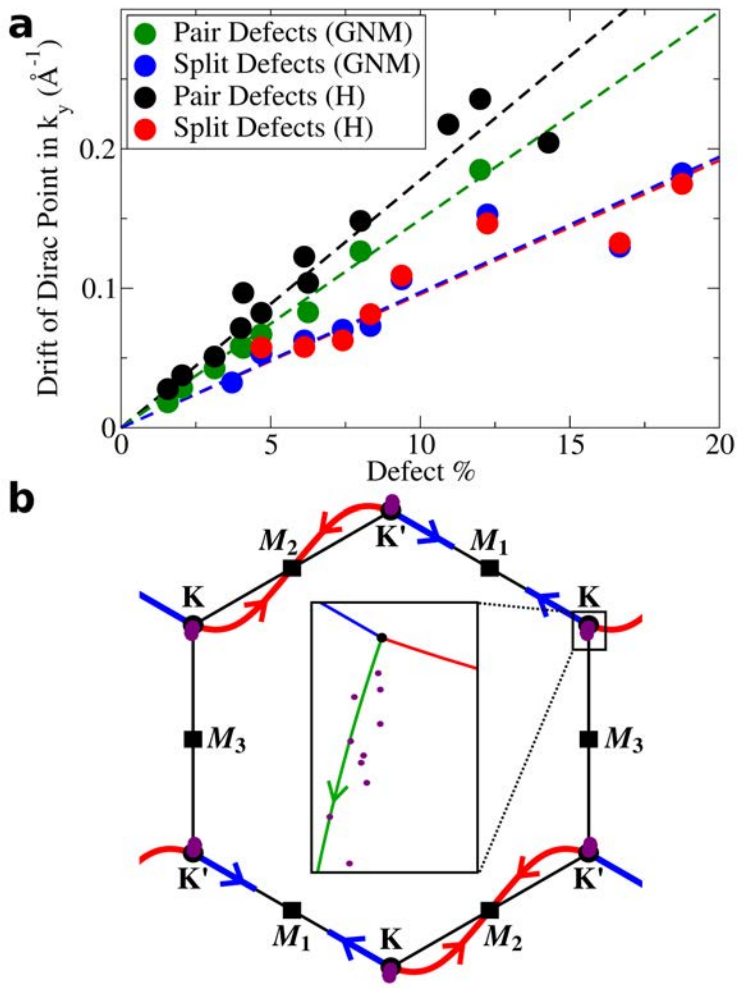

Figure 4.3: Dirac point drift vs. defect fraction. (a) Magnitude of Dirac point drift in 4 types of defected graphene as functions of defect fraction f_d. Dashed lines are linearly fitted to calculated data plotted with solid dots. For split defects, the drift is along the $-k_y$ direction, while the drift is along $+k_y$ for pair defects. Results for BN doping are presented in Supplementary Information Figure 4.7. (b) Blue and red solid lines are trajectories of Dirac points in reciprocal space as f_d increases for the two examples discussed in text. Purple dots are numerical data for the defect shown in Figure 4.2e and the green line is a numerical fit.

We track the movement of Dirac points in the $\pm k_y$ direction for graphene supercells with pair and split defects created by partial H-passivation, vacancies, and BN doping. We consider arbitrary supercell geometries and sizes to test the generality of our theory. By unfolding the Brillouin zones of these materials, we find the Dirac-like points derived from the Dirac points of pristine graphene. Our defining criterion for Dirac-like points is a gapless state with linear dispersion nearby. Some materials may have very small band gaps due to buckling of the graphene sheet or broken inversion symmetry. For our purposes, these materials are practically gapless. Not all materials show these Dirac-like points; the exceptions to this rule are semiconductors (when the topological phase transition occurs) and will be discussed shortly. Figure 4.3a demonstrates that for vacancy defects (GNM), the ratio of the fitted slopes for split and pair defects is 0.64, while this ratio is 0.54 for H-passivation. The direction of the Dirac point drift due to split defects is, as predicted, opposite that of pair defects (see Figure 4.2b and Figure 4.2c). Our VCA tight-binding model, therefore, can qualitatively predict the movement of Dirac points in graphene with anistropic defects.

We now turn our attention to the case $t_1 \neq t_2 \neq t_3$. It proves convenient to reparameterize the VCA hopping parameters according to

$$\begin{aligned} t_1 &= (1-f_d)t_{\mathrm{CC}} + f_d t'_1, \\ t_2 &= (1-f_d)t_{\mathrm{CC}} + f_d t'_2, \\ t_3 &= (1-f_d)t_{\mathrm{CC}} + f_d t'_3. \end{aligned} \tag{4.5}$$

Here, the t'_i parameters represent the hopping in the i^{th} direction averaged *only* for the defected C atoms. These values enter the VCA with the weight f_d, and the remainder of the supercell is the usual C-C hopping with the weight $(1-f_d)$. We explore the evolution of the Dirac points as a function of defect fraction f_d for different combinations of t'_1, t'_2 and t'_3 analytically (details in Supplementary Info) and then compare with numerical results from first-principles calculations.

Three examples are plotted in Figure 4.3b. The blue curve corresponds to $t'_1 = t'_{2'} = 6t_{\mathrm{CC}}$, $t'_3 = 11t_{\mathrm{CC}}$, the red curve depicts the case $t'_1 = 4t_{\mathrm{CC}}$, $t'_2 = 3t_{\mathrm{CC}}$, $t'_3 = -t_{\mathrm{CC}}$, whereas the green curve is a numerical fit to the purple data points computed for the BN defect shown in Figure 4.2e. All these trajectories begin at the $\mathbf{K}$ or $\mathbf{K}'$ points and evolve towards an $\mathbf{M}$ point of the Brillouin zone as f_d approaches 1. Note that the upper bound on anistropy is when f_d is 1, which may not induce high enough anisotropy to merge the Dirac points at an $\mathbf{M}$ point. If they do merge, a topological transition from semimetal to semiconductor occurs. Figure 4.3b suggests that, among these three cases, only the red curve can cause the Dirac points to merge. However, such large values of f_d and t'_i are unrealistic, and any practical anisotropy induced by defects can only generate a small amount of Dirac point drift (e.g., the green curve and purple data points). Nonetheless, the intriguing semimetal to semiconductor phase transition can be realized in periodically defected graphene by intervalley scattering.

4.2.3 Topological phase transition

While scientifically very interesting, drifting Dirac points also have important ramifications for technological applications. When the Dirac points drift on top of each other, a topological transition occurs and a bulk band gap opens [110, 114, 118, 119]. As already stated, the degree of anisotropy required for the Dirac points to merge is unreasonably large. For example, in strained graphene, uniaxial strains of around 20% are necessary to facilitate this transition [111, 112].

Fortunately, the long-range order created by defects provides an alternative route to opening a band gap at the Dirac points without the need for such high anisotropy [10, 13, 15, 103, 124]. Previous work has shown that band gap opening under an external potential is not possible when the potential varies slowly over the scale of the interatomic distance [78, 127–129]. However, if the external potential $U(\mathbf{G})$ has appreciable contributions at high wave vectors $|\mathbf{G}| \sim |\mathbf{D}|$, as we expect in defected graphene, bulk band gap opening is possible.

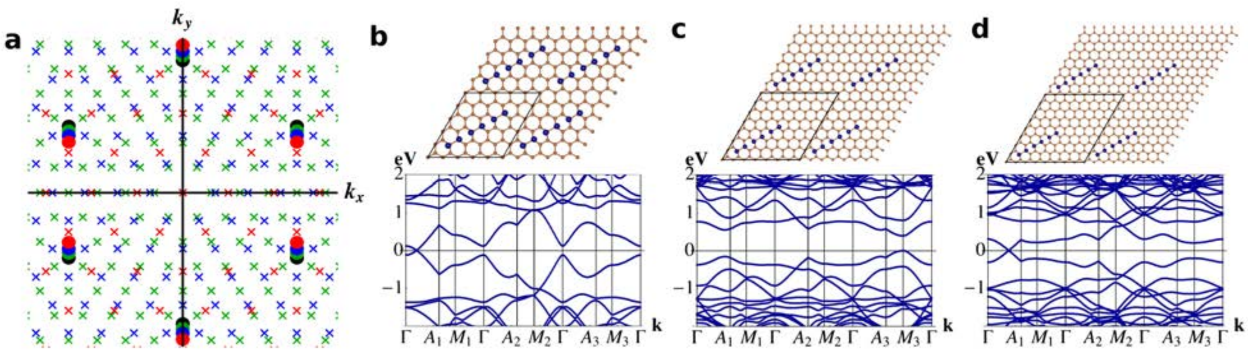

Figure 4.4: Numerical search for topological phase transition in graphene with anisotropic defects. (a) Black dots indicate the original positions of the Dirac points in pristine graphene. After unfolding their respective Brillouin zones, red and green dots correspond to equivalent positions of the Dirac point for 5×5 (panel (b) and 8×8 (panel (c)) supercells subject to three H-pair defects. The blue dot corresponds to the unfolded **k**-point location of the band gap in a 7×7 supercell (panel (c)) subject to three H-pair defects. Red, blue, and green $\times$'s mark the reciprocal lattice vectors of their respective structures. Only the blue dot falls at an **M** or **G** point of its Brillouin zone. (b,c,d) Crystal and electronic structures of the 5×5, 7×7 and 8×8 supercells with three H-pair defects presented in panel (a).

The topological phase transition takes place when the intervalley scattering condition $U(\mathbf{D} - \mathbf{D}') \neq 0$ is satisfied. This condition is equivalent to the requirement that the Dirac points drift onto a supercell reciprocal lattice vector ($\mathbf{G}$) or onto a middle point $\mathbf{M} = \mathbf{G}/2$. To test our prediction, we numerically search for defected graphene structures with drifted Dirac points that satisfy the intervalley scattering condition. This search is quite challenging because the degree of Dirac point movement is only known numerically, and each supercell has its own set of reciprocal lattice vectors. For a given defect, changing the size of the supercell changes not only f_d and the position of the Dirac points, but also changes the high symmetry points of the Brillouin zone.

Figure 4.4a shows a successful search for such a transition schematically. For a fixed defect of three H-passivation pairs, the drift of the Dirac point decreases as the size of supercell increases from 5×5 to 8×8 (red to green, Figure 4.4b to Figure 4.4d). As f_d decreases, the shift of Dirac points is reduced; the 7×7 supercell has an $\mathbf{M}$ point overlapping with $\mathbf{D}$, as indicated in Figure 4.4a, inducing intervalley scattering between two Dirac points and resulting in gapped and parabolic dispersion at $\mathbf{M}_3$ in the calculated electronic band structure.

One can also add defects to a fixed supercell to increase defect fraction f_d and Dirac point drift, as summarized in Figure 4.5. Figure 4.5a, Figure 4.5c, and Figure 4.5e show that the Dirac point drifts away from $\mathbf{A}_2$ and towards a reciprocal lattice vector $\mathbf{G}$ as f_d increases. Once the Dirac point drifts onto a $\mathbf{G}$ vector, a topological phase transition occurs and the resulting electronic band structure has a gap at the Γ-point. Figure 4.5b, Figure 4.5d and Figure 4.5f show a similar trend: their Dirac points move towards an $\mathbf{M}$-point. Once the Dirac point drifts onto $\mathbf{M}_2$, the intervalley scattering condition is satisfied and a band gap opens at $\mathbf{M}_2$.

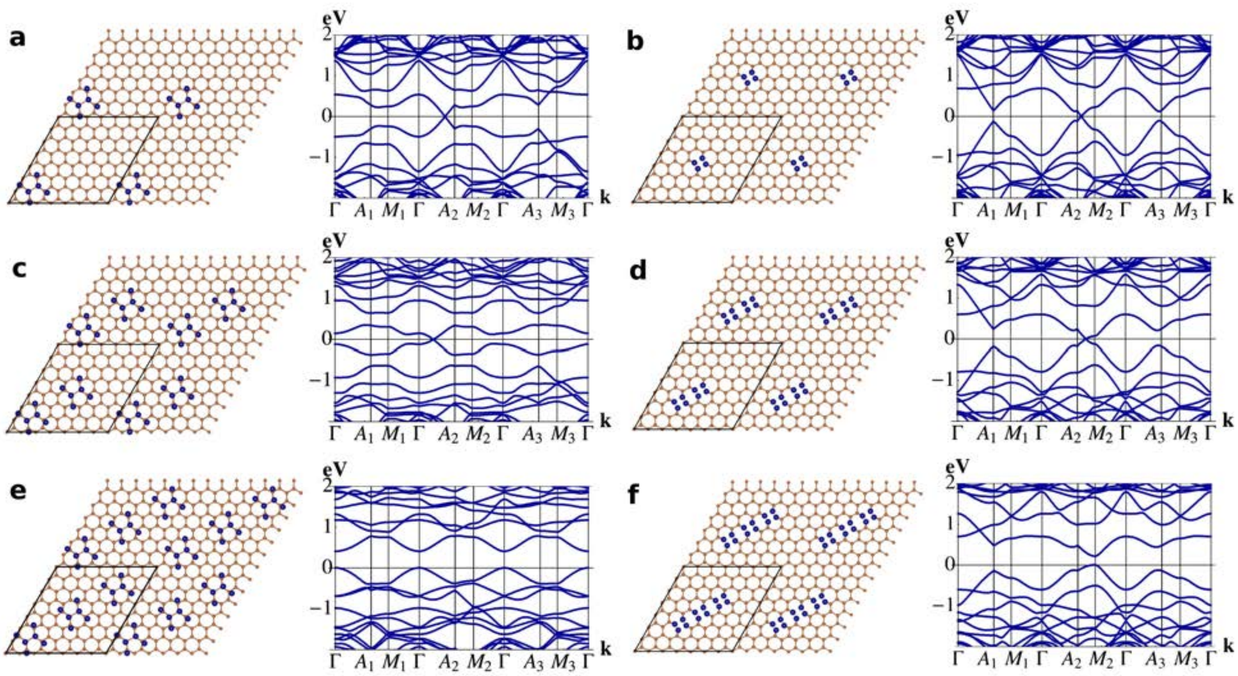

Figure 4.5: Topological phase transition in graphene by changing number of defects in a supercell. (a,c,e) Crystal (left) and electronic (right) structures of a 7×7 graphene supercell subject to one, two, and three split H-passivation defects, respectively. (b,d,f) Crystal (left) and electronic (right) structures of a 7×7 graphene supercell subject to one, two, and three pair vacancy defects, respectively.

4.3 Discussion

We have demonstrated the sensitivity of a defected graphene sheet's electronic structure to the geometries of both the supercell and the defect structure. The movement of Dirac points is well predicted by considering the local configuration of defects and the supercell size. The appearance of a band gap depends on both the local defect structure and the long range order. Therefore, patterned graphene could be a practical material to investigate the fundamental physics of Dirac point movement and the relevant topological phase transition in a solid-state system.

The seemingly complicated behaviors of Dirac points in these complex graphene systems can be understood by a simple effective TB model based on the VCA. Because the defect structures vary on the scale of the interatomic distance, they can induce intervalley scattering between the Dirac points and cause a semimetal-to-semiconductor transition. Not surprisingly, the intervalley scattering mechanism has a strong resemblance to the annihilation of merging Dirac points, leading to a topological phase transition in both cases. However, overlap of Dirac points in the *supercell* Brillouin zone simply due to zone folding *never* causes them to merge. For example, it is possible to construct a non-Bravais lattice of defected graphene such that the phase factors for each defect cancel, effectively reversing the appearance of a band gap and causing a semiconductor-to-semimetal transition [124]. In this case, the two Dirac points both overlap with $\mathbf{G}$ but they do *not* annihilate each other. The cancellation of phase factors is strong evidence that a scattering mechanism is responsible for band-gap opening in patterned graphene, not the merging of Dirac points.

Finally, the technological importance of such semiconducting graphene structures cannot be understated. Patterned graphene sheets with sizable band gaps have already been fabricated as electronic devices [6, 26, 74, 91, 92]. Despite these successes, however, a fundamental understanding of defects on graphene was missing, especially regarding the interplay between long-range order and local defect configuration. Our theory points out that the long-range order offers possible intervalley scattering while the local defect configuration can move Dirac points. When Dirac points meet a supercell reciprocal lattice vector **G** or a middle point $\mathbf{M} = \mathbf{G}/2$, a topological phase transition occurs and the massless fermions gain effective mass. Therefore, our work not only provides a platform to investigate the fundamental physics of Dirac cones, but also presents a reliable road map to designing semiconducting graphene materials.

4.4 Methods

Our first-principles electronic structure calculations based on density functional theory were performed using the SIESTA package [84] using a triple-ζ polarized atomic basis set for carbon atoms, whose numerical accuracy has been rigorously tested against the planewave-based VASP program [85]. The 2D Brillouin zones of supercells were sampled on a 2×2 Monkhorst-Pack **k**-point grid with good convergence due to very large primitive cells. The generalized gradient approximation [86] was used for the exchange-correlation functional. All calculations are spin-polarized. Structures are optimized until the maximum atomic force is less than 0.02 eV/Å. Dangling bonds in GNM structures are passivated with hydrogen atoms.

4.5 Acknowledgments

This work was financially supported by DOE Early Career Award (No. DE-SC0006433). Computations were carried out at the Golden Energy Computing Organization at CSM and NERSC.

4.6 Supplementary Information: Dirac point movement and topological phase transition in patterned graphene

4.6.1 Virtual crystal approximation

In the virtual crystal approximation (VCA), an effective 2×2 tight-binding (TB) Hamiltonian is constructed for a defected graphene supercell. First, on-site energies and hopping parameters are calculated for all N atoms in the supercell. These quantities are then averaged separately over graphene's A and B sublattices. After averaging, these values are inserted into the familiar TB Hamiltonian on a honeycomb lattice. We limit our discussion to on-site energies and nearest neighbor hopping only. The on-site energy of the i^{th} atom in the supercell $-$ a C atom or a defect $-$ is given by

$$E_i = \langle \phi_i(\mathbf{r} - \mathbf{R}_i) | \, H \, | \phi_i(\mathbf{r} - \mathbf{R}_i) \rangle \, . \tag{4.6}$$

Supercell averages give on-site energies for A and B sublattices. On-site energies are averaged over A- and B-sublattice separately. Each sublattice contains $N/2$ atoms in the supercell.

$$\begin{aligned} E_{\mathrm{A}} &= \frac{1}{N/2} \sum_{i \in \mathrm{A}}^{N/2} E_i \\ E_{\mathrm{B}} &= \frac{1}{N/2} \sum_{i \in \mathrm{B}}^{N/2} E_i \end{aligned} \tag{4.7}$$

There are three nearest neighbor vectors δ_j. The hopping parameter for the i^{th} atom in the j^{th} nearest neighbor direction is

$$t_{ji} = \langle \phi_{i+\delta_j}(\mathbf{r} - (\mathbf{R}_i + \delta_j) | \, H \, | \phi_i(\mathbf{r} - \mathbf{R}_i) \rangle \, . \tag{4.8}$$

The three distinct VCA hopping parameters t_j for each direction δ_j are calculated as

$$t_j = \frac{1}{N/2} \sum_{i \in \mathrm{A}}^{N/2} \sum_{k=j} t_{ik}. \tag{4.9}$$

Here, there are three distinct hopping parameters t_j. The sum over $k = j$ serves to pick out the proper j^{th} direction from all hopping parameters t_{ik}. The sum over i averages the hopping parameters over the $N/2$ atoms in the A sublattice. We only sum over the A sublattice to avoid double counting each hopping integral ($i \to k$ and $k \to i$). With the VCA hopping parameters, the locations of the Dirac points are at the roots of the following equation.

$$f(\mathbf{k}) = t_1 e^{i\mathbf{k}\cdot\delta_1} + t_2 e^{i\mathbf{k}\cdot\delta_2} + t_3 e^{i\mathbf{k}\cdot\delta_3} = 0 \tag{4.10}$$

4.6.2 Dirac point movement

On the isotropic honeycomb lattice, the Dirac points ($\mathbf{D}_{\pm}$) exist at the corners of the Brillouin zone ($\mathbf{K}$ and $\mathbf{K}'$), just as in pristine graphene. On the anisotropic honeycomb lattice, the Dirac points move away from $\mathbf{K}$ and $\mathbf{K}'$. When two of the hopping parameters are equal, $t_1 = t_2 \neq t_3$, the movement of the Dirac point is in only one direction [110].

$$\mathbf{D}_{\pm} = \left(\frac{2}{a} \arccos\left(-\frac{t_3}{2t_1} \right), 0 \right) \tag{4.11}$$

When all three hopping parameters are different, the Dirac points are located at [118]

$$\begin{aligned} D_{x,\pm} &= \pm\frac{2}{a} \arccos\left(-\sqrt{\frac{t_3^2 - (t_2 - t_1)^2}{4t_1t_2}} \right) \\ D_{y,\pm} &= \pm\frac{2}{\sqrt{3}a} \mathrm{sgn}(t_1 - t_2) \arccos\left(\frac{t_1 + t_2}{t_3} \sqrt{\frac{t_3^2 - (t_2 - t_1)^2}{4t_1t_2}} \right). \end{aligned} \tag{4.12}$$

Consider generic VCA hopping parameters given by

$$\begin{aligned} t_1 &= (1 - f_d)t_{\mathrm{CC}} + f_d t_1' \\ t_2 &= (1 - f_d)t_{\mathrm{CC}} + f_d t_2' \\ t_3 &= (1 - f_d)t_{\mathrm{CC}} + f_d t_3'. \end{aligned} \tag{4.13}$$

Here, t_i' represents the hopping parameter in the i^{th} direction averaged *only* for the defect atoms. By considering the surrounding C atoms, the t_i' enter the VCA with the weight of f_d; ordinary C-C hopping enters with the weight $(1 - f_d)$.

After inserting Equation 4.13 into Equation 4.1, the Dirac points are located at

$$\begin{aligned} D_{x,\pm} &= \pm\frac{2}{a} \arccos\left(-\frac{1}{2}\sqrt{\frac{(f_d t_3' + (1 - f_d)t_{\mathrm{CC}})^2 - (f_d t_2' - f_d t_1')^2}{(f_d t_1' + (1 - f_d)t_{\mathrm{CC}})(f_d t_2' + (1 - f_d)t_{\mathrm{CC}})}} \right) \\ D_{y,\pm} &= \pm\frac{2}{\sqrt{3}a} \mathrm{sgn}(f_d t_1' - f_d t_2') \\ &\quad \arccos\left(\frac{(f_d t_1' + f_d t_2' + 2(1 - f_d)t_{\mathrm{CC}})\sqrt{\frac{-(-f_d t_1' + f_d t_2')^2 + (f_d t_3' + (1 - f_d)t_{\mathrm{CC}})^2}{(f_d t_1' + (1 - f_d)t_{\mathrm{CC}})(f_d t_2' + (1 - f_d)t_{\mathrm{CC}})}}}{2(f_d t_3' + (1 - f_d)t_{\mathrm{CC}})} \right) \end{aligned} \tag{4.14}$$

A few test cases illustrate how the Dirac points move in our VCA-TB approximation. When $t_1' = t_2' = t_3'$, the Dirac points remain at their original locations,

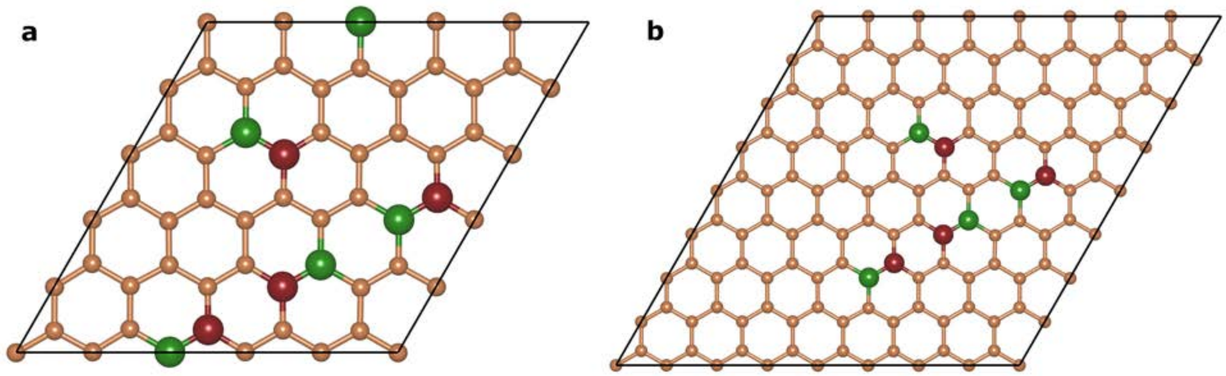

Figure 4.6: BN doped defect with $t'_1 \neq t'_2 \neq t'_3$.

$$\mathbf{D}_{\pm} = \pm\left(\frac{4\pi}{3a}, 0\right). \tag{4.15}$$

When $t'_1 = t'_2 = t_{\mathrm{CC}}$ and $t'_3 = 2t_{\mathrm{CC}}$, the Dirac points are at

$$\mathbf{D}_{\pm} = \pm\left(\frac{2}{a}\arccos\left(\frac{-(1+f_d)}{2}\right), 0\right). \tag{4.16}$$

The case $t'_1 = t_{\mathrm{CC}}$, $t'_2 = 2t_{\mathrm{CC}}$, $t'_3 = 3t_{\mathrm{CC}}$ has Dirac points at

$$\begin{aligned} D_{x,\pm} &= \pm\frac{2}{a}\arccos\left(-\frac{1}{2}\sqrt{1+3f_d}\right) \\ D_{y,\pm} &= \pm\frac{-2}{\sqrt{3}a}\mathrm{sgn}(f_d t_{\mathrm{CC}})\arccos\left(\frac{(2+f_d)\sqrt{1+3f_d}}{2+4f_d}\right) \end{aligned} \tag{4.17}$$

The defect averaged hopping parameters t'_i depend on the local defect geometry. For the BN defect shown in Figure 4.6, the t_i are

$$\begin{aligned} t'_1 &= (t_{\mathrm{CC}} + t_{\mathrm{BC}} + t_{\mathrm{NC}})/3 \\ t'_2 &= (7t_{\mathrm{CC}} + t_{\mathrm{BC}} + t_{\mathrm{NC}} + 3t_{\mathrm{BN}})/12 \\ t'_3 &= (5t_{\mathrm{CC}} + t_{\mathrm{BN}} + 3t_{\mathrm{BC}} + 3t_{\mathrm{NC}})/12. \end{aligned} \tag{4.18}$$

The two supercells in Figure 4.6 have identical defects and, hence, identical t'_i. These two structures demonstrate a practical realization to test the parameterization of the hopping parameters in Equation 4.13 and the movemement of Dirac points based on Equation 4.14.

4.6.3 BN doping

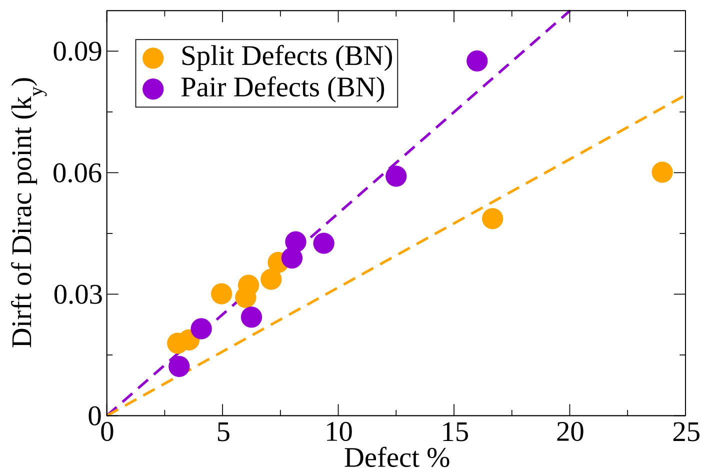

Figure 4.7: Drift of Dirac points depends on defect fraction. The drift of the Dirac point in BN doped graphene increases with defect fraction. Plotted values are the magnitude of the drift. For split defects, the drift is in the $-k_y$ direction, and for pair defects, the drift is in the $+k_y$ direction. Overall balance in on-site energies between A and B sublattices is achieved by switching B and N dopants between sublattices for different defects. Hence, each BN doped supercell must have an even number of defects. The ratio of the fitted slopes is 0.63.

4.6.4 Brillouin zone

The Brillouin zone, high symmetry points, and band structure path of the 5×5 graphene supercell used in the text are shown below in Figure 4.8. All plotted band structures belong to hexagonal supercells with the same shape. Therefore, all Brillouin zones have the same shape and high symmetry points and differ only in size. Hexagonal supercells are particularly convenient for tracking the movement of Dirac points in the case of $t_1 = t_2 \neq t_3$ because the Dirac points move in a direction that is along the band structure path shown here. For an arbitrarily shaped supercell, the Dirac points may move off of the band structure path and not be visibile in the band structure plot.

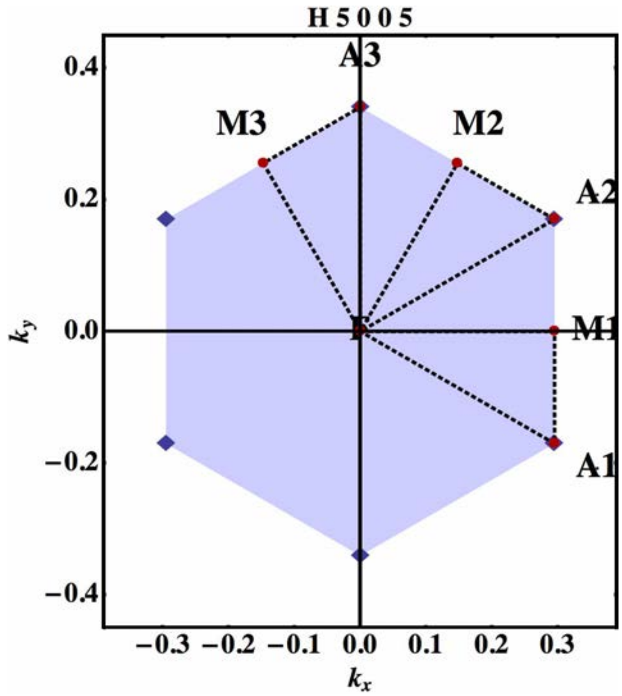

Figure 4.8: BZ of 5×5 graphene supercell.

4.6.5 Intervalley scattering

Consider Dirac points at the positions in reciprocal space $\mathbf{D}$ and $\mathbf{D'} = -\mathbf{D}$. The scattering matrix element between eigenstates of pristine graphene is given by [78]

$$\langle s, \mathbf{k}| \, U(\mathbf{r}) \, |s', \mathbf{k}'\rangle = \sum_{\mathbf{G}} \frac{1}{2}(1 + ss'e^{-i\theta_{\mathbf{k},\mathbf{k}'}})U(\mathbf{G})\delta_{\mathbf{k}',\mathbf{k}-\mathbf{G}} \tag{4.19}$$

where $\theta_{\mathbf{k},\mathbf{k}'}$ is the angle in reciprocal space between the scattered states.

If the impurity potential $U(\mathbf{r})$ has a range much larger than the carbon-carbon distance in graphene, intervalley scattering does not occur between $\mathbf{D}$ and $\mathbf{D'}$ and a band gap can not open [78, 127]. However, if the perturbing potential has oscillations on the order of the carbon-carbon distance, $U(\mathbf{G})$ has significant contributions at large $|\mathbf{G}|$ − such as some $\mathbf{G}$ connecting $\mathbf{D}$ and $\mathbf{D'}$ − and band gap opening can occur. This is the case for structural modifications on graphene. Defects create a scattering potential somewhere between a slowly varying potential and a perfectly localized δ-function.

The intervalley scattering matrix element is nonzero only if $\mathbf{D}$ and $\mathbf{D}'$ can be connected by a reciprocal lattice vector. This can only occur if the Dirac points are at certain high symmetry locations in the Brillouin zone. The Kroenecker-δ in Equation 4.19 is satisfied when the Dirac points drift to the zone center (Γ) or the points $\mathbf{M}_i = \mathbf{G}_i/2$. When $\mathbf{D} = \mathbf{D}' = \Gamma \mod \mathbf{G}_i$,

$$\mathbf{D} - \mathbf{D}' = 2\mathbf{G}_i. \tag{4.20}$$

When $\mathbf{D} = \mathbf{M} = \mathbf{G}_i/2$ and $\mathbf{D}' = -\mathbf{M} = -\mathbf{G}_i/2$,

$$\mathbf{D} - \mathbf{D}' = \mathbf{G}_i. \tag{4.21}$$

CHAPTER 5

TUNABLE MANY-BODY INTERACTIONS IN SEMICONDUCTING GRAPHENE: GIANT EXCITONIC EFFECT AND STRONG OPTICAL ABSORPTION

Adapted from an article under review with

Physical Review B.

Marc Dvorak [8,9], and Zhigang Wu[8,9]

Electronic and optical properties of graphene depend strongly on many-body interactions. Employing the highly accurate many-body perturbation approach based on Green's functions, we find a large renormalization over independent particle methods of the fundamental band gaps of semiconducting graphene structures with perodic defects. Additionally, their exciton binding energies are larger than 0.4 eV, suggesting significantly strengthened electron-electron and electron-hole interactions. Their absorption spectra show two strong peaks whose positions are sensitive to the defect fraction and distribution. The strong near-edge optical absorption and excellent tunability make these two-dimensional materials promising for optoelectronic applications.

5.1 Introduction

Since the discovery of graphene [1, 130–132], the physics of two-dimensional (2D) materials, including boron nitride (BN) monolayer [133] and transition-metal dichalcogenides [134], has been a rapidly evolving research field [135]. Graphene possesses exceptional charge carrier mobilities [68], unusual optical properties [12, 82], and exotic topological phases [109, 136], showing great promise in replacing bulk semiconductors to build next-generation optoelectronic devices [6, 66]. In order to realize this vision, however, electronic and optical properties

[8]Department of Physics, Colorado School of Mines
[9]Researcher and Author

of graphene must be tunable. One practical approach is patterning graphene periodically with vacancies [6], passivants [137], dopants, [74] etc. Certain patterns of defects on graphene induce long-range order that causes a nonzero scattering matrix element between Dirac points and opens a sizable band gap (E_{g}). The magnitude of E_{g} in these semiconducting materials depends on defect size, type, and distribution [10, 15, 95, 99, 103, 124, 138].

In contrast to the electronic band structure, which can be well described within the picture of a single quasiparticle (QP) system, excitonic effects and optical spectra depend sensitively on two-QP (electron-hole) interactions as well, especially for low-dimensional materials. In low dimensional materials, low electronic screening and the close proximity of electron and hole lead to strengthened electron-electron and electron-hole interactions. Furthermore, the electron-electron interactions between the single-QP excitations are not correctly determined by single-particle methods, such as density functional theory (DFT), which tends to severely underestimate E_{g}. [58, 139, 140] The GW approximation [58, 139, 140] is the state-of-the-art approach to compute single-QP energies, and solving the Bethe-Salpeter equation (BSE) [57, 58, 141] for correlated electron-hole excitations has been remarkably successful in quantifying excitonic effects in low-dimensional materials [82, 142, 143]. Such GW-BSE calculations are very demanding, however, and have not yet been performed for these semiconducting graphene structures because of the large primitive cell size.

In this article, the QP energies and optical spectra of semiconducting graphene structures are computed to reveal the effects of defect size, geometric arrangement, and type on many-body interactions involved in electronic excitations. We consider vacancy defects that form graphene nanomeshes (GNMs) in hexagonal and rectangular arrangements, and BN doped graphene in a hexagonal arrangement. Our results show that DFT underestimates E_{g} of these materials by about 50%, suggesting strong many-body interactions. The independent-QP absorption spectra miss some essential features that are attributed solely to the electron-hole interaction. Each BSE absorption spectrum shows two strong and isolated peaks below a continuum of exciton states. Excitons are strongly bound, with giant binding energies (E_{b})

ranging from $0.46-0.81$ eV, in comparison to E_{g} of $1.3-2.2$ eV. The excitons form a non-hydrogenic series and individual exciton wave functions show a Γ-centered ring structure in the Brillouin zone. The absorption edge is also strongly dependent on defect size. By varying the fraction of the unit cell occupied by the defect, it is possible to tune the optical gap to essentially any value below ~ 1.4 eV, making these materials promising for optoelectronic applications.

5.2 Results

We use four parameters (n_1, m_1, n_2, m_2) to denote the translation vectors ($\mathbf{R}_1$ and $\mathbf{R}_2$) of a defected graphene supercell: $\mathbf{R}_1 = n_1\mathbf{a}_1 + m_1\mathbf{a}_2$ and $\mathbf{R}_2 = n_2\mathbf{a}_1 + m_2\mathbf{a}_2$ [103, 124], with $\mathbf{a}_1$ and $\mathbf{a}_2$ the primitive translation vectors of pristine graphene. As long as the defect has average hexagonal symmetry [144], the $\mathbf{K} \leftrightarrow \mathbf{K}'$ scattering condition for a semiconductor is equivalent to $n_1 - m_1 = 3p$ and $n_2 - m_2 = 3q$ for integers p and q. In this work, we consider $(n_1, m_1, n_2, m_2) = (6, 0, 0, 6)$ and $(6, -6, 3, 3)$ supercells. The $(6, 0, 0, 6)$ hexagonal supercell has both edges along the zigzag direction, while the $(6, -6, 3, 3)$ rectangular supercell has one edge along an armchair direction and the other along a zigzag direction. In this article, we refer to these two systems simply as hexagonal and rectangular, and consider vacancy and BN doping defects that occupy 6 C (one hexagonal ring) and 12 C atoms. The four systems investigated are shown on the left side of Figure 5.1.

Our *ab-initio* GW calculations are performed on a 4×4 $\mathbf{k}$-point grid (equivalent to a 24×24 $\mathbf{k}$-point sampling in the Brillouin zone of pristine graphene for the $(6, 0, 0, 6)$ structure) using the Quantum Espresso [145] and BerkeleyGW [62] packages. DFT calculations are performed with the PBE-GGA [86], norm-conserving pseudopotentials, and a cutoff energy of 60 Ry. We find the GW self-energies (Σ) converged for the dielectric function with a cutoff energy of 10 Ry. Unlike the 2D transition-metal dichalcogenides [142, 146], these systems do not show localized states, leading to fast convergence of Σ. Summations over empty states to compute Σ include 5×10^3 unoccupied bands, so that QP energies are converged to within 0.1 eV. We use the generalized plasmon-pole model of Hybertsen and Louie [139].

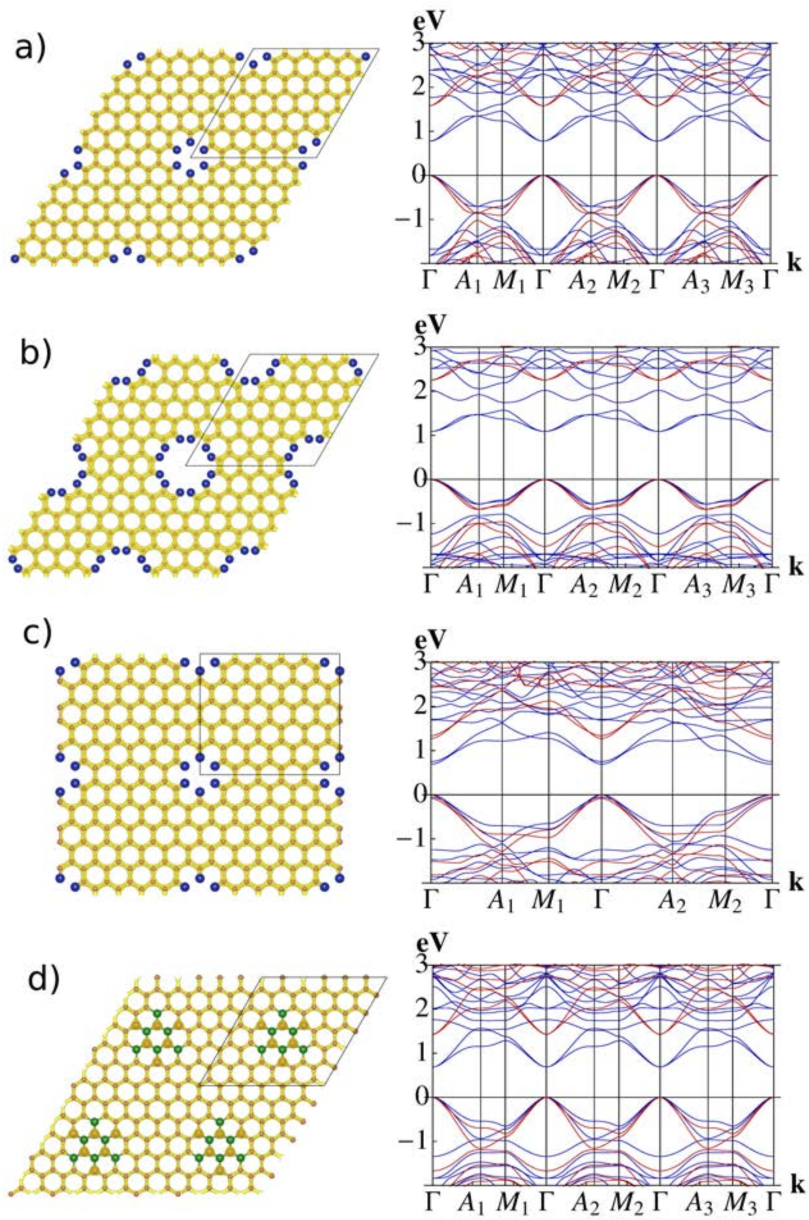

Figure 5.1: Crystal (left column) and electronic band (right column) structures of defected graphene structures. Yellow isosurfaces (left) indicate the total charge density. Blue and red lines (right) correspond to DFT and GW band structures, respectively. Hole edges are passivated by hydrogen (blue dots). (a) $(6, 0, 0, 6)$ GNM with a 6-C hole. (b) $(6, 0, 0, 6)$ GNM with a 12-C hole. (c) $(6, -6, 3, 3)$ GNM with a 6-C hole. (d) $(6, 0, 0, 6)$ BN doped graphene with 12 C atoms replaced by hexagonal BN (green and gold dots). Band gaps, in eV, are (a) (DFT, GW) = (0.78, 1.58), (b) (1.09, 2.26), (c) (0.69, 1.27), and (d) (0.69, 1.43).

The right four panels of Figure 5.1 show the electronic band structures of the four systems studied, which are all semiconducting with a direct gap at Γ. All of them have two isolated (or nearly isolated) valence (conduction) bands near the Fermi energy below (above) the band gap. The GW band gap is almost double the DFT gap, with the renormalization factor $E_{\mathrm{g}}^{GW}/E_{\mathrm{g}}^{\mathrm{DFT}} \approx 1.8 - 2.1$, a stronger enhancement due to many-body interactions than is typically seen in bulk insulators. We attribute this effect to the low screening and strong electron-electron interaction in 2D materials compared with their bulk counterparts.

In GNMs, as the hole size increases, E_{g} increases, scaling roughly $\propto \sqrt{N_{\mathrm{C}}^{\mathrm{removed}}}/N_{\mathrm{C}}^{\mathrm{original}}$, with $N_{\mathrm{C}}^{\mathrm{removed}}$ and $N_{\mathrm{C}}^{\mathrm{original}}$ the numbers of removed and original C atoms, respectively. For example, E_{g} increases from 1.58 eV to 2.26 eV as the hole size increases from 6-C to 12-C in GNMs plotted in Figure 5.1a and Figure 5.1b. Similar scaling rules for structurally modified graphene based on tight-binding or DFT have been proposed previously [10, 18, 103, 124], but here we present GW results for the first time. In principle, one can tune E_{g} in patterned graphene to any desired value by varying defect percentage or supercell size. Moreover, for the same defect percentage, E_{g} can also vary considerably, e.g., $E_{\mathrm{g}} = 1.27$ eV in the rectangular GNM shown in Figure 5.1c, compared to $E_{\mathrm{g}} = 1.58$ eV in the hexagonal GNM (Figure 5.1a) with the same $N_{\mathrm{C}}^{\mathrm{removed}}$ and $N_{\mathrm{C}}^{\mathrm{original}}$. Clearly, the geometric arrangement of the defects has a nontrivial effect on the band gap as well. Finally, Figure 5.1b and 1d provide a comparison of vacancy defects versus BN dopants. For the same defect size, BN dopants are a smaller perturbation than vacancies and open a considerably smaller band gap (reduced by about one third). The electronic structure shown in Figure 5.1d is similar to that of the corresponding GNM (Figure 5.1b) in spite of the fact that the GNM preserves A- B-sublattice symmetry and BN dopants do not. The combined effects of sublattice imbalance and intervalley scattering are explored in our previous work [124].

Our primary focus in this work is the optical properties of defected graphene. To account for the electron-hole interaction, we use BerkeleyGW to solve the BSE for the two-QP eigenstates [62]. We compute the electron-hole interaction on the same 4×4 grid of **k**-points, and then interpolate the matrix elements onto a 20×20 **k**-point grid. For the hexagonal systems, this is equivalent to a 120×120 **k**-point sampling of a graphene primitive cell. Such a dense **k**-point sampling is required to converge exciton eigenvalues within 40 meV. DFT wave functions are used as the basis, with GW QP energies used in place of DFT eigenvalues. The screened interaction is evaluated up to 10 Ry, and all independent-QP transitions up to 6 eV are used to construct the Hamiltonian.

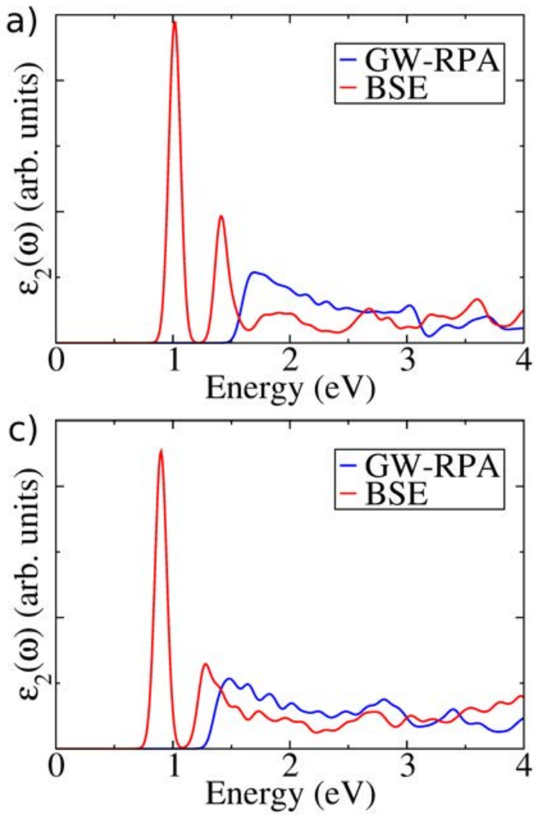

Figure 5.2: Imaginary part of the dielectric function for hexagonal systems with a (a) 6-C hole, (b) 12-C hole, (c) rectangular system with a 6-C hole, and (d) hexagonal system with 12 C atoms replaced by BN dopants.

Figure 5.2 shows the imaginary dielectric functions (ϵ_2) for the same four systems as shown in Figure 5.1. In each case, the excitonic absorption edge is red-shifted by roughly 0.5 eV compared to the GW-RPA (random phase approximation) spectrum. The BSE spectra all show two prominent absorption peaks before reaching a continuum of exciton states, which are missing from the non-interacting single-QP estimation. The oscillator strengths of these peaks are enhanced considerably compared to any of the peaks in the non-interacting spectra.

Specifically, there are two absorption peaks at 1.02 and 1.41 eV in Figure 5.2a; below 1.02 eV, there exists a single dark state at 0.97 eV. This state is bound by $E_\mathrm{b} = 0.61$ eV below the band gap, and such strongly bound excitons are typical of low-dimensional systems, and comparable values have been theoretically predicted and observed experimentally in 2D materials [142, 143, 146, 147]. In comparison, the electron-hole binding energy in covalently bonded bulk semiconductors is typically only tens of meV, although certain ionic compounds have Frenkel excitons bound by hundreds of meV [65, 148]. It is important to note that our calculations are performed for a free-standing GNM without substrate. Experimentally, GNMs are likely to be fabricated on a substrate, which could reduce E_b and shift absorption peaks because of the enhanced screening [146].

In the following, we analyze excitons of the GNM shown in Figure 5.1a. The first absorption peak is comprised of three degenerate states (excitons $2-4$) originating from transitions directly at Γ. Figure 5.3a shows the modulus squared of the third exciton wave function and the weights in the Brillouin zone of Bloch waves contributing to the exciton. Away from Γ, the contributions to the exciton decrease rapidly. The first four excitons, including the dark state, all have similar character: they are approximately azimuthally symmetric in real space and localized functions with a single peak in $\mathbf{k}$-space. These four states are made of different mixings of the two degenerate valence and two degenerate conduction bands at Γ. Not surprisingly, the low energy absorption is dominated by these nearly isolated pairs of valence and conduction bands near the band gap in Figure 5.1a.

Next, there are two degenerate dark states with similar character at 1.32 eV. Shown in Figure 5.3b, these states are primarily comprised of six transitions in a ring surrounding Γ. The six-fold symmetric maxima in $\mathbf{k}$-space are located along the $\Gamma - \mathbf{M}$ directions of the Brillouin zone. In real space, the wave function has two lobes, resembling a p-type wave function. In general, we find that exciton spectra of defected graphene do not resemble a hydrogenic series, agreeing with previous work on 2D materials [142, 143]. Certain exciton wave functions, however, still show a strong s- or p-type character. Excitons $7-10$ are two closely spaced pairs of degenerate states. In real space (Figure 5.3c), the exciton has a preferred direction but no obvious structure; in reciprocal space, however, the **k**-point weights form two lobes centered on a line going through Γ. For these four states, the orientation of the lobes varies between the $\Gamma - \mathbf{M}$ and $\Gamma - \mathbf{A}$ directions of the Brillouin zone with a minimum weight at Γ.

The next optically active state is the 14th exciton eigenstate, contributing to the second absorption peak at 1.41 eV. In **k**-space, the weights are peaked sharply at Γ – sharper than Figure 5.3a – pass through a minimum, and then form a nearly continuous ring around Γ. This state, together with higher exciton states, bear resemblance to the states shown in Figure 5.3 but acquire additional nodes in **k**-space as the excitation energy increases. Not until the continuum of states are there significant contributions to the optical absorption beyond the pairs of valence and conduction bands near the band gap (see Figure 5.1). In the continuum, the exciton states have a structure near the Γ-point similar to those shown in Figure 5.3 but slowly gain weight at **k**-points further away from Γ.

Figure 5.2b shows ϵ_2 for a hexagonal system with a 12-C hole. Due to its larger band gap, the absorption edge for this system is substantially blue-shifted compared to that in Figure 5.2a. Otherwise, both hexagonal GNMs share the same basic features, as expected. Here, the lowest exciton is bound by $E_\mathrm{b} = 0.81$ eV, which is $\approx 1/3$ stronger than that in the hexagonal supercell with a 6-C hole. This is because screening is reduced as the electron density decreases with increasing hole size, enhancing the electron-hole interaction. Additionally, a larger hole forces greater confinement of the electron and hole. This increased physical overlap of their wave functions also serves to enhance E_b.

We also consider the effect of geometric configuration of defects on ϵ_2. Figure 5.2c plots ϵ_2 for the rectangular GNM (Figure 5.1c). The rectangular system shows a slight red shift of its absorption spectrum compared with its corresponding hexagonal GNM, but its absorption generally has the same character as that of the hexagonal system. This is not surprising, given the similarities of the near gap bands plotted in Figure 5.1. However, because of the

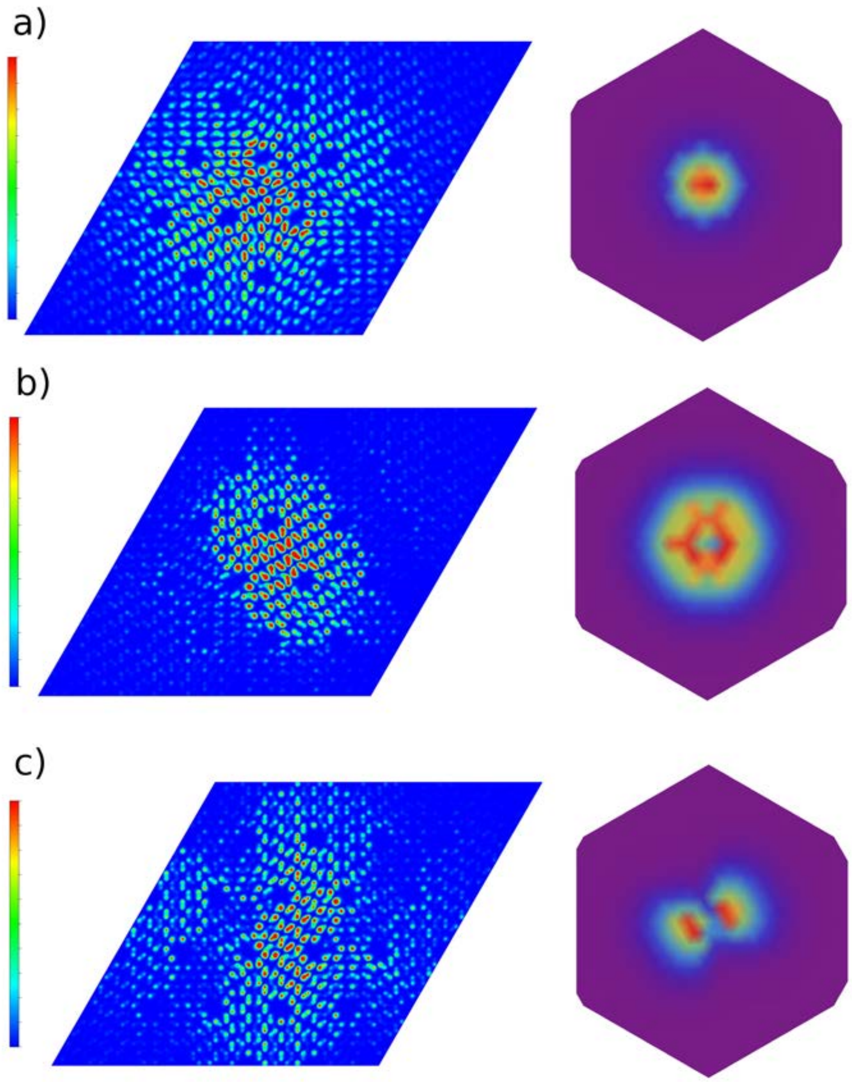

Figure 5.3: Real space plots of the exciton wave function modulus squared (left column) and weights in the Brillouin zone (right column) for the (a) third, (b) fifth, and (c) seventh lowest exciton eigenstates in a hexagonal GNM shown in Figure 5.1a. The hole in an exciton wave function is fixed at the center of the supercell, and the modulus squared of the electron coordinate is shown in the density plots. Real space plots are in a 6×6 supercell (left), and the purple hexagon is the Brillouin zone (right).

reduced symmetry of the rectangular system, several states that were completely dark in the hexagonal system now appear as very small shoulders near the main absorption peaks, though their enhancement is not significant enough to dramatically alter the shape of ϵ_2. Interestingly, the lowest exciton in the rectangular system is bound by only 0.46 eV, noticeably less than E_b in the corresponding hexagonal system with the same number of C atoms and hole size. One possible explanation for this difference is less confinement of electron and hole in a rectangular supercell compared to a hexagonal cell. If we consider the largest circle that can fit on each supercell between the boundaries of defects, it is straightforward to show that the circle in the rectangular supercell has a larger radius than the circle in the hexagonal supercell. If we consider this 'confinement circle' as a crude measure of electron-hole confinement, the trend predicted by the circle radius agrees with the trend in our calculated values of E_b.

Finally, we compute the optical properties of the BN doped system shown in Figure 5.1d. Figure 5.2b and d provide a comparison of ϵ_2 for a GNM with a 12-C hole and a graphene sheet with 12 C atoms replaced by BN. There is a large red-shift of > 0.5 eV of the BN spectra because of its much reduced band gap, but the overall features of the absorption remain the same. The most striking difference between these two materials is their difference in exciton binding energy: $E_\mathrm{b}^{\mathrm{GNM}} = 0.81$ eV while $E_\mathrm{b}^{\mathrm{BN-doped}} = 0.48$ eV. As with the comparison of E_b between GNMs with 12-C and 6-C holes, increased electronic screening is likely responsible for the large reduction in E_b seen in BN-doped systems. Our results demonstrate great tunability of the optical band gap and exciton binding energy in periodically defected graphene.

5.3 Conclusion

In conclusion, we have reported *ab-initio* results for the electronic band structure and optical properties of 2D graphene-based semiconductors obtained from GW-BSE computations. The QP band gaps of these materials are roughly twice their DFT values, while the optical absorption shows two prominent peaks below the continuum of exciton states. Low-energy excitons are strongly bound and composed of transitions mixing the two highest valence bands with the two lowest conduction bands near the Γ-point. Our results demonstrate great sensitivity of structurally modified graphene's electronic and optical properties to size, type, and distribution of the defects, thus these 2D materials can be customized to make better optoelectronic devices. For example, varying the hole size in a GNM could tune the absorption edge in the $0 - 1.4$ eV range; due to its extremely efficient optical absorption, a layered GNM structure with varying hole and supercell size could be an ideal absorber material for photovoltaics. Furthermore, strong Coulomb interaction and a relatively small band gap would suggest efficient multi-exciton generation [149], while the strong and isolated absorption peaks make them good candidates for light-emitting diodes.

5.4 Acknowledgments

This work was supported by U.S. DOE Early Career Award (Grant No. DE-SC0006433). Computations were carried out at the Golden Energy Computing Organization at CSM and the National Energy Research Scientific Computing Center (NERSC). The authors thank M. Lusk and D. Wood for insightful discussions.

CHAPTER 6

GIANT BAND GAP QUANTUM SPIN HALL INSULATOR WITH WEAK SPIN-ORBIT COUPLING

Adapted from an article to be submitted to

Physical Review Letters.

Marc Dvorak [10,11], and Zhigang Wu[10,11]

The typical quantum spin Hall (QSH) insulator acquires its band gap through spin-orbit coupling (SOC). However, the intrinsic SOC in most materials is rather weak and creates small band gaps comparable to k_BT. Here, we present a new method to open a giant band gap (> 1 eV) in a QSH phase for arbitrarily weak SOC. We consider the tight-binding (TB) Kane-Mele model for the QSH insulator with the additional feature of periodic defects. By tuning the periodicity of structural defects, one can induce intervalley scattering and open a large band gap. Surprisingly, the characteristic metallic edge modes of a QSH phase persist even with the inclusion of such periodic defects. We perform TB calculations showing the existence of a Z_2 odd QSH phase in a Kane-Mele model modified to include periodic defects, outlining the path to a giant band gap QSH insulator without enhancing intrinsic SOC.

6.1 Introduction

Since the prediction of the quantum spin Hall (QSH) phase in graphene by Kane and Mele in 2005 [34, 35], research in the field of topological insulators has grown extensively [109, 136, 150–154]. Topological insulators are most easily explained by the idea of adiabatic continuation. By deforming the Hamiltonian, insulators belonging to the same topological class may be connected to each other without undergoing band gap closure at any point in

[10]Department of Physics, Colorado School of Mines
[11]Researcher and Author

between. For example, a set of isolated noble gas atoms may be brought together to form an insulating crystal with slight dispersion. Insulators belonging to different topological classes can only be connected along an adiabatic path which causes band gap closure at some point between the two phases. Any insulating phase can be characterized by an invariant that determines its topological class; when the band gap closes along the adiabatic path separating topologically distinct phases, the topological invariant changes value, distinguishing the two insulating phases. The Chern insulator [155] and the QSH insulator are two examples of topological insulators, though they are characterized by different invariants.

In the bulk, spin-orbit coupling (SOC) is the mechanism for band gap opening in the QSH phase. Even though they are insulating in the bulk, as a consequence of their topological character, topological insulators possess metallic edge (in two dimensions) or surface (three dimensions) states. Hence, the QSH insulator is a highly unusual phase that is insulating in the bulk but metallic on the edges. Furthermore, the edge states are spin-filtered so that electrons with opposite spin propagate in opposite directions. There are myriad potential applications in electronics and spintronics for such an exotic material. However, because the SOC in graphene − the original QSH insulator − is so weak, it is easy for electronic excitations to thermalize above its intrinsic band gap. Such a small band gap, which is predicted to be on the order of only μeV [36], effectively transforms the material into a bulk metal at room temperature, eliminating its unusual electronic structure. In the past, researchers have focused on increasing the band gap by enhancing the intrinsic SOC of graphene by the adsorption of heavy adatoms [156, 157]. This method shows promise, but typically increases the band gap only to the $0.01 - 0.2$ eV range. These values are larger than k_{B}T, but increasing the band gap to the range of common bulk semiconductors ($\approx$1 eV) could further improve the performance of devices.

There are other routes to opening a band gap in graphene, however. Prior work has shown that periodic defects on graphene can induce intervalley scattering between inequivalent Dirac points and open a band gap without breaking A- and B-sublattice symmetry [13, 15, 103, 124]. The simplest such example is a periodic array of perforations on graphene, creating a graphene nanomesh (GNM). If the translation vectors of the GNM are written as linear combinations of graphene's primitive translation vectors, $\mathbf{R}_1 = n_1\mathbf{a}_1 + m_1\mathbf{a}_2$ and $\mathbf{R}_2 = n_2\mathbf{a}_1 + m_2\mathbf{a}_2$, the intervalley scattering condition is satisfied if $n_1 - m_1 = 3i$ and $n_2 - m_2 = 3j$ for some integers i and j. If the scattering preserves the proper symmetries of graphene, most importantly time reversal (TR) symmetry, it may be possible to realize a large band gap QSH phase in a GNM. Here we show that a QSH insulator with a giant band gap can exist in a GNM for arbitrarily weak values of SOC. We construct a GNM ribbon to demonstrate the metallic edge states and compute the Wannier charge centers in the bulk to demonstrate the Z_2 odd topological index.

6.2 Model

Our model is a slightly modified version of the familiar Kane-Mele TB Hamiltonian [34, 35].

$$H = \sum_i \epsilon_i c_i^\dagger c_i + \sum_{\langle ij \rangle} t_{ij} c_i^\dagger c_j + \sum_{\langle\langle ij \rangle\rangle} i\Lambda_{ij}^{\mathrm{SO}} v_{ij} c_i^\dagger s^z c_j \tag{6.1}$$

Here, all sums are performed over a supercell on a honeycomb lattice, which we will refer to as graphene. Inside the supercell, a single 6-C ring of atomic sites is replaced with a second type of atom, as shown in Figure 6.1. Previous *ab-initio* results have shown that a single 6-C ring defect is enough to open a substantial band gap in graphene [103, 124]. Now, the hopping parameter t_{ij} is a function of position in the supercell, with t_{ij} representing hopping between atom types i and j. Because there are two types of atoms, there are three distinct hopping parameters (t_{11}, t_{12}, and t_{22}). Similar arguments follow for the next-nearest neighbor SOC parameter $\Lambda_{ij}^{\mathrm{SO}}$ and on-site energies ϵ_i. s^z is a Pauli spin matrix and $v_{ij} = (2/\sqrt{3})(\hat{\mathbf{d}}_1 \times \hat{\mathbf{d}}_2)_z = \pm 1$ where $\hat{\mathbf{d}}_1$ and $\hat{\mathbf{d}}_2$ are unit vectors along the bonds traversed by the electron in hopping from site j to site i. By adjusting the six hopping parameters and two on-site energies, as well as the size and shape of the supercell, this system is described by a high dimensional, complicated phase diagram. We neglect the Rashba nearest neighbor hopping term and sublattice symmetry breaking λ_v term present in the original Kane-Mele model. In the original Kane-Mele model, these are not necessary to drive the system into a Z_2 odd phase, and their inclusion here does not qualitatively change the results. For numerical calculations, we use the PythonTB package provided by David Vanderbilt's group [158, 159].

6.3 Band gap opening

We start by examining the bulk band structures of several GNMs. In order to easily represent a GNM, we simply turn off the hopping from C to atom type two and from type two to type two, i.e. $t_{11} = 2.7$ and $t_{12} = t_{22} = 0$. Most GNMs have hole edges passivated by H, and we refer to atomic type two as H from now on. With all hopping to or from H turned off, their atomic states create flat bands that we move far away from the Fermi energy by setting their on-site energies high above the band gap. We consider two graphene supercells with different periodicities, one insulating and the other semimetallic. Their TB band structures based on Equation 6.1 without SOC are shown in Figure 6.1 e,f, as well as their comparison to a pristine graphene supercell (Figure 6.1 c,d). The 6×6 supercell satisfies the three fold rule on translation vectors for intervalley scattering and has a substantial band gap at the Γ point in Figure 6.1e. In contrast, the bands near the Fermi energy in the 7×7 supercell shown in Figure 6.1f are basically unchanged by the presence of the defect and are similar to the 7×7 supercell of pristine graphene. Despite the very simple approximation of turning off hopping to H atoms, the TB band structure in Figure 6.1e matches *ab-initio* density functional calculations of an insulating hydrogen passivated GNM very well [103, 124].

Including SOC for C ($\Lambda^{\mathrm{SO}}_{\mathrm{CC}} = 0.01$, $\Lambda^{\mathrm{SO}}_{\mathrm{CH}} = \Lambda^{\mathrm{SO}}_{\mathrm{HH}} = 0$) produces the band structures shown in Figure 6.1 g,h. For the 6×6 GNM, there is a slight splitting of previously degenerate bands at the VBM and CBM. The band gap is mostly unaffected though. In the case of the 7×7 supercell, SOC opens a small band gap at the position of the Dirac points. This small gap is the bulk band gap ordinarily seen in the QSH phase that has been studied in the past. With SOC turned on, we are now in the QSH regime of the original QSH phase diagram if

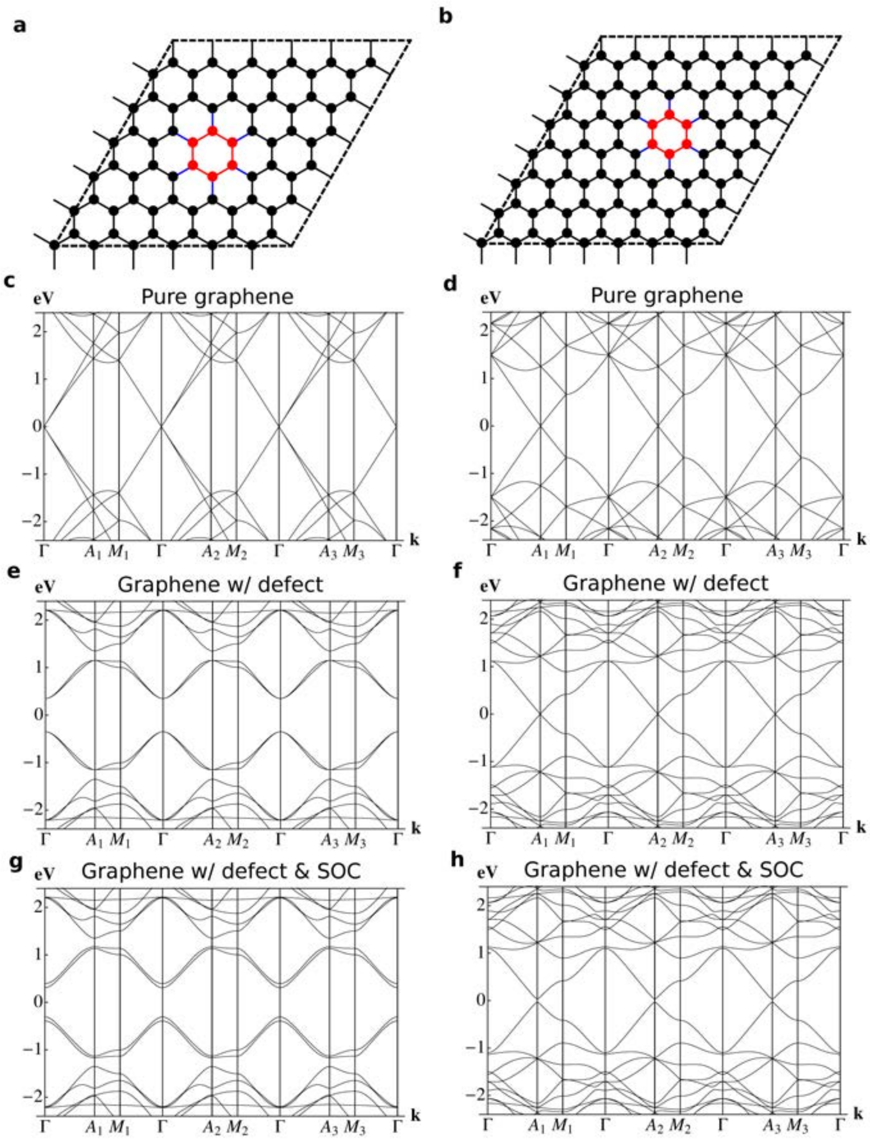

Figure 6.1: Bulk band structures with and without SOC. (a,b) Crystal structures of 6×6 and 7×7 graphene supercells subject to a single 6-C defect. In the (n_1, m_1, n_2, m_2) classifcation described in the text, these are $(6, 0, 0, 6)$ and $(7, 0, 0, 7)$ supercells, respectively. C atoms are represented by black dots while H is red. In our model, hopping along red and blue bonds is turned off. (c,d) Band structures of 6×6 and 7×7 graphene supercells without any defect, i.e. pure graphene. (e,f) Band structures of 6×6 and 7×7 GNMs with a single 6-C defect. (g,h) Band structures of 6×6 and 7×7 GNMs with a single 6-C defect and SOC for C.

there were no defect. Qualitatively, the phase diagram of our model GNM behaves similarly to the original QSH phase diagram, a point we will elaborate on by showing the existence of an actual QSH phase. To that end, we focus our attention on Figure 6.1g. Clearly, this crystal is an insulator, but the bulk band structure alone is not enough to determine if it is a QSH insulator.

6.4 Topological invariant

To determine the topological index of the 6×6 GNM, we place edges on the material to create a GNM ribbon. Figure 6.2a shows the geometry of the ribbon, with three defect sites and ribbon edges passivated by H. Again, hopping along red or blue bonds is set to zero. For comparison, we show the electronic structure of the same ribbon of pure graphene ($t_{\mathrm{CC}} = t_{\mathrm{CH}} = t_{\mathrm{HH}} = 2.7$). At the TB level, this graphene nanoribbon has gapless edge modes, as expected. The TB electronic structure of graphene nanoribbons has been studied extensively in the past [160–164]. When the defects are introduced, a large band gap appears as in Figure 6.2c, in agreement with the bulk band structure shown in Figure 6.1g. The flat edge modes present in the graphene nanoribbon still exist with defects in the nanoribbon. Importantly, these bands do not actually cross the Fermi energy.

Finally, we turn on SOC in the GNM ribbon (Figure 6.2d). Now, the edge states cross the Fermi energy, the hallmark of a QSH insulator. Importantly, the substantial bulk band gap is essentially unchanged by SOC and the crossing of edge bands. Each band crossing the Fermi energy is degenerate, with one copy for each edge. For a given edge, each spin propagates in only one direction, as shown in Figure 6.3. Despite the relative complexity of the GNM ribbon studied here, this behavior is identical to that of the original Kane-Mele model. Unlike the Kane-Mele model, the edge modes are now completely disconnected from the bulk bands by a subsantial energy gap. This comes as no surprise, since the bulk band gap is much larger than what would normally be induced by SOC alone. By increasing (decreasing) $\Lambda^{\mathrm{SO}}_{\mathrm{CC}}$, it is possible to increase (decrease) the band width of the edge states. The crossing of the edge states in the GNM ribbon persists for arbitrarily weak values of $\Lambda^{\mathrm{SO}}_{\mathrm{CC}}$, suggesting that the intrinsic SOC of C would be enough to form a giant band gap QSH phase in a GNM. Because we do not rely on weak SOC to open the bulk band gap, electronic excitations would not be able to thermalize across the bulk band gap in a GNM.

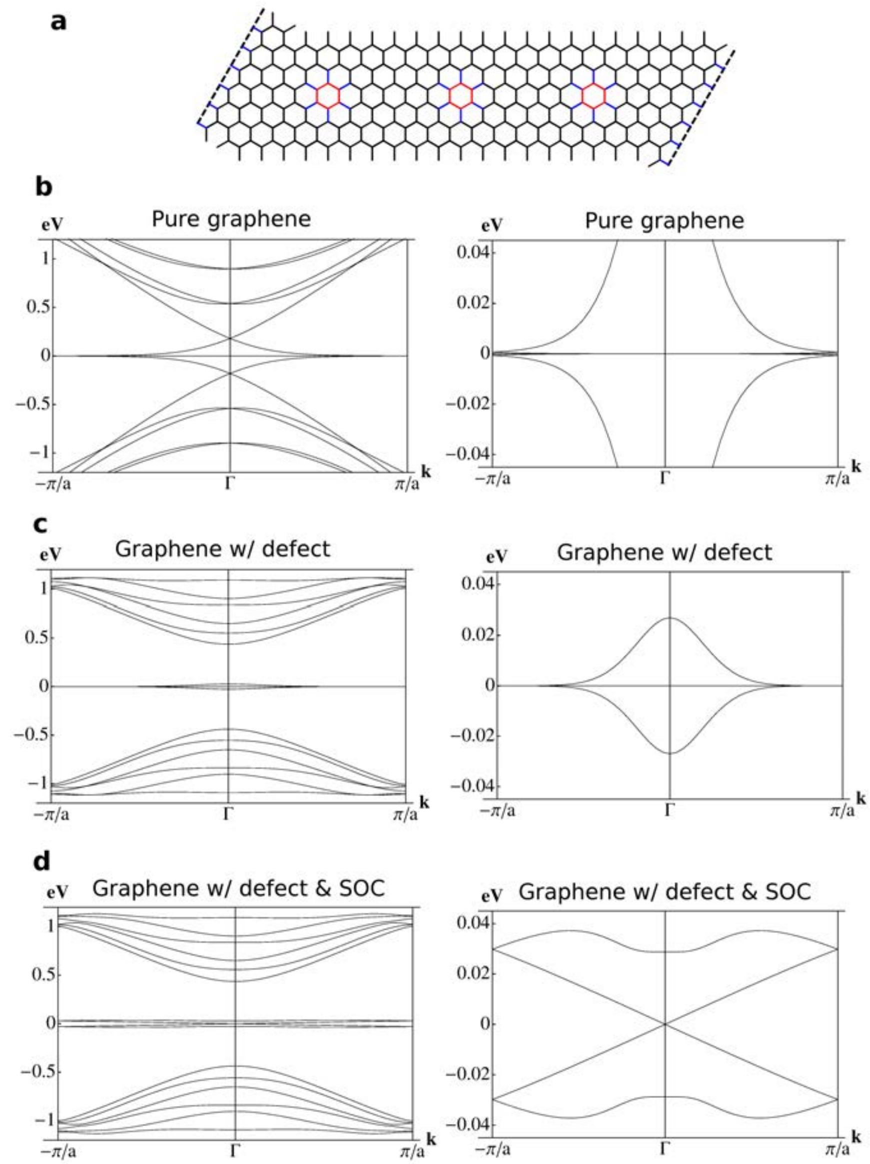

Figure 6.2: Ribbon band structures with and without SOC. (a) Crystal structure of a ribbon constructed from a 6×6 GNM. Dashed lines indicate the periodic direction. Band structures for a ribbon of (a) pure graphene, (b) GNM, (c) and GNM with SOC.

Figure 6.3 shows the TB wave functions for edge modes of the GNM ribbon. On the left edge, the orange band (spin 1) increases in energy from the $-\mathbf{k}$ direction to $+\mathbf{k}$, while the green band (spin 2) propagates in the opposite direction. A degenerate pair of bands exists on the right edge (not shown), except with the opposite direction of propagation for each spin. These are the characteristic spin-filtered edge states of the QSH insulator. These

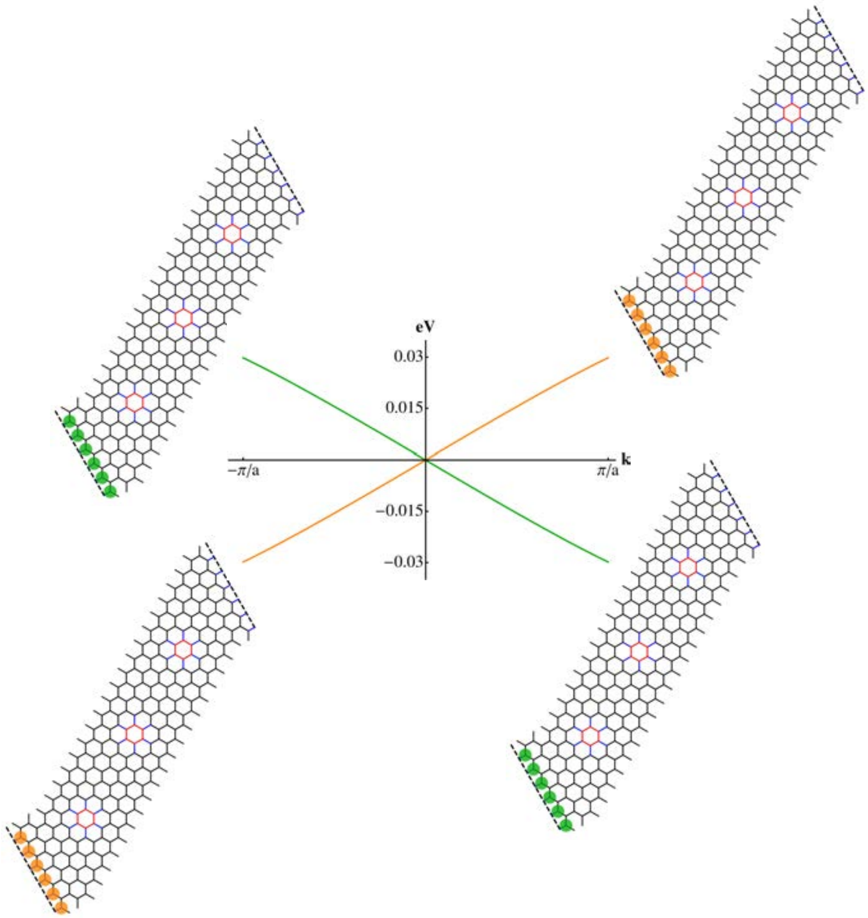

Figure 6.3: Spin-filtered edge states. Orange and green correspond to opposite spins, with each spin propagating in opposite directions. The area of orange and green circles represent the probability of finding an electron on that atomic site for TB wave functions at $\mathbf{k} = -0.15\pi/a$ (left) and $\mathbf{k} = 0.15\pi/a$ (right) in the orange and green bands, respectively.

bands become perfectly flat when SOC is turned off, as in Figure 6.2b,c. There are additional pairs of edge bands near ± 0.03 eV in Figure 6.2d. These extra bands do not touch the Fermi energy, but they are close enough in energy to the crossing bands that charge carriers could occupy these states. If these extra bands are ordinary, i.e. not spin-filtered, they could ruin the spin-filtered metallic edge states of the ribbon. Fortunately, these extra bands are extensions of the crossing bands that are simply folded back into the small 1D Brillouin zone of the ribbon. After unfolding these edge bands and examining their wave functions, it is obvious that the bands at ± 0.03 eV belong to the same spin-filtered bands of edge states that cross the Fermi energy.

It is also possible to characterize a QSH phase in the bulk without placing edges on the ribbon. The topological invariant of a QSH insulator is the Z_2 index, which is only defined modulo 2 and hence leads to two phases, even or odd [35]. The even phase is a trivial insulator, and the odd phase is a QSH insulator. In two dimensions, there is a single Z_2 invariant that can be determined in the bulk, i.e. with periodic boundary conditions in both directions. The Z_2 index is only defined when time-reversal (TR) symmetry is preserved, causing occupied states at $\mathbf{k}$ and $-\mathbf{k}$ to form Kramers pairs. Without presenting a microscopic description for the scattering mechanism in our model GNM, we assume that TR symmetry is preserved and proceed with the calculation of the Z_2 invariant. The calculated band structures suggest that this is the case, with degenerate states for all occupied $\mathbf{k}$ and $-\mathbf{k}$.

Instead of simply reporting the Z_2 invariant of the 6×6 GNM with SOC, we present the positions of Wannier charge centers ($\bar{x}$) for a set of fictitious 1D systems sampled along the k_y direction [158, 159]. The connectivity of these charge center bands provides a visual determination of the Z_2 index. If a degenerate pair at $k_y = 0$ is also degenerate at $k_y = \pi/a$ after tracking their charge centers across the 1D BZ, the Z_2 index is even. An example of the even phase is if $\bar{x}$ is unchanged as a function of k_y and the charge center bands are flat. If, however, a degenerate pair at $k_y = 0$ trades one of its partners with a member of a different degenerate pair at π/a, the Z_2 index is odd and the system is in the QSH phase. The charge centers of the Z_2 odd phase must change position as a function of k_y in order for degenerate pairs at $k_y = 0$ to trade members at $k_y = \pi/a$. In the Z_2 odd phase, the charge center bands are analogous to dispersive electronic bands, in contrast to the flat bands of the Z_2 even phase.

Figure 6.4 shows the evolution of Wannier charge centers for a set of fictitious 1D systems at several values of k_y in our model GNM with SOC. To exaggerate the connectivity features of the charge centers, the SOC is increased to $\Lambda^{\mathrm{SO}}_{\mathrm{CC}} = 0.1$. Because there are so many occupied

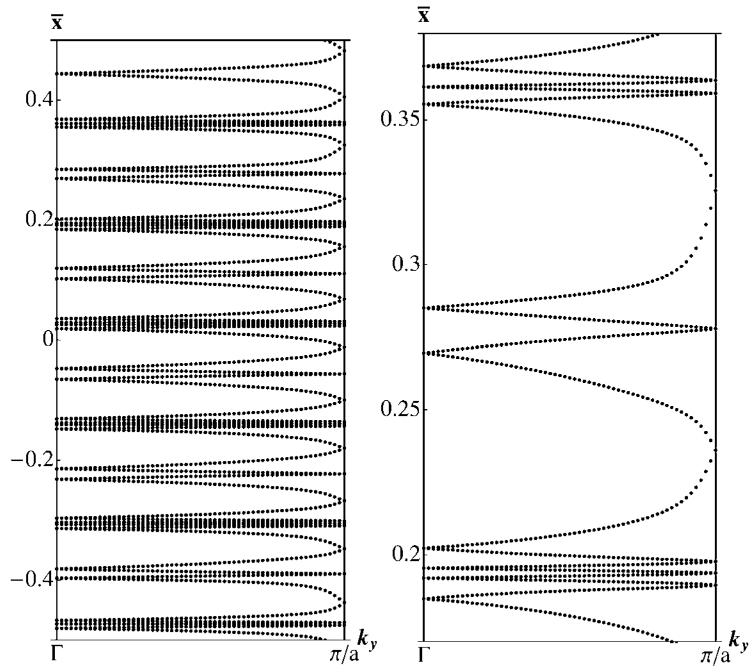

Figure 6.4: Evolution of Wannier charge centers. The 2D BZ of the 6×6 GNM is divided into 61 different 1D systems along k_y. The reduced coordinate of the centers of Wannier functions for all occupied bands are plotted as a function of k_y. Flat bands coming from non-dispersive atomic H states are treated as unoccupied.

bands, the connectivity of the charge centers requires a dense sampling of k_y and is difficult to analyze all at once. The right side of Figure 6.4 shows a close-up of the bands where the connectivity is more obvious. Tracking the charge center bands from left to right, any degenerate pair at $k_y = 0$ loses one of its partners at $k_y = \pi/a$ to the next highest (lowest) degenerate pair above (below) it. This trading of degenerate pairs is the signature of a Z_2 odd phase and is further evidence for a QSH phase in a GNM.

6.5 Discussion

The major obstacle to fabricating QSH devices made of graphene is its small intrinsic band gap. Previous efforts aimed at increasing the bulk band gap of QSH insulators have studied enhancing SOC by the adsorption of heavy adatoms [156, 157]. While this method can produce band gaps larger than k_BT at room temperature, *ab-initio* calculations of GNMs report band gaps of 1 eV and even higher, depending on the size of the hole and supercell.

These large band gaps are comparable to the values in conventional semiconductors and could improve the on-off switching characteristics of devices. We are currently investigating the *ab-initio GW* quasiparticle electronic structure and excitonic effects in bulk GNMs.

Mapping the complex phase diagram of the QSH phase in a GNM may be the next step in realizing a giant band gap QSH phase. There are several parameters defining the phase diagram, however: three different nearest neighbor hopping parameters, three values of SOC, two different on-site energies, the size and shape of the supercell, and the possible inclusion of Rashba terms. Qualitatively, our results show that the phase diagram behaves similarly to that of the original Kane-Mele model. Even at the TB level, such a complete mapping represents a considerable effort. Because of the intrinsically large size of GNMs, such calculations at the *ab-initio* level may be limited.

In fact, *ab-initio* calculations of the QSH phase in a GNM present significant numerical and physical challenges. The 6×6 GNM described here has 72 atoms; a fully relativistic, non-collinear treatment of SOC for such a large system will be numerically difficult, though not impossible. Additionally, electron-electron interactions on the edges of a GNM ribbon may break the required TR symmetry and ruin the QSH phase. In a graphene nanoribbon, for example, ferromagnetic ordering exists along each edge but anti-ferromagnetic ordering exists between different edges [69, 165, 166]. For this reason, it is advisable to focus on computing the Z_2 index of a GNM in the bulk rather than the ribbon geometry. The effect of intervalley scattering on TR symmetry in real materials may also present a challenge to the existence of a QSH phase. Without a detailed microscopic model of the scattering mechanism involved in the real material, it is difficult to predict if TR symmetry will be preserved. Using different defect structures, like dopants or adsorbed atoms instead of C vacancies, offers some tunability of the scattering mechanism and its effect on TR symmetry. Certainly, the real scattering will be more complex than the idealized case considered here.

We have presented a new method to form a giant band gap (> 1 eV) QSH insulator in graphene. Instead of increasing the bulk band gap by enhancing the intrinsic SOC of graphene, we open a bulk band gap by patterning periodic defects to induce intervalley scattering between Dirac points. In a ribbon geometry and for arbitrarily weak SOC, spin-filtered edge states cross the Fermi energy to indicate the existence of a QSH phase. By adjusting the value of SOC, the band width of the edge modes can be made arbitrarily wide and the gap between edge and bulk bands can be reduced. Additionally, the connectivity of Wannier charge centers clearly demonstrate the Z_2 odd topological index of the GNM. Therefore, a giant band gap QSH phase can exist in a GNM with only the intrinsic SOC of graphene.

6.6 Acknowledgments

This work was supported by U.S. DOE Early Career Award (Grant No. DE-SC0006433). The authors thank M. Lusk and D. Wood for insightful discussions.

CHAPTER 7
CONCLUSION

In this dissertation, we have advanced the understanding of the effects of structural defects on electronic and optical properties of graphene. Most previous studies in this area were numerical calculations on certain specific defected graphene structures, offering some empirical rules and trends but lacking fundamental understanding and the corresponding relationship between defect distribution and electronic structure. In contrast, our systematic study provides an analytic understanding on the physics involved. The geometric condition for scattering between Dirac points is similar to the nearly free electron model in solid-state physics, where an external potential opens a band gap at the BZ boundaries. Our general methodology is applicable to band structure engineering any material by application of defects; find geometric conditions on the supercell so that scattering between states near the Fermi energy is allowed. Obviously, the three-fold rule discovered here is specific to graphene. If the defect is a strong enough perturbation, a splitting of degenerate states should occur and a band gap would open. In our particular case, graphene is transformed from a semimetal to a semiconductor because the valence and conduction bands touch only at the Dirac points without overlapping. In a real metal, there could be significant overlap between valence and conduction bands, and structural defects might not actually open a band gap. Defect engineering may still be useful to modify other aspects of the electronic structure, however, like effective masses or band widths.

In addition to defect periodicity and size, characterizing defected graphene also requires knowledge of the defect shape. We have shown that a complete understanding of defects on graphene only comes with considering the defect geometry. While the movement of Dirac points is physically interesting by itself, anisotropic defects might also be useful to tune transport properties in graphene. Semiconducting graphene sheets with anistropic defects show different effective masses in different directions. By controlling the defect shape, it may be possible to reduce electrical transport in any particular direction. Thermal transport will certainly be affected by the presence of structural defects. An open question, in general, is the effect of defects on the phonon spectrum of graphene and how defects affect thermal transport.

Topological band theory is a new and rapidly evolving field. There is already a significant amount of theoretical research aimed at discovering new topological insulators in two and three dimensions. In two dimensions, most of the prior work has focused on enhancing the intrinsic spin-orbit coupling of graphene to increase the bulk band gap. Our work shows that this is not the only route to enhancing the band gap. It is somewhat surprising and unexpected that the QSH phase persists even with structural defects in the lattice. Our discovery could start a new branch of topological insulator research based on enhancing the bulk band gap by methods beyond the standard models of topological insulators, mainly the Kane-Mele model. Such complex systems may be difficult to model analytically. Luckily, tight-binding calculations are efficient and accurate for C based systems.

There is a significant amount of future research that could be performed based only on our discovery of a QSH phase in a GNM. It seems likely that any semiconducting GNM could support a QSH phase, but this must be verified explicitly. To make the predictions as realistic as possible, the structures also need to include the effects of lattice dilation, buckling caused by defects, and small but non-zero hopping to and from the defect atoms. Eventually, predictions of the QSH phase need to go beyond tight-binding as well. Density functional calculations on such large systems are difficult but not impossible. To most closely match experiment, the spin-orbit coupling should be treated with fully relativistic, non-collinear calculations. In the ribbon geometry, electron-electron interactions on the edges of graphene nanoribbons can induce ferromagnetic ordering along edges that break time reversal symmetry. Luckily, one can circumvent this issue by performing calculations in the bulk based on the Wannier charge centers to determine the topological index of the material. Numerical packages do exist that take the output from density functional codes and compute the Wannier charge centers and Z_2 index.

Structurally modified graphene sheets offer highly tunable electronic and optical properties, making them attractive candidates for optoelectronic devices. Quantum dots present a similar level of customization, as their band gap can be increased due to quantum confinement by decreasing the dot size. Research into quantum dot based photovoltaics and optoelectronics has developed into an expansive field. One drawback of using quantum dots, however, is that they cannot carry current unless they are formed into a chain or embedded into a matrix. Defected graphene is periodic in two directions, meaning its observed electrical and transport properties will not be altered by any material that it is embedded in. Practically speaking, however, graphene will always exist on a substrate in any kind of device. Even so, transport can happen within the graphene layer, not through the surrounding material. 1D nanostructured materials, such as carbon nanotubes or silicon nanowires, also present some level of tunability by varying their diameter.

As general as our modeling and calculations are, there are still certain defect configurations that we do not consider. All of our structures have perfect translational symmetry, which may not match the laboratory made materials perfectly. Experimentalists do not have perfect, atomic scale precision to pattern defects, and grain boundaries in the initial graphene sheet or substrate can also break translational symmetry. Unfortunately, a sheet of graphene without translational symmetry is essentially a giant molecule, making it numerically intractable. Another limitation of our research is that we only consider defects that preserve the honeycomb lattice of graphene. Hexagonal BN has the same crystal structure as graphene, passivating H atoms are all paired exactly with one C atom, and hole edges in GNMs are not allowed to reconstruct. Except for local lattice dilation and atomic relaxation, we do not allow the material to deviate from its honeycomb structure, e.g. we do not allow any heptagonal or pentagonal rings on graphene. Irregular defect boundaries can be described by our VCA description of the anisotropic honeycomb lattice, but this picture likely breaks down once the underlying honeycomb lattice is destroyed.

One major topic of potential future work is transport calculations. Pristine graphene has very high charge carrier mobility, but the effect of structural defects on mobility remains somewhat unknown. There have been tight-binding studies of transport in defected graphene in the past, but, as with initial research on their electronic structure, there is not careful attention to the periodicity of the defects. At the very least, one should separate transport calculations for semimetals from semiconductors. Future work could also include the energetic stability of structural defects. Our work is general enough that it should accommodate most defects, but research on their energetics could help experimentalists focus their efforts on stable materials. It could also be interesting to study bilayer GNMs. Bilayer graphene is also a semimetal, making it useless for semiconductor devices. The role of defects in bilayer graphene is yet to be discovered. Layered structures could be particularly useful for multilayered photovoltaic absorbers since individual layers of defected graphene have such sharp absorption peaks.

APPENDIX - CO-AUTHOR AND PUBLISHER PERMISSIONS

Figure A.1 shows the permission from the publisher to reproduce the material in Chapter 2.

License agreement and author copyright

Scientific Reports does not require authors to assign copyright of their published original research papers to the journal. Articles are published under a CC BY license (Creative Commons Attribution 4.0 International License). The CC BY license allows for maximum dissemination and re-use of open access materials and is preferred by many research funding bodies. Under this license users are free to share (copy, distribute and transmit) and remix (adapt) the contribution including for commercial purposes, providing they attribute the contribution in the manner specified by the author or licensor (read full legal code).

The CC BY-NC-ND and CC BY-NC-SA licenses are available on request: authors should contact the editorial office (scientificreports@nature.com) on acceptance of an article to discuss these options.

Creative Commons

Creative Commons License Deed

Attribution 4.0 International (CC BY 4.0)

This is a human-readable summary of (and not a substitute for) the license.
Disclaimer

Free Cultural Works APPROVED FOR

You are free to:

Share — copy and redistribute the material in any medium or format

Adapt — remix, transform, and build upon the material

for any purpose, even commercially.

The licensor cannot revoke these freedoms as long as you follow the license terms.

Under the following terms:

Attribution — You must give appropriate credit, provide a link to the license, and indicate if changes were made. You may do so in any reasonable manner, but not in any way that suggests the licensor endorses you or your use.

No additional restrictions — You may not apply legal terms or technological measures that legally restrict others from doing anything the license permits.

Figure A.1: Reproduction permission from Scientific Reports.

Figure A.2 shows the permission from the publisher to reproduce the material in Chapters 3 and 5.

As the author of an APS-published article, may I use figures, tables, graphs, etc. in future publications?

Yes, as the author you have the right to use figures, tables, graphs, etc. in subsequent publications using files prepared and formatted by you or the APS-prepared versions. The appropriate bibliographic citation must be included.

As the author of an APS-published article, may I include my article or a portion of my article in my thesis or dissertation?

Yes, the author has the right to use the article or a portion of the article in a thesis or dissertation without requesting permission from APS, provided the bibliographic citation and the APS copyright credit line are given on the appropriate pages.

As the author of an APS-published article, may I give permission to a colleague or third party to republish all or part of the article in a print publication?

Yes, as the author you may grant permission to third parties to republish print versions of the article provided the APS-published version (e.g., the PDF from the online journal, or a copy of the article from the print journal) is not used for this purpose. The article may not be published in another journal, and the third party may not charge a fee. The appropriate bibliographic citation and notice of the APS copyright must be included.

As the author of an APS-published article, may I give permission to a colleague or third party to republish all or part of the APS-published version in an online journal, book, database compilation, etc.?

No, an author may not grant permission in this case. To request permission to republish APS-copyrighted material, please refer to the “Reprints & Permissions” link that can be found on each APS article page.

Figure A.2: Reproduction permission from the American Physical Society.

Figure A.3 shows the permission from the publisher to reproduce the material in Chapter 4.

Acknowledgements to be used by RSC authors

Authors of RSC books and journal articles can reproduce material (for example a figure) from the RSC publication in a non-RSC publication, including theses, without formally requesting permission providing that the correct acknowledgement is given to the RSC publication. This permission extends to reproduction of large portions of text or the whole article or book chapter when being reproduced in a thesis.

The acknowledgement to be used depends on the RSC publication in which the material was published and the form of the acknowledgements is as follows:

- For material being reproduced from an article in *New Journal of Chemistry* the acknowledgement should be in the form:
  - [Original citation] - Reproduced by permission of The Royal Society of Chemistry (RSC) on behalf of the Centre National de la Recherche Scientifique (CNRS) and the RSC
- For material being reproduced from an article *Photochemical & Photobiological Sciences* the acknowledgement should be in the form:
  - [Original citation] - Reproduced by permission of The Royal Society of Chemistry (RSC) on behalf of the European Society for Photobiology, the European Photochemistry Association, and RSC
- For material being reproduced from an article in *Physical Chemistry Chemical Physics* the acknowledgement should be in the form:
  - [Original citation] - Reproduced by permission of the PCCP Owner Societies
- For material reproduced from books and any other journal the acknowledgement should be in the form:
  - [Original citation] - Reproduced by permission of The Royal Society of Chemistry

The acknowledgement should also include a hyperlink to the article on the RSC website.

The form of the acknowledgement is also specified in the RSC agreement/licence signed by the corresponding author.

Except in cases of republication in a thesis, this express permission does not cover the reproduction of large portions of text from the RSC publication or reproduction of the whole article or book chapter.

A publisher of a non-RSC publication can use this document as proof that permission is granted to use the material in the non-RSC publication.

Figure A.3: Reproduction permission from The Royal Society of Chemistry.

Figure A.4 shows co-author permission to reproduce the material in Chapter 2.

Marc Dvorak <marc.dvorak@gmail.com>

Dissertation

William Oswald <billevos@gmail.com> Sun, Mar 29, 2015 at 6:45 PM
To: Marc Dvorak <mdvorak@mines.edu>, Zhigang Wu <zhiwu@mines.edu>

Marc,

I'm glad to hear you're finishing your dissertation! I'm happy to consent - You have my permission to include the paper titled "Bandgap Opening by Patterning Graphene" in your dissertation. Good luck!

Respectfully,
Signed: William Oswald

On Fri, Mar 27, 2015 at 2:05 PM, Marc Dvorak <mdvorak@mines.edu> wrote:

> Hi Billy,
> I'm finishing up my dissertation now, and I need your permission to include our Scientific Reports paper as a chapter. Do I have your permission to include this paper in my dissertation?
>
> http://www.nature.com/srep/2013/130726/srep02289/full/srep02289.html
>
> Thanks,
> Marc

Figure A.4: Reproduction permission from co-author William Oswald.

REFERENCES CITED

[1] A. K. Geim and K. S. Novoselov. The rise of graphene. *Nature Mat.*, 6(3):183–191, 2007.

[2] Lewis Gomez De Arco, Yi Zhang, Cody W. Schlenker, Koungmin Ryu, Mark E. Thompson, and Chongwu Zhou. Continuous, highly flexible, and transparent graphene films by chemical vapor deposition for organic photovoltaics. *ACS Nano*, 4(5):2865–2873, 2010.

[3] Rachel Won. Photovoltaics: graphene-silicon solar cells. *Nature Phot.*, 4(7):411, 2010.

[4] Vinay Gupta, Neeraj Chaudhary, Ritu Srivastava, Gauri Datt Sharma, Ramil Bhardwaj, and Suresh Chand. Luminscent graphene quantum dots for organic photovoltaic devices. *Jour. of the ACS*, 133(26):9960–9963, 2011.

[5] Virginia Yong and James M. Tour. Theoretical efficiency of nanostructured graphene-based photovoltaics. *Small*, 6(2):313–318, 2010.

[6] Jingwei Bai, Xing Zhong, Shan Jiang, Yu Huan, and Xiangfeng Duan. Graphene nanomesh. *Nat. Nano.*, 5(3):190–194, 2010.

[7] Rui Cheng, Jingwei Bai, Lei Liao, Hailong Zhou, Yu Chen, Lixin Liu, Yung-Chen Lin, Shan Jiang, Yu Huang, and Xiangfeng Duan. High-frequency self-aligned graphene transistors with transferred gate stacks. *Proceed. of Nat. Acad. of Sci.*, 2012.

[8] L. Britnell, R. V. Gorbachev, R. Jalil, B. D. Belle, F. Schedin, A. Mishchenko, T. Georgiou, M. I. Katsnelson, L. Eaves, S. V. Morozov, N. M. R. Peres, J. Leist, A. K. Geim, K. S. Novoselov, and L. A. Ponomarenko. Field-effect tunneling transistor based on vertical graphene heterostructures. *Science*, 335(6071):947–950, 2012.

[9] Yanqing Wu, Yu-ming Lin, Ageeth A. Bol, Keith A. Jenkins, Fengnian Xia, Damon B. Farmer, Yu Zhu, and Phaedon Avouris. High-frequency, scaled graphene transistors on diamond-like carbon. *Nature*, 472(7341):74–78, 2011.

[10] William Oswald and Zhigang Wu. Energy gaps in graphene nanomeshes. *Phys. Rev. B*, 85:115431, 2012.

[11] H. Şahin and S. Ciraci. Structural, mechanical, and electronic properties of defect-patterned graphene nanomeshes from first principles. *Phys. Rev. B*, 84:035452, 2011.

[12] Thomas G. Pedersen, Christian Flindt, Jesper Pedersen, Niels Asger Mortensen, Antti-Pekka Jauho, and Kjeld Pedersen. Graphene antidot lattices: Designed defects and spin qubits. *Phys. Rev. Lett.*, 100:136804, 2008.

[13] Wei Liu, Z. F. Wang, Q. W. Shi, Jinlong Yang, and Feng Liu. Band-gap scaling of graphene nanohole superlattices. *Phys. Rev. B*, 80:233405, 2009.

[14] X. Y. Cui, R. K. Zheng, Z. W. Liu, L. Li, B. Delley, C. Stampfl, and S. P. Ringer. Magic numbers of nanoholes in graphene: Tunable magnetism and semiconductivity. *Phys. Rev. B*, 84:125410, 2011.

[15] Fangping Ouyang, Shenglin Peng, Zhongfan Liu, and Zhirong Liu. Bandgap opening in graphene antidot lattices: The missing half. *ACS Nano*, 5(5):4023–4030, 2011.

[16] J A Frst, J G Pedersen, C Flindt, N A Mortensen, M Brandbyge, T G Pedersen, and A-P Jauho. Electronic properties of graphene antidot lattices. *New Journal of Physics*, 11(9):095020.

[17] A. Baskin and P. Kral. Electronic structures of porous nanocarbons. *Sci. Rep.*, 1:36, 2011.

[18] Ren Petersen, Thomas Garm Pedersen, and Antti-Pekka Jauho. Clar sextet analysis of triangular, rectangular, and honeycomb graphene antidot lattices. *ACS Nano*, 5(1): 523–529, 2011.

[19] Ji Feng, Wenbin Li, Xiaofeng Qian, Jingshan Qi, Liang Qi, and Ju Li. Patterning of graphene. *Nanoscale*, 4:4883–4899, 2012.

[20] Mark T. Lusk and L. D. Carr. Nanoengineering defect structures on graphene. *Phys. Rev. Lett.*, 100:175503.

[21] Mark T. Lusk, David T. Wu, and Lincoln D. Carr. Graphene nanoengineering and the inverse Stone-Thrower-Wales defect. *Phys. Rev. B*, 81:155444, 2010.

[22] David J. Appelhans, Zhibin Lin, and Mark T. Lusk. Two-dimensional carbon semiconductor: Density functional theory calculations. *Phys. Rev. B*, 82:073410, 2010.

[23] David J. Appelhans, Lincoln D. Carr, and Mark T. Lusk. Embedded ribbons of graphene allotropes: an extended defect perspective. *New J. Phys.*, 12:125006, 2010.

[24] Lincoln D. Carr and Mark T. Lusk. Defect engineering: Graphene gets designer defects. *Nat. Nano.*, 5:316–317, 2010.

[25] Xiaofeng Fan, Zexiang Shen, A. Q. Liu, and Jer-Lai Kuo. Band gap opening of graphene by doping small boron nitride domains. *Nanoscale*, 4:2157–2165, 2012.

[26] Lijie Ci, Li Song, Chuanhong Jin, Deep Jariwala, Dangxin Wu, Yongjie Li, Anchal Srivastava, Z. F. Wang, Kevin Storr, Luisa Balicas, Feng Liu, and Pulickel M. Ajayan. Atomic layers of hybridized boron nitride and graphene domains. *Nature Mater.*, 9: 430–435, 2010.

[27] Michael Rohlfing and Steven G. Louie. Electron-hole excitations in semiconductors and insulators. *Phys. Rev. Lett.*, 81:2312–2315, 1998.

[28] Michael Rohlfing and Steven G. Louie. Electron-hole excitations and optical spectra from first principles. *Phys. Rev. B*, 62:4927–4944, 2000.

[29] Stefan Albrecht, Giovanni Onida, and Lucia Reining. Ab-initio calculation of the quasiparticle spectrum and excitonic effects in li_2o. *Phys. Rev. B*, 55:10278–10281, 1997.

[30] Robert Laskowski, Niels Egede Christensen, Gilles Santi, and Claudia Ambrosch-Draxl. *Ab-initio* calculations of excitons in GaN. *Phys. Rev. B*, 72:035204, 2005.

[31] Robert Laskowski and Niels Egede Christensen. *Ab-initio* calculation of excitons in ZnO. *Phys. Rev. B*, 73:045201, 2006.

[32] Andrea Marini and Rodolfo Del Sole. Dynamical excitonic effects in metals and semiconductors. *Phys. Rev. Lett.*, 91:176402, 2003.

[33] Lorin X. Benedict, Eric L. Shirley, and Robert B. Bohn. Optical absorption of insulators and the electron-hole interaction: An *Ab-initio* calculation. *Phys. Rev. Lett.*, 80: 4514–4517, 1998.

[34] C. L. Kane and E. J. Mele. Quantum spin hall effect in graphene. *Phys. Rev. Lett.*, 95:226801, Nov 2005.

[35] C. L. Kane and E. J. Mele. Z_2 topological order and the quantum spin hall effect. *Phys. Rev. Lett.*, 95:146802, Sep 2005.

[36] M. Gmitra, S. Konschuch, C. Ertler, C. Ambrosch-Draxl, and J. Fabian. Band-structure topologies of graphene: Spin-orbit coupling effects from first principles. *Phys. Rev. B*, 80:235431, Dec 2009.

[37] G. K. Webb. Predicting processor performance. *Issues in Inform. Sys.*, 5, 2004.

[38] P. Gepner and M. F. Kowalik. Multi-core processors: new way to achieve high system performance. *Proc. of the Intl. Symp. on Parall. Comput. in Elec. Eng.*, 2006.

[39] H. Esmaeilzadeh, E. Blem, R. St. Amant, K. Sankaralingam, and D. Burger. Dark silicon and the end of multicore scaling. *Proc. of the 38th Intl. Symp. on Comput. Arch.*, 2011.

[40] Nathan S. Lewis. Toward cost-effective solar energy use. *Science*, 315(5813):798–801, 2007.

[41] Cyrus Wadia, A. Paul Alivisatos, and Daniel M. Kammen. Materials availability expands the opportunity for large-scale photovoltaics deployment. *Environ. Sci. Tech.*, 43(6):2072–2077, 2009.

[42] Zhibin Lin, Huashan Li, Alberto Franceschetti, and Mark T. Lusk. Efficient exciton transport between strongly quantum-confined silicon quantum dots. *ACS Nano*, 6(5): 4029–4038, 2012.

[43] Wendy U. Huynh, Janke J. Dittmer, and A. Paul Alivisatos. Hybrid nanorod-polymer solar cells. *Science*, 295(5564):2425–2427, 2002.

[44] Kevin M. Coakley, Yuxiang Liu, Chiatzun Goh, and Michael D. McGehee. Ordered organicinorganic bulk heterojunction photovoltaic cells. *MRS Bulletin*, 30:37–40, 0 2005.

[45] A. H. Castro Neto, F. Guinea, N. M. R. Peres, K. S. Novoselov, and A. K. Geim. The electronic properties of graphene. *Rev. Mod. Phys.*, 81:109–162, 2009.

[46] Igor A. Luk'yanchuk and Yakov Kopelevich. Dirac and normal fermions in graphite and graphene: Implications of the quantum hall effect. *Phys. Rev. Lett.*, 97:256801, 2006.

[47] Catalin D. Spataru, Sohrab Ismail-Beigi, Lorin X. Benedict, and Steven G. Louie. Excitonic effects and optical spectra of single-walled carbon nanotubes. *Phys. Rev. Lett.*, 92:077402, 2004.

[48] C.D. Spataru, S. Ismail-Beigi, L.X. Benedict, and S.G. Louie. Quasiparticle energies, excitonic effects and optical absorption spectra of small-diameter single-walled carbon nanotubes. *Appl. Phys. A*, 78:1129–1136, 2004.

[49] Zhiyuan Zeng, Xiao Huang, Zongyou Yin, Hong Li, Yang Chen, Hai Li, Qing Zhang, Jan Ma, Freddy Boey, and Hua Zhang. Fabrication of graphene nanomesh by using an anodic aluminum oxide membrane as a template. *Adv. Mats.*, 24(30):4138–4142, 2012.

[50] Alexander Sinitskii and James M. Tour. Patterning graphene through the self-assembled templates: Toward periodic two-dimensional graphene nanostructures with semiconductor properties. *Jour. of the ACS*, 132(42):14730–14732, 2010.

[51] Omid Akhavan. Graphene nanomesh by ZnO nanorod photocatalysts. *ACS Nano*, 4 (7):4174–4180, 2010.

[52] W. A. Harrison. *Electronic structure and the properties of solids.* W. H. Freeman, 1980.

[53] P. Hohenberg and W. Kohn. Inhomogeneous electron gas. *Phys. Rev.*, 136:B864–B871, 1964.

[54] W. Kohn and L. J. Sham. Self-consistent equations including exchange and correlation effects. *Phys. Rev.*, 140:A1133–A1138, 1965.

[55] John P. Perdew and Yue Wang. Accurate and simple analytic representation of the electron-gas correlation energy. *Phys. Rev. B*, 45:13244–13249, 1992.

[56] John P. Perdew, Kieron Burke, and Matthias Ernzerhof. Generalized gradient approximation made simple. *Phys. Rev. Lett.*, 77:3865–3868, 1996.

[57] A. L. Fetter and J. D Walecka. *Quantum theory of many-particle systems.* McGraw-Hill, 1971.

[58] Giovanni Onida, Lucia Reining, and Angel Rubio. Electronic excitations: density-functional versus many-body green's-function approaches. *Rev. Mod. Phys.*, 74:601–659, 2002.

[59] Lars Hedin. New method for calculating the one-particle green's function with application to the electron-gas problem. *Phys. Rev.*, 139:A796–A823, 1965.

[60] Mark S. Hybertsen and Steven G. Louie. Electron correlation in semiconductors and insulators: Band gaps and quasiparticle energies. *Phys. Rev. B*, 34:5390–5413, 1986.

[61] Mark S. Hybertsen and Steven G. Louie. First-principles theory of quasiparticles: Calculation of band gaps in semiconductors and insulators. *Phys. Rev. Lett.*, 55:1418–1421, 1985.

[62] Jack Deslippe, Georgy Samsonidze, David A. Strubbe, Manish Jain, Marvin L. Cohen, and Steven G. Louie. Berkeleygw: A massively parallel computer package for the calculation of the quasiparticle and optical properties of materials and nanostructures. *Comp. Phys. Comm.*, 183(6):1269 – 1289, 2012.

[63] E. E. Salpeter and H. A. Bethe. A relativistic equation for bound-state problems. *Phys. Rev.*, 84:1232–1242, 1951.

[64] Giovanni Bussi. Effects of the electronhole interaction on the optical properties of materials: the bethesalpeter equation. *Physica Scripta*, 2004(T109):141, 2004.

[65] Marc Dvorak, Su-Huai Wei, and Zhigang Wu. Origin of the variation of exciton binding energy in semiconductors. *Phys. Rev. Lett.*, 110:016402, 2013.

[66] F. Schwierz. Graphene transistors. *Nat. Nano.*, 5:487–496, 2010.

[67] K. S. Novoselov, A. K. Geim, S. V. Morozov, D. Jiang, M. I. Katsnelson, I. V. Grigorieva, S. V. Dubonos, and A. A. Firsov. Two-dimensional gas of massless dirac fermions in graphene. *Nature*, 438:197–200, 2005.

[68] Alexander S. Mayorov, Roman V. Gorbachev, Sergey V. Morozov, Liam Britnell, Rashid Jalil, Leonid A. Ponomarenko, Peter Blake, Kostya S. Novoselov, Kenji Watanabe, Takashi Taniguchi, and A. K. Geim. Micrometer-scale ballistic transport in encapsulated graphene at room temperature. *Nano Letters*, 11(6):2396–2399, 2011.

[69] Young-Woo Son, Marvin L. Cohen, and Steven G. Louie. Energy gaps in graphene nanoribbons. *Phys. Rev. Lett.*, 97:216803, 2006.

[70] S. Y. Zhou, G.-H. Gweon, A. V. Fedorov, P. N. First, W. A. de Heer, D.-H. Lee, F. Guinea, A. H. Castro Neto, and A. Lanzara. Substrate-induced bandgap opening in epitaxial graphene. *Nat. Mater.*, 6:770–775, 2007.

[71] J. Hicks, A. Tejeda, A. Taleb-Ibrahimi, M. S. Nevius, F. Wang, K. Sheppered, J. Palmer, F. Bertran, P. Le Fevre, J. Kunc, W. A. de Heer, C. Berger, and E. H. Conrad. A wide-bandgap metal-semiconductor-metal nanostructure made entirely from graphene. *Nat. Phys.*, 9:49–54, 2013.

[72] Seon-Myeong Choi, Seung-Hoon Jhi, and Young-Woo Son. Effects of strain on electronic properties of graphene. *Phys. Rev. B*, 81:081407, Feb 2010.

[73] J. Lahiri, Y. Lin, P. Bozkurt, I. Oleynik, and M. Batzill. An extended defect in graphene as a metallic wire. *Nat. Nano.*, 5:326–329, 2010.

[74] Richard Balog, Bjarke Jorgensen, Louis Nilsson, Mie Andersen, Emile Rienks, Marco Bianchi, Mattia Fanetti, Erik Laegsgaard, Alessandro Baraldi, Silvano Lizzit, Zeljko Sljivancanin, Flemming Besenbacher, Bjork Hammer, Thomas G. Pedersen, Philip Hofmann, and Liv Hornekaer. Bandgap opening in graphene induced by patterned hydrogen adsorption. *Nature Mater.*, 9:315–319, 2010.

[75] J. Eroms and D. Weiss. Weak localization and transport gap in graphene antidot lattices. *New Journal of Physics*, 11(9):095021, 2009.

[76] Myungwoong Kim, Nathaniel S. Safron, Eungnak Han, Michael S. Arnold, and Padma Gopalan. Fabrication and characterization of large-area, semiconducting nanoperforated graphene materials. *Nano Letters*, 10(4):1125–1131, 2010.

[77] K. F. Allison, D. Borka, I. Radović, Lj. Hadžievski, and Z. L. Mišković. Dynamic polarization of graphene by moving external charges: Random phase approximation. *Phys. Rev. B*, 80:195405, Nov 2009.

[78] Cheol-Hwan Park, Li Yang, Young-Woo Son, Marvin L. Cohen, and Steven G. Louie. Anisotropic behaviours of massless dirac fermions in graphene under periodic potentials. *Nature Phys.*, 4:213–217, 2008.

[79] Jean-Christophe Charlier, Xavier Blase, and Stephan Roche. Electronic and transport properties of nanotubes. *Rev. Mod. Phys.*, 79:677–732, 2007.

[80] D. V. Kosynkin, A. L. Higginbotham, A. Sinitskii, J. R. Lomeda, A. Dimiev, B. K. Price, and J. M. Tour. Longitudinal unzipping of carbon nanotubes to form graphene nanoribbons. *Nature*, 458.

[81] O. O. Kit, T. Tallinen, L. Mahadevan, J. Timonen, and P. Koskinen. Twisting graphene nanoribbons into carbon nanotubes. *Phys. Rev. B*, 85:085428, Feb 2012.

[82] Li Yang, Cheol-Hwan Park, Young-Woo Son, Marvin L. Cohen, and Steven G. Louie. Quasiparticle energies and band gaps in graphene nanoribbons. *Phys. Rev. Lett.*, 99: 186801, 2007.

[83] L. Tapaszto, G. Dobrik, P Lambin, and L. P. Biro. Tailoring the atomic structure of graphene nanoribbons by scanning tunnelling microscope lithography. *Nat. Nano.*, 3: 397–401, 2008.

[84] J. M. Soler, Emilio Artacho, Julian D Gale, Alberto Garca, Javier Junquera, Pablo Ordejn, and Daniel Snchez-Portal. The siesta method for ab-initio order- n materials simulation. *Jour. Phys.: Cond. Matt.*, 14(11):2745, 2002.

[85] G. Kresse and J. Furthmüller. Efficient iterative schemes for *ab-initio* total-energy calculations using a plane-wave basis set. *Phys. Rev. B*, 54:11169–11186, Oct 1996.

[86] John P. Perdew, Kieron Burke, and Matthias Ernzerhof. Generalized gradient approximation made simple. *Phys. Rev. Lett.*, 77:3865–3868, Oct 1996.

[87] Tsuneya Ando and Takeshi Nakanishi. Impurity scattering in carbon nanotubes – absence of back scattering –. *Journal of the Physical Society of Japan*, 67(5):1704–1713, 1998.

[88] Tsuneya Ando, Takeshi Nakanishi, and Riichiro Saito. Berry's phase and absence of back scattering
in carbon nanotubes. *Journal of the Physical Society of Japan*, 67(8):2857–2862, 1998.

[89] A. K. Geim and K. S. Novoselov. The rise of graphene. *Nature Mater.*, 6:183–191, 2007.

[90] Ruiqi Zhao, Jinying Wang, Mingmei Yang, Zhongfan Liu, and Zhirong Liu. BN-embedded graphene with a ubiquitous gap opening. *J. Phys. Chem. C*, 116(39):21098–21103, 2012.

[91] Paolo Sessi, Jeffrey R. Guest, Matthias Bode, and Nathan P. Guisinger. Patterning graphene at the nanometer scale via hydrogen desorption. *Nano Lett.*, 9(12):4343–4347, 2009.

[92] Haili Gao, Lu Wang, Jijun Zhao, Feng Ding, and Jianping Lu. Band gap tuning of hydrogenated graphene: H coverage and configuration dependence. *J. Phys. Chem. C*, 115(8):3236–3242, 2011.

[93] Vitor M. Pereira, J. M. B. Lopes dos Santos, and A. H. Castro Neto. Modeling disorder in graphene. *Phys. Rev. B*, 77:115109, Mar 2008.

[94] Vitor M. Pereira, F. Guinea, J. M. B. Lopes dos Santos, N. M. R. Peres, and A. H. Castro Neto. Disorder induced localized states in graphene. *Phys. Rev. Lett.*, 96: 036801, Jan 2006.

[95] Rocco Martinazzo, Simone Casolo, and Gian Franco Tantardini. Symmetry-induced band-gap opening in graphene superlattices. *Phys. Rev. B*, 81:245420, Jun 2010.

[96] Mahboobeh Mirzadeh and Mani Farjam. First-principles study of bandgap effects in graphene due to hydrogen adsorption. *J. Phys.: Condens. Matter*, 24(23):235304, 2012.

[97] J. M. Garcia-Lastra. Strong dependence of band-gap opening at the dirac point of graphene upon hydrogen adsorption periodicity. *Phys. Rev. B*, 82:235418, Dec 2010.

[98] Joongoo Kang, Junhyeok Bang, Byungki Ryu, and K. J. Chang. Effect of atomic-scale defects on the low-energy electronic structure of graphene: Perturbation theory and local-density-functional calculations. *Phys. Rev. B*, 77:115453, Mar 2008.

[99] Roberto Grassi, Tony Low, and Mark Lundstrom. Scaling of the energy gap in pattern-hydrogenated graphene. *Nano Lett.*, 11(11):4574–4578, 2011.

[100] Behnaz Gharekhanlou, Marjan Alavi, and Sina Khorasani. Tight-binding description of patterned graphene. *Semicond. Sci. Tech.*, 23(7):075026, 2008.

[101] P. R. Wallace. The band theory of graphite. *Phys. Rev.*, 71:622, May 1947.

[102] Paul L. McEuen, Marc Bockrath, David H. Cobden, Young-Gui Yoon, and Steven G. Louie. Disorder, pseudospins, and backscattering in carbon nanotubes. *Phys. Rev. Lett.*, 83:5098–5101, Dec 1999.

[103] M. Dvorak, W. Oswald, and Z. Wu. Bandgap opening by patterning graphene. *Sci. Rep.*, 3:2289, 2013.

[104] A. Grüneis, C. Attaccalite, T. Pichler, V. Zabolotnyy, H. Shiozawa, S. L. Molodtsov, D. Inosov, A. Koitzsch, M. Knupfer, J. Schiessling, R. Follath, R. Weber, P. Rudolf, L. Wirtz, and A. Rubio. Electron-electron correlation in graphite: A combined angle-resolved photoemission and first-principles study. *Phys. Rev. Lett.*, 100:037601, Jan 2008.

[105] Young-Woo Son, Marvin L. Cohen, and Steven G. Louie. Energy gaps in graphene nanoribbons. *Phys. Rev. Lett.*, 97:216803, Nov 2006.

[106] Li Yang, Cheol-Hwan Park, Young-Woo Son, Marvin L. Cohen, and Steven G. Louie. Quasiparticle energies and band gaps in graphene nanoribbons. *Phys. Rev. Lett.*, 99: 186801, Nov 2007.

[107] K. S. Novoselov, V. I. Falko, L. Colombo, P. R. Gellert, M. G. Schwab, and K. Kim. A roadmap for graphene. *Nature*, 490:192–200, 2012.

[108] A. K. Geim and K. S. Novoselov. The rise of graphene. *Nature Mater.*, 6:183–191, 2007.

[109] M. Z. Hasan and C. L. Kane. Colloquium: Topological insulators. *Rev. Mod. Phys.*, 82:3045–3067, 2010.

[110] Vitor M. Pereira, A. H. Castro Neto, and N. M. R. Peres. Tight-binding approach to uniaxial strain in graphene. *Phys. Rev. B*, 80:045401, 2009.

[111] Guang-Xin Ni, Yi Zheng, Sukang Bae, Hye Ri Kim, Alexandre Pachoud, Young Soo Kim, Chang-Ling Tan, Danho Im, Jong-Hyun Ahn, Byung Hee Hong, and Barbaros zyilmaz. Quasi-periodic nanoripples in graphene grown by chemical vapor deposition and its impact on charge transport. *ACS Nano*, 6(2):1158–1164, 2012.

[112] M. Farjam and H. Rafii-Tabar. Uniaxial strain on gapped graphene. *Physica E*, 42(8): 2109 – 2114, 2010.

[113] Leticia Tarruell, Daniel Greif, Thomas Uehlinger, Gregor Jotzu, and Tilman Esslinger. Creating, moving and merging dirac points with a fermi gas in a tunable honeycomb lattice. *Nature*, 483:302–305, 2012.

[114] Julen Ibañez Azpiroz, Asier Eiguren, Aitor Bergara, Giulio Pettini, and Michele Modugno. Self-consistent tight-binding description of dirac points moving and merging in two-dimensional optical lattices. *Phys. Rev. A*, 88:033631, Sep 2013.

[115] Shi-Liang Zhu, Baigeng Wang, and L.-M. Duan. Simulation and detection of dirac fermions with cold atoms in an optical lattice. *Phys. Rev. Lett.*, 98:260402, Jun 2007.

[116] Li Wang and Libin Fu. Interaction-induced merging of dirac points in non-abelian optical lattices. *Phys. Rev. A*, 87:053612, May 2013.

[117] Marco Polini, Francisco Guinea, Maciej Lewenstein, Hari C. Manoharan, and Vittorio Pellegrini. Artificial honeycomb lattices for electrons, atoms and photons. *Nature Nanotech.*, 8:625, 2013.

[118] B. Wunsch, F. Guinea, and F. Sols. Dirac-point engineering and topological phase transitions in honeycomb optical lattices. *New J. Phys.*, 10(10):103027, 2008.

[119] G. Montambaux, F. Piéchon, J.-N. Fuchs, and M. O. Goerbig. Merging of dirac points in a two-dimensional crystal. *Phys. Rev. B*, 80:153412, 2009.

[120] Yasumasa Hasegawa and Keita Kishigi. Merging dirac points and topological phase transitions in the tight-binding model on the generalized honeycomb lattice. *Phys. Rev. B*, 86:165430, 2012.

[121] C. H. Park and S. G. Louie. Making massless dirac fermions from a patterned two-dimensional electron gas. *Nano Lett.*, 9:1793–1797, 2009.

[122] A. Singha, M. Gibertini, B. Karmakar, S. Yuan, M. Polini, G. Vignale, M. I . Katsnelson, A. Pinczuk, L. N. Pfeiffer, K. W. West, and V. Pellegrini. Two dimensional mott?hubbard electrons in an artificial honeycomb lattice. *Science*, 332:1176–1179, 2011.

[123] Myungwoong Kim, Nathaniel S. Safron, Eungnak Han, Michael S. Arnold, and Padma Gopalan. Fabrication and characterization of large-area, semiconducting nanoperforated graphene materials. *Nano Lett.*, 10(4):1125–1131, 2010.

[124] Marc Dvorak and Zhigang Wu. Geometrically induced transitions between semimetal and semiconductor in graphene. *Phys. Rev. B*, 90:115415, Sep 2014.

[125] L. Nordheim. *Ann. Physik*, 9:607, 1931.

[126] R. H. Parmenter. Energy levels of a disordered alloy. *Phys. Rev.*, 97:587–598, 1955.

[127] Tsuneya Ando and Takeshi Nakanishi. Impurity scattering in carbon nanotubes - absence of back scattering. *J. Phys. Soc. Jap.*, 67(5):1704–1713, 1998.

[128] Tsuneya Ando, Takeshi Nakanishi, and Riichiro Saito. Berry's phase and absence of back scattering in carbon nanotubes. *J. Phys. Soc. Jap.*, 67(8):2857–2862, 1998.

[129] Paul L. McEuen, Marc Bockrath, David H. Cobden, Young-Gui Yoon, and Steven G. Louie. Disorder, pseudospins, and backscattering in carbon nanotubes. *Phys. Rev. Lett.*, 83:5098–5101, Dec 1999.

[130] K. S. Novoselov, A. K. Geim, S. V. Morozov, D. Jiang, Y. Zhang, S. V. Dubonos, I. V. Grigorieva, and A. A. Firsov. Electric field effect in atomically thin carbon films. 306 (5696):666–669, 2004.

[131] K. S. Novoselov, A. K. Geim, S. V. Morozov, D. Jiang, M. I. Katsnelson, I. V. Grigorieva, S. V. Dubonos, and A. A. Firsov. Two-dimensional gas of massless dirac fermions in graphene. *Nature*, 438:197–200, 2005.

[132] A. Castro Neto, F. Guinea, N. Peres, K. Novoselov, and A. Geim. The electronic properties of graphene. *Rev. Mod. Phys.*, 81:109–162, Jan 2009.

[133] A. Nagashima, N. Tejima, Y. Gamou, T. Kawai, and C. Oshima. Electronic structure of monolayer hexagonal boron nitride physisorbed on metal surfaces. *Phys. Rev. Lett.*, 75:3918–3921, Nov 1995.

[134] Kin Mak, Changgu Lee, James Hone, Jie Shan, and Tony Heinz. Atomically thin MoS_2: A new direct-gap semiconductor. *Phys. Rev. Lett.*, 105:136805, Sep 2010.

[135] K. S. Novoselov, D. Jiang, F. Schedin, T. J. Booth, V. V. Khotkevich, S. V. Morozov, and A. K. Geim. Two-dimensional atomic crystals. *Proc. Nat. Acad. Sci.*, 102(30): 10451–10453, 2005.

[136] D. Hsieh, Y. Xia, D. Qian, L. Wray, J. H. Dil, F. Meier, J. Osterwalder, L. Patthey, J. G. Checkelsky, N. P. Ong, A. V. Fedorov, H. Lin, A. Bansil, D. Grauer, Y. S. Hor, R. J. Cava, and M. Z. Hasan. A tunable topological insulator in the spin helical dirac transport regime. *Nature*, 460:1101–1105, 2009.

[137] Lijie Ci, Li Song, Chuanhong Jin, Deep Jariwala, Dangxin Wu, Yongjie Li, Anchal Srivastava, Z. F. Wang, Kevin Storr, Luisa Balicas, Feng Liu, and Pulickel M. Ajayan. Atomic layers of hybridized boron nitride and graphene domains. *Nature Mater.*, 9: 430–435, 2010.

[138] B. Xu, Y. H. Lu, Y. P. Feng, and J. Y. Lin. Density functional theory study of bn-doped graphene superlattice: Role of geometrical shape and size. *J. Appl. Phys.*, 108 (7):073711, 2010.

[139] Mark S. Hybertsen and Steven G. Louie. Electron correlation in semiconductors and insulators: Band gaps and quasiparticle energies. *Phys. Rev. B*, 34:5390–5413, Oct 1986.

[140] Wilfried G. Aulbur, Lars Jnsson, and John W. Wilkins. Quasiparticle calculations in solids. volume 54 of *Solid State Physics*, pages 1 – 218. Academic Press, 1999.

[141] Michael Rohlfing and Steven G. Louie. Electron-hole excitations and optical spectra from first principles. *Phys. Rev. B*, 62:4927–4944, Aug 2000.

[142] Diana Y. Qiu, Felipe H. da Jornada, and Steven G. Louie. Optical spectrum of MoS_2: Many-body effects and diversity of exciton states. *Phys. Rev. Lett.*, 111:216805, Nov 2013.

[143] Keliang He, Nardeep Kumar, Liang Zhao, Zefang Wang, Kin Fai Mak, Hui Zhao, and Jie Shan. Tightly bound excitons in monolayer WSe_2. *Phys. Rev. Lett.*, 113:026803, Jul 2014.

[144] M. Dvorak and Z. Wu. Dirac point movemement and topological phase transition in defected graphene. *Nanoscale*, 7:3645, 2015.

[145] Paolo Giannozzi, Stefano Baroni, Nicola Bonini, Matteo Calandra, Roberto Car, Carlo Cavazzoni, Davide Ceresoli, Guido L Chiarotti, Matteo Cococcioni, Ismaila Dabo, Andrea Dal Corso, Stefano de Gironcoli, Stefano Fabris, Guido Fratesi, Ralph Gebauer, Uwe Gerstmann, Christos Gougoussis, Anton Kokalj, Michele Lazzeri, Layla Martin-Samos, Nicola Marzari, Francesco Mauri, Riccardo Mazzarello, Stefano Paolini, Alfredo Pasquarello, Lorenzo Paulatto, Carlo Sbraccia, Sandro Scandolo, Gabriele Sclauzero, Ari P Seitsonen, Alexander Smogunov, Paolo Umari, and Renata M Wentzcovitch. Quantum espresso: a modular and open-source software project for quantum simulations of materials. *Jour. of Phys.: Cond. Matt.*, 21(39):395502, 2009.

[146] Miguel M. Ugeda, Aaron J. Bradley, Su-Fei Shi, Felipe H. da Jornada, Yi Zhang, Diana Y. Qiu, Wei Ruan, Sung-Kwan Mo, Zahid Hussain, Zhi-Xun Shen, Feng Wang, Steven G. Louie, and Michael F. Crommie. Giant bandgap renormalization and excitonic effects in a monolayer transition metal dichalcogenide semiconductor. *Nature Mater.*, 4061, 2014.

[147] Marco Bernardi, Maurizia Palummo, and Jeffrey C. Grossman. Optoelectronic properties in monolayers of hybridized graphene and hexagonal boron nitride. *Phys. Rev. Lett.*, 108:226805, Jun 2012.

[148] Michael Rohlfing and Steven G. Louie. Electron-hole excitations in semiconductors and insulators. *Phys. Rev. Lett.*, 81:2312–2315, Sep 1998.

[149] Gautham Nair, Liang-Yi Chang, Scott M. Geyer, and Moungi G. Bawendi. Perspective on the prospects of a carrier multiplication nanocrystal solar cell. *Nano Lett.*, 11:2145–2151, 2011.

[150] Xiao-Liang Qi and Shou-Cheng Zhang. Topological insulators and superconductors. *Rev. Mod. Phys.*, 83:1057–1110, Oct 2011.

[151] B. Andrei Bernevig, Taylor L. Hughes, and Shou-Cheng Zhang. Quantum spin hall effect and topological phase transition in HgTe quantum wells. *Science*, 314(5806): 1757–1761, 2006.

[152] Y. L. Chen, J. G. Analytis, J.-H. Chu, Z. K. Liu, S.-K. Mo, X. L. Qi, H. J. Zhang, D. H. Lu, X. Dai, Z. Fang, S. C. Zhang, I. R. Fisher, Z. Hussain, and Z.-X. Shen. Experimental realization of a three-dimensional topological insulator, Bi2Te3. *Science*, 325(5937):178–181, 2009.

[153] Markus Knig, Steffen Wiedmann, Christoph Brne, Andreas Roth, Hartmut Buhmann, Laurens W. Molenkamp, Xiao-Liang Qi, and Shou-Cheng Zhang. Quantum spin hall insulator state in HgTe quantum wells. *Science*, 318(5851):766–770, 2007.

[154] B. A. Bernevig. *Topological insulators and topological superconductors.* Princeton University Press, 2013.

[155] F. D. M. Haldane. Model for a quantum hall effect without landau levels: Condensed-matter realization of the "parity anomaly". *Phys. Rev. Lett.*, 61:2015–2018, Oct 1988.

[156] C. Weeks, J. Hu, J. Alicea, M. Franz, and R. Wu. Engineering a robust quantum spin hall state in graphene via adatom deposition. *Phys. Rev. X*, 1:021001, Oct 2011.

[157] J. Hu, J. Alicea, R. Wu, and M. Franz. Giant topological insulator gap in graphene with $5d$ adatoms. *Phys. Rev. Lett.*, 109:266801, Dec 2012.

[158] A. A. Soluyanov and D. Vanderbilt. Wannier representation of Z_2 topological insulators. *Phys. Rev. B*, 83:035108, Jan 2011.

[159] A. A. Soluyanov and D. Vanderbilt. Computing topological invariants without inversion symmetry. *Phys. Rev. B*, 83:235401, Jun 2011.

[160] S. Reich, J. Maultzsch, C. Thomsen, and P. Ordejón. Tight-binding description of graphene. *Phys. Rev. B*, 66:035412, 2002.

[161] K. Nakada, M. Fujita, G. Dresselhaus, and M. S. Dresselhaus. Edge state in graphene ribbons: Nanometer size effect and edge shape dependence. *Phys. Rev. B*, 54:17954–17961, Dec 1996.

[162] M. Fujita, K. Wakabayashi, K. Nakada, and K. Kusakabe. Peculiar localized state at zigzag graphite edge. *Journ. of the Phys. Soc. of Japan*, 65(7):1920–1923, 1996.

[163] K. Wakabayashi, M. Fujita, H. Ajiki, and M. Sigrist. Electronic and magnetic properties of nanographite ribbons. *Phys. Rev. B*, 59:8271–8282, Mar 1999.

[164] M. Ezawa. Peculiar width dependence of the electronic properties of carbon nanoribbons. *Phys. Rev. B*, 73:045432, Jan 2006.

[165] G. Autes and O. V. Yazyev. Engineering quantum spin hall effect in graphene nanoribbons via edge functionalization. *Phys. Rev. B*, 87:241404, Jun 2013.

[166] L. Matthes and F. Bechstedt. Influence of edge and field effects on topological states of germanene nanoribbons from self-consistent calculations. *Phys. Rev. B*, 90:165431, Oct 2014.